



SAPIENZA
UNIVERSITÀ DI ROMA

DOTTORATO DI RICERCA IN ENERGIA E AMBIENTE
PhD Program in ENERGY and ENVIRONMENT

XXXV Cycle

**Radiometric impact assessments and
shielding of CubeSat class satellites in
interaction with orbital radiation fields and
representativity of the calibration procedure
and radiation damage tests in the ground
facility**

PhD Thesis

Scuola di Dottorato in Scienze e Tecnologie per l'Innovazione Industriale
Facoltà di Ingegneria Civile e Industriale
Dipartimento di Ingegneria Astronautica, Elettrica ed Energetica

Nunzio Burgio

Advisor
Prof. Massimo Corcione

Co-Advisor/Tutor
Prof. Massimo Frullini

A.A. 2022-2023

Abstract

Using FLUKA and MCNP nuclear particle transport codes, support for radiation shielding design and assessing damage to aerospace components and systems has been developed. In order to make the method quantitative, it was necessary to face the representativeness of the damage tests conducted on the aerospace components and systems with accelerators, nuclear research reactors, and spontaneous decay sources by making parallels with the orbital sources obtained from the applications used in the design of missions. As the first step, a high-energy calibration of the codes has been executed comparing the simulation results obtained simulating the Galactic Cosmic Ray atmospheric shower with the measured fluxes and spectra of secondary cosmic neutrons from ground stations, obtaining an excellent agreement. The activity continued with the design of the payload radiation shield of the ABCS (Astro Bio CubeSat) satellite launched in the Van Allen belt in the summer of 2022. A further point of verification was the comparison between dose rates measured with the dosimeters integrated into the ABCS payload during the mission and the simulated ones, which appear to be in fair agreement paving the way for the design of a series of ground-based experiments to be performed in parallel on research accelerators and reactors, to quantify and unify equivalent damage measurements.

The present document is distributed under the license Creative Commons CC BY-NC-SA

“Il presente documento è distribuito secondo la licenza Creative Commons CC BY-NC-SA, attribuzione, non usi commerciali, condividi allo stesso modo.”

Contents

Introduction	4
Chapter 1 – The natural radiation sources of interest in aerospace activities.....	6
The Solar radiation environment.....	7
The Galactic Cosmic Ray (GCR)	10
The trapped particles in Van Allen’s Belt	14
Conclusion	15
Chapter 2 - The transport code for nuclear particles and ions.....	17
Introduction.....	17
Generalities on MC techniques for the transport of nuclear particles.....	18
The definition of a simulation in an MC code for nuclear particle transport.....	21
Source Definition	21
Geometry definition.....	23
Materials definition.....	24
Estimators.....	25
Biasing techniques	28
FLUKA parallel execution.....	29
Conclusions.....	30
Chapter 3 – The atmospheric neutrons: comparisons between FLUKA models and measurements from the ground station	31
Introduction.....	31
Generalities on the FLUKA model to estimate local GCR ion shower at various altitudes in the Earth’s atmosphere and surface	31
Model geometry	32
Materials	35
GCR Source	36
Transport options	38
Simulations set	39
FLUKA’s estimates of some selected particles in the GCR atmospheric shower.....	41
Single Events Upset estimation	48
Neutron Flux Comparison between FLUKA and BSY model.....	49
Conclusions.....	52
Chapter 4 The ground irradiation facilities	53
Introduction.....	53
The Si slab model definition	54

Generalities on solid irradiation	54
Displacement Per Atom.....	54
Frenkel pair.....	55
Lindhard Partition Function $\xi(T)$	56
Nuclear Stopping Force	57
Equivalent Damage	57
FLUKA simulations tests	58
Simulation results	59
The FLUKA simulation of the radFET calibration	60
Generalities on radFETs and the VT-02 Varadis radFET	60
Implementation of the VT-02 radFET geometry in FLUKA	62
Radiation source selected for the simulation.....	62
FLUKA simulations set	63
Simulation results	64
Conclusions.....	67
Chapter 5 – Radiometric Analysis of the ABCS payload.....	69
Introduction.....	69
Calculation Assumption and Model definitions.....	70
Implementation of the ABCS layout’s relevant features in the FLUKA and MCNP models	70
Orbital source term definitions	73
The source term for simulation with MCNP in the TAPIRO reactor	78
Description of the MCNP and FLUKA Simulation Sets	79
Estimation of the TID and SI1MEVNE in selected satellite components.....	80
Results and discussion	82
TID rate estimation in ABCS Payload.....	82
TID rate and shielding effectiveness estimations in the Solar Panels.....	86
The Silicon 1 MeV neutron equivalent fluxes in the ABCS target components.....	87
Comparisons of the FLUKA estimates of the dose rate with the ABCS onboard radFET reading.....	89
Conclusion and Future work.....	93
References.....	95

Introduction

The present thesis aims are primarily on the use the nuclear transport codes in aerospace activities to define the design parameter of electronic components to be integrated into aerospace systems, their fault tolerance on radiation, designing tests on the ground facilities to both test components, systems and, in some cases, entire dummy satellites.

The leading idea is not to implement yet another web-based radioactivity calculator calibrated on some specific design requirement but to integrate general-purpose nuclear transport codes into the concurrent development cycle of satellites and spacecraft.

Such a tool requires the training and operativity of a qualified nuclear engineer to be included in the development team and the mission pre- and post-analysis. Consequently, his skill must be extended to interpreting the results from the qualification tests of radiation hardening components and designing ad hoc tests for special components.

The thesis starts describing in chapter one the so-called “space weather” that characterised the dynamically changing environment encountered by aircraft and spacecraft during routine activities.

Central to space weather is the continuous observation of the sun’s activity that causes a chain of events such as SF (Solar Flares), CME (Coronal Mass Ejection), SEP (Solar Energetic Particle), and HSS (High-speed Solar wind Stream) that create changes in ambient plasma, magnetic fields, and particles flow in space and interaction with the magnetosphere disturbing the availability of telecommunications and many other systems.

Also, the GCR (Galactic Cosmic Ray) contribute to the space environment, and its anti-correlation with solar activity is also introduced. Examples of in-orbit radiative environments up to the Van Allen’s Belt as defined through the models used in the SPENVIS (Space Environment Information System) code systems and database.

A description of the stand-alone codes that simulate the interaction between the radiative sources and target components and the distinction between stochastic and deterministic transport codes is given in chapter 2, where The choice to adopt the stochastic codes for the present study is motivated, and the main features of MCNP and FLUKA Monte Carlo codes, are then presented.

Chapter 3 deals with the FLUKA simulation of the GCR shower into the atmosphere to estimate the secondary neutrons flux and energy distribution in various locations on the Earth’s surface. The results were compared, finding a good agreement, with other numerical models and publicly available measurements from ground stations worldwide. The discussion of the results is an occasion to revise the central concept related to cosmic rays and the tools necessary to define their local composition at the beginning of the injection into the Earth’s atmosphere to model their shower.

Chapter 4 presents the central concept of radiation damage on solids. Then, the effect on a reference silicon slab of beams and fields of particles, representative of readily available facilities (accelerators, research nuclear reactors, ^{60}Co sources) and more rare ones as heavy ion accelerators,

is revised using a simple set of FLUKA simulation. The results underline the difference and similitude of the imparted damages using different irradiation sources. Finally, the concept of equivalent damage is introduced.

Entering the more operative thesis phase, chapter 5 describes the shielding design for the payload of the ABCS (Astro Bio CubeSat) mission and compares the estimated dose rate with the measurement performed during the mission. The discussion of the design and the comparison of the mission outcomes constitutes an example of applying all the concepts and techniques presented in the previous chapters. Finally, the conclusions of this work and some hints for the development of future work were presented.

Chapter 1 – The natural radiation sources of interest in aerospace activities.

The design of aerospace systems with high availability levels towards the spatial radiative environments requests an accurate knowledge of each relevant radiation source that contributes to the interaction with the system. The tools that allow such knowledge are embedded in space weather modelling. Space weather can be defined according to the following definition [1]

“Space Weather is the physical and phenomenological state of natural space environments. The associated discipline aims, through observation, monitoring, analysis and modelling, to understand and predict the state of the sun, the interplanetary and planetary environments, and the solar and non-solar driven perturbations that affect them, and also at forecasting and nowcasting the potential impacts on biological and technological systems.”

In 1913, Victor Hess [2], the father of cosmic ray physics, proved, by balloon experiments with electroscopes, that background radiation increases with altitude, contrary to common belief. He called this phenomenon “Cosmic Rays”; consequently, he won the Nobel Prize in 1936. Cosmic rays have played a fundamental role in nuclear physics: in the past, they allowed the analysis of particles at energies not reachable with the available experimental equipment. In Hess’s sense, “cosmic rays” embrace all the detectable radioactive components arriving on Earth.

To remain within the scope of the present thesis, fulfilling the need to distinguish between different radiation sources at several orbital altitudes and also inside the Earth’s atmosphere and surface, we define three radiation terms: The galactic cosmic ray (GCR), the solar energetic particles (SEP), The Van Allen’s Belt trapped particles. The following paragraphs will briefly review such radiative sources to clarify their mutual interactions using some data obtained from the dedicated implementation of parametric models and the use of the built-in codes embedded in SPENVIS [3].

The same tools will be used in later chapters of this work as input data for transport calculation for the payload shielding design, support and irradiation test on the ground facility, and pre and post-mission analysis.

The Solar radiation environment

The sun and its activity are central to the formation of space weather. Thus, to better understand and define the radiative sources to be used in modelling and design activities is necessary to resume the main characteristics of the Sun emissions briefly.

Based on observing the sun's surface for centuries (see Figure 1.1), scientists found a nearly periodic 11-year change in its activity in terms of variation in the number of detected sunspots, known as the solar cycle (or solar magnetic activity cycle, sunspot cycle, Schwabe cycle). Throughout a solar cycle, the number and the magnitude of sunspots have a synchronous fluctuation from a minimum to a maximum of activity. When a solar cycle is near a maximum, the sun's magnetic field flips, and after two solar cycles, it returns to its original state (Hale cycle).

Figure 1.1 also includes the so-called Maunder minimum, a period between 1645 and 1715 where very few sunspots were registered. Therefore, some researchers argue that the period coincided with a climate change where the weather was colder than usual. Consequently, the idea of Solar driven climate change, besides the anthropic-driven one, is undoubtedly a polarising factor in the public debate on the Earth's climate status. However, without exit from the scope of the present description of the Solar environment, we observe that space science and spatial technologies should disclose knowledge of paramount importance for long-term decision-making [4].

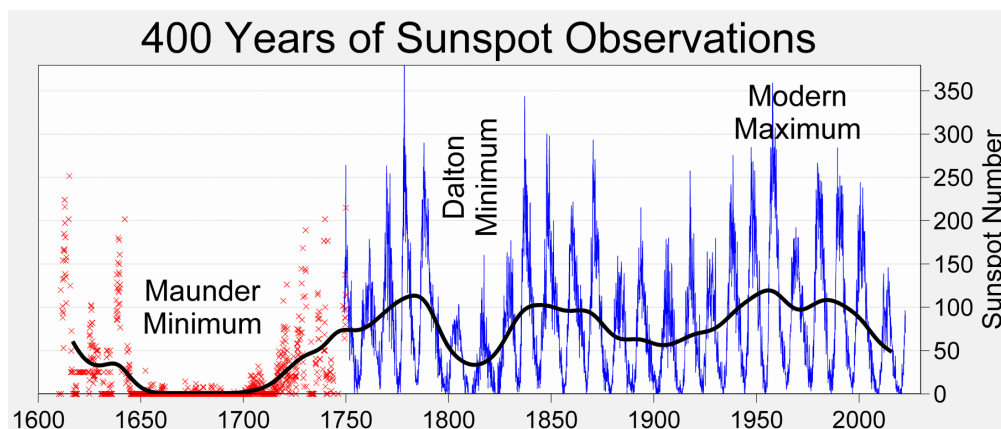


Figure 1.1: 400 years of sunspot history, including the period from 1645 to 1715, characterised by very few sunspots known as the Maunder minimum. [This file is licensed under the Creative Commons Attribution-Share Alike 3.0, https://en.wikipedia.org/wiki/File:Sunspot_Numbers.png 09/16/2022.]

Sunspots appear as temporary spots on the sun's photosphere denoted by a darker colour than the surrounding area due to a reduced surface temperature induced by magnetic flux increases that limit the convection (See Figure 1.2). Sunspots appeared to be confined, usually in pairs of opposite magnetic polarity, within zones called active regions characterised by a complex magnetic field. The sunspots, or group of it, decays in days to months, expanding and contracting in size with diameters ranging from 16 to 150000 km. Their relative motion speed is of the order of some hundred meters per second.

Sunspots indicate intense regional magnetic activity and are often precursors to phenomena like solar flares and coronal mass ejection. The solar flares are caused by the magnetic energy accumulated in the sun's atmosphere accelerating the plasma-charged particles and causing the emission of electromagnetic radiation (Mostly X – rays) that start travelling in space. The fraction of such radiation that reaches the Earth's atmosphere is absorbed in its upper layers (ionosphere), causing ionisation that interferes with short-wave communication. We cannot predict solar flares, and their observation is one of the early alert signals for the space weather forecast.



Figure 1.2: Usual shape of sunspots from the book “Atlante Astronomico (1890) di Giovanni Celoria”. [Macchia Solare. (2022, August 1). In Wikipedia. https://it.wikipedia.org/wiki/Macchia_solare]

Often associated with solar flares, a considerable release of plasma from the sun's corona, called Coronal Mass Ejection (CME), is ejected into the heliosphere. The ejected matter is a proton and electron plasma with an average speed of 490 km/s. When a CME leave the Sun and travels in interplanetary space becomes an Interplanetary Coronal Mass Ejection (ICME), triggering an alert for the space weather agency. ICME take one to five days to reach the Earth.

During travel, ICMEs interact with the Solar Wind (SW) and the heliospheric magnetic field. The interaction accelerated the ICMEs slower than SW and accelerated the faster ones. Often, only a tiny fraction of a CMS reaches the Earth. However, when an ICMS is directed toward the Earth, it causes a geomagnetic storm, disturbing radio transmission and damaging satellite and electrical transmission lines. The most notably geomagnetic storm was the solar storm of 1859 that damaged parts of the recently created United States telegraph network [5]. When an ICMS has a speed greater than 500 km/s, it drives a shock wave that should be closely linked with the Solar Energetic Particle (SEP) acceleration. SEP, reaching the Earth, causes intense aurorae in vast regions around the poles and exposes humans in aeroplanes or space stations to a risky level of radiation [6].

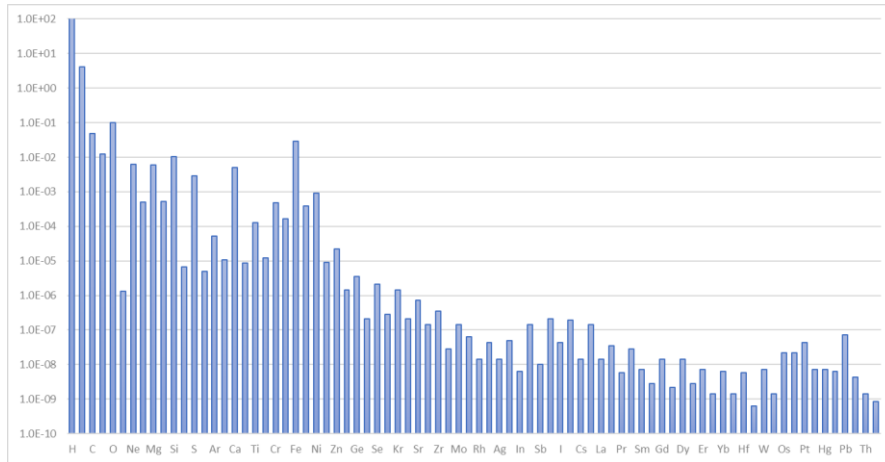


Figure 1.3: Relative abundance (logarithm scale) of ion in a SEP emission foreseen by the CRÈME96 code on a circular orbit at 900 km of altitude to Earth's surface.

Finally, we have calculated a SEP emission using the CRÈME96 module of the SPENVIS code, considering a circular orbit at 900 km of altitude from the Earth's surface. Figure 1.3 reports the CRÈME data, post-processed with a set of scripts, as the per cent of abundance rescaled to the total emission. Due to the predominance of hydrogen ions, the logarithm scale has been used to represent the ion's abundance histogram. Therefore, it is worth mentioning that, in traces, ions from almost all periodic system ions are present in the SEP emission.

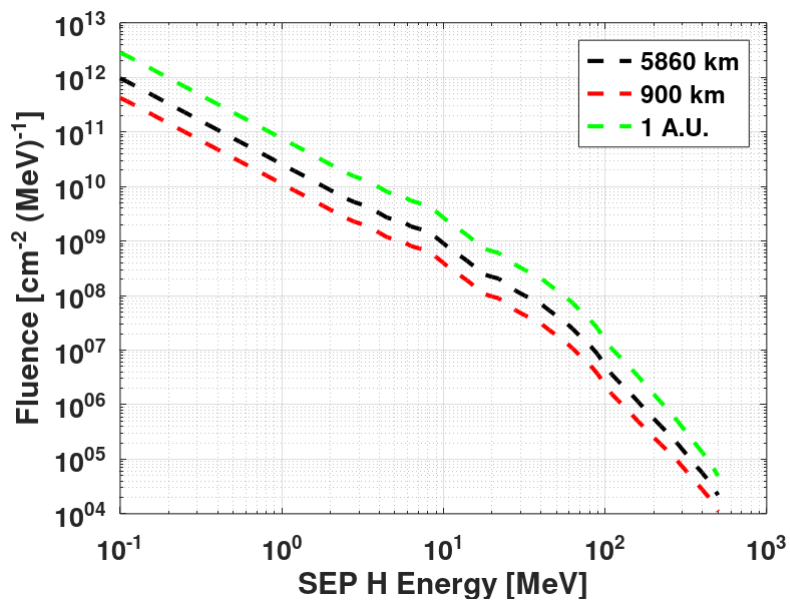


Figure 1.4: Comparison of the worst SEP fluences spectra in the year 2022 (Solar maximum cycle 25) at 900 km (LEO upper limit, red curve) and 5860 km (Van Allen Belt's, black curve) orbital distances from Earth and the same fluence at 1 AU (Astronomic Unit);

The Galactic Cosmic Ray (GCR)

GCR are a mixture of ions, photons and neutrinos covering kinetic energy that spans from hundreds of eV up to $1E20$ eV (1 EeV, see [7]). The charged component is mainly composed of protons (hydrogen, 83%), helium (3%), and heavy ions like carbon, iron, nickel, and other nuclei (1%). The remaining 13% are neutral components like photons and neutrinos.

The charged component includes all stable nuclei produced due to stellar nucleosynthesis, stellar flares, supernova explosions, quasar, blazars, pulsars, black holes and active galactic nuclei [8]. After production, they can be accelerated and completely ionised by the Fermi acceleration mechanism [9], interacting with magnetic fields in supernova remnants. They remained confined for hundreds of years, continuously increasing their energy, reaching speeds close to those of light, and, finally, they escaped magnetic fields and started to travel in space.

GCR undergoes many interactions in their passage through the interstellar medium, emitting secondaries in their reaction with dust and gases. The particles reaching the top of our atmosphere can be generated in any phase of those processes and, according to the different production mechanisms, show peculiar energy spectral trends.

Experimentally, the ion species were identified using the signatures of the masses of the secondary particles in the air-shower data (see Chapter 3). The energy spectra of the ions showed significant differences according to their origins. For example, uncollided ions accelerated by the Fermi mechanism have slightly flatter spectra than those created in the spallation reaction with nuclei of atoms and molecules of the interstellar gas. At lower energies, the spectra have a maximum in the energy range of 10^2 - 10^3 MeV/nucleon.

The cumulative CGR energy distribution in the solar system obeys a power law of the type

$$\frac{dN}{dE} \propto E^{-k} \quad \text{Equation 1.1}$$

Where E is the energy and k the spectral index.

Table 1.1: -Energy ranges and Mean flux of the GCR ions

Region of the GCR energy spectrum	Mean Ion Flux in region
$E < 10^{15}$ eV ("knee" $k=2.7$)	1 particle $\text{cm}^{-2}\text{s}^{-1}$
10^{15} eV $< E < 10^{18}$ eV ("ankle" $k=3.0$)	1 particle m^{-2} year $^{-1}$
$10^{18} < E < 10^{20}$ eV	From 1 particle km^{-2} year $^{-1}$ to 1 particle km^{-2} century $^{-1}$

According to Table 1.1, the spectrum can be divided into three energy regions. In the first region, the "knee", ions are considered of galactic origin, and the Fermi mechanism explains the kinetic energy they reach. Research is in progress to fully explain the slope changes between the "ankle" and the third region on the base of all possible galactic and extragalactic acceleration mechanisms. Table 1.1 resumes the order of magnitude of the GCR fluxes in the various spectral regions.

Due to several micro-Gauss's pervasive galactic magnetic field, the cosmic rays show a spiral trajectory with a diameter comparable to a fraction of the Galaxy diameter. The ions maintain those trajectories for hundreds of years, and when they finally reach the Earth, the information concerning the position of the sources is lost to a local observer.

Consequently, the spatial distribution of CGR is highly isotropic up to the energy of 10^{15} eV; however, some degree of anisotropy is localised in the energy region above the "ankle" [10]. Therefore, in the scope of this thesis, the isotropically-propagate GCR ions with energy up to 10^{15} eV are of practical interest.

When the GCR ions enter the solar system, they electro-magnetically interact with the plasma emitted by the sun during the solar activity and with its magnetic field. This kind of interaction modulated in time the GCR intensity: when the solar activity is high, the GCR flux intensity is reduced. Conversely, the GCR flux has a higher intensity during the Sun's quiet activity periods. The anti-correlation of the solar activity with the GCR flux intensity is described in various semi-empirical models. For example, we expressed, using a semi-empirical GCR model [11], the modulation of the energy differential spectra of each GCR ion for a given solar activity period, according to the following equations

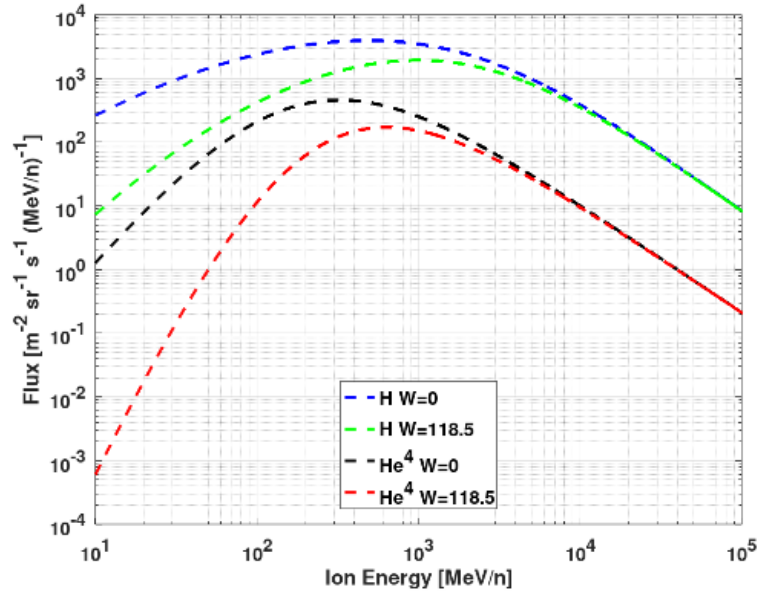
$$J_{GCR}(R, \varphi) = \frac{C_i \beta^{\alpha_i}}{R^{\gamma_i}} \frac{A_i}{Z_i} \frac{1}{\beta} \left(\frac{R}{R+R_0} \right)^{0.02W+4.7} \quad \text{Equation 1.2}$$

$$R_0 = 3 * 10^{-4} W + 0.37 \quad \text{Equation 1.3}$$

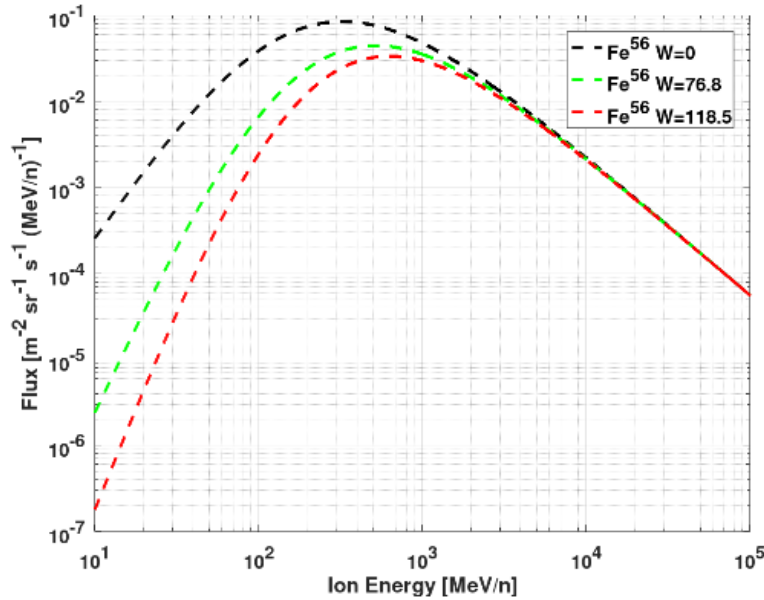
$$R = \frac{A_i}{Z_i} \sqrt{T^2 + 2TT_0} \quad \text{Equation 1.4}$$

Here subscript i is the GCR ion, R is the particle rigidity (GV), β is the ratio of particle speed and light speed, Z is the atomic number, A is the mass number, T is the kinetic energy of the ions, T_0 is its rest mass. W is the mean sunspot number for considering the influence of solar modulation, and C ($\text{cm}^{-2} \text{s}^{-1} \text{sr}^{-1} \text{GeV}^{-1}$) is a dimensional coefficient. α and γ are model-fitting parameters [12]. It is worth noting that such models are based on fitting experimental data, and more details on the topics can be found in [13].

Implementing such a model in an Octave [14] program, we calculated the spectra for Hydrogen and Helium at the solar minimum (sunspot number $W = 0$) and maximum (sunspot number $W = 118.5$). The results are reported in Figure 1.1b. The same Calculation has been made for ^{56}Fe , in this case (see Figure 1.1b), adding the spectra at the intermediate solar activity (sunspot number $W = 76.8$). Examining the spectra, the anti-correlation of the flux intensities with the increase of solar activity is apparent. The intensity decreasing during the maximum solar activity is particularly marked in the lower energies range. At higher energy, the influence of the solar activity modulation decreases and reaching 10^4 eV, the curves representing the spectra of each ion become coincident according to the increasing magnetic rigidity (Equation 1.4).



a)



b)

Figure 1.5: Comparison of the energy spectra of three GCR ions under the modulation of different solar activities: a) H and He at sunspot numbers $W=0$ and $W=118.5$; b) ^{56}Fe at sunspot number $W=0$, $W=76.8$, and $W=118.5$. It is apparent that above 10^4 MeV/n, the high magnetic rigidity (Equations 1.3 and 1.4) makes the modulation negligible.

The previous GCR model refers to the GCR spectra obtained within the solar system far from the Earth and without the geomagnetic field influence. It is possible using more refined models like the one included in SPENVIS to calculate the GCR source term considering the modulation contribution of the geomagnetic field. Figure 1.6 compared the GCR-H fluxes at $1.5e9$ km previously obtained with the GCR model implementation from the Matthia model and reported in Figure 1.5a (green curve) and 900 km from the Earth's surface using the ISO 15390 model [15].

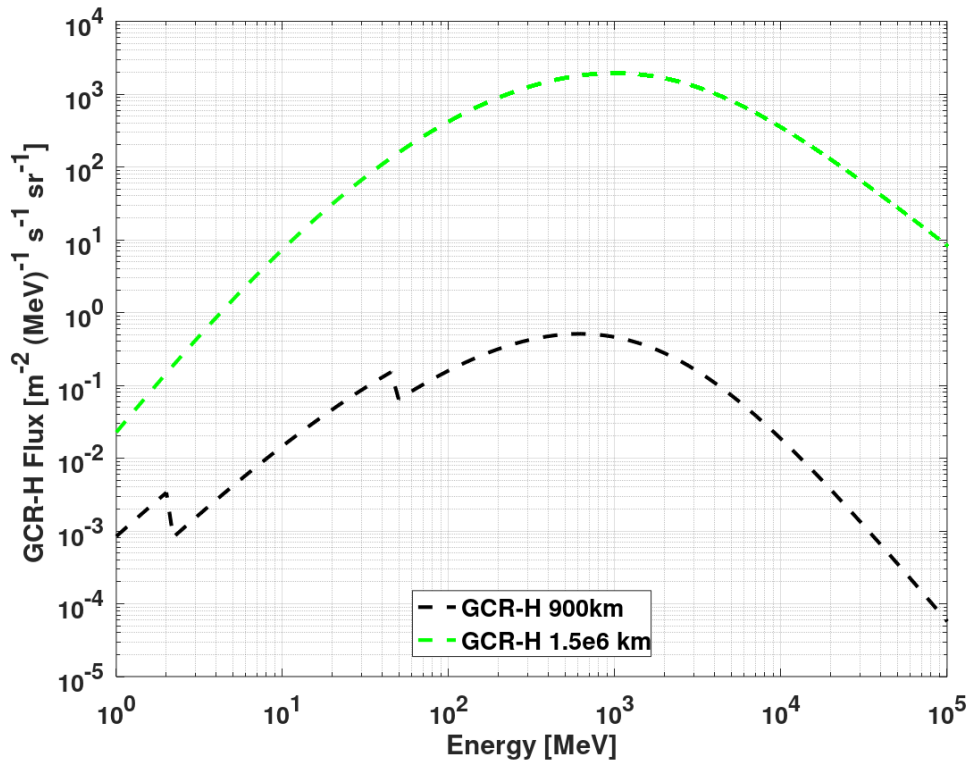


Figure 1.6: Comparison of the energy spectra of GCR hydrogen spectra at solar maximum at 900 km (black curve-ISO15390 model) and in space at 1.5e6 km (green curve- GCR model from [1.10]) from Earth's surface. The 900 km spectrum clearly shows the geomagnetic field's additive effect (new figure with Matthia model response covering the entire energy range).

Both spectra are computed at solar maximum: the spectrum at 900 km of altitude shows low-energy discontinuities between 2-3 MeV and 40-50 MeV that are not present in the smooth behaviour of the spectrum evaluation at 1.5e6 km from Earth's surface. Those differences are probably due to the geomagnetic field effect that in the 900 km orbit decelerates the GCR ions increasing the population of the low energy zones. However, it is worth mentioning that above 50 MeV, despite the decrease in intensity of 3 orders of magnitude for the 900 km spectra, the two spectra have the same curvature due to the higher ion's magnetic rigidity.

The trapped particles in Van Allen's Belt

A Van Allen radiation Belt is a confinement zone for charged particles trapped by the Earth's magnetosphere. The Belt's name originates from James Van Allen, the scientist credited for their discovery [16]. "Van Allen Belt" term is strictly used to indicate the region surrounding the Earth, but confinement regions with similar properties have also been discovered on other planets.

According to Figure 1.6, the Earth has two permanent belts in its magnetic field's inner region. Their extension is from 640 to 58000 km from our planet's surface. Besides the permanent belts, there is experimental evidence of the formation of more temporary ones.

The Van Allen's Belt radiative environment originates far from Earth in the mutual interaction of the SW ions, emitted during the Sun's periodic activity, GCR ions, and the occasional emission of SEP during SF. Near the Earth, the shielding influence of the geomagnetic field allows the deflection of the less energetic fraction of both GCR and SEP that slow down along the geomagnetic field's lines, remaining trapped for a long time in complex trajectories. Only a fraction of the ions had sufficiently high kinetic energy to penetrate beyond the Belt, interacting with the atmosphere and generating the well-known atmospheric particles' shower, whose secondary partially reached the ground [17].

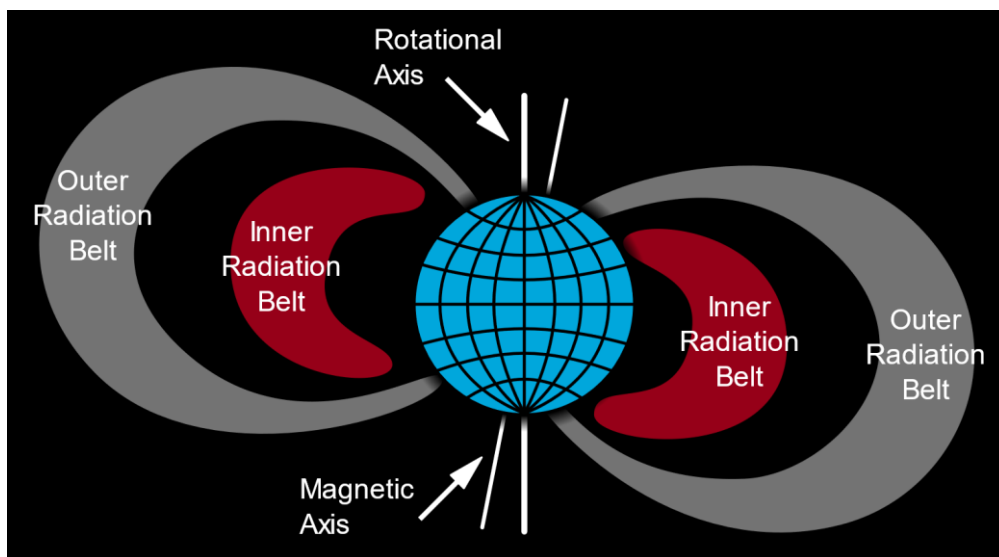


Figure 1.7: Schematic representation of the two main Van Allen belts where energetic particles were confined after their capture from the Earth's magnetosphere. [By Booyabazooka at English Wikipedia - Transferred from en.wikipedia to Commons., Public Domain, <https://commons.wikimedia.org/w/index.php?curid=1715297>]

The trapped particles' radiation term mainly consists of proton and electron, whose energy spectra are sufficiently intense to need a radiative shield to protect components and systems of satellites and spacecraft that pass through this region for long periods.

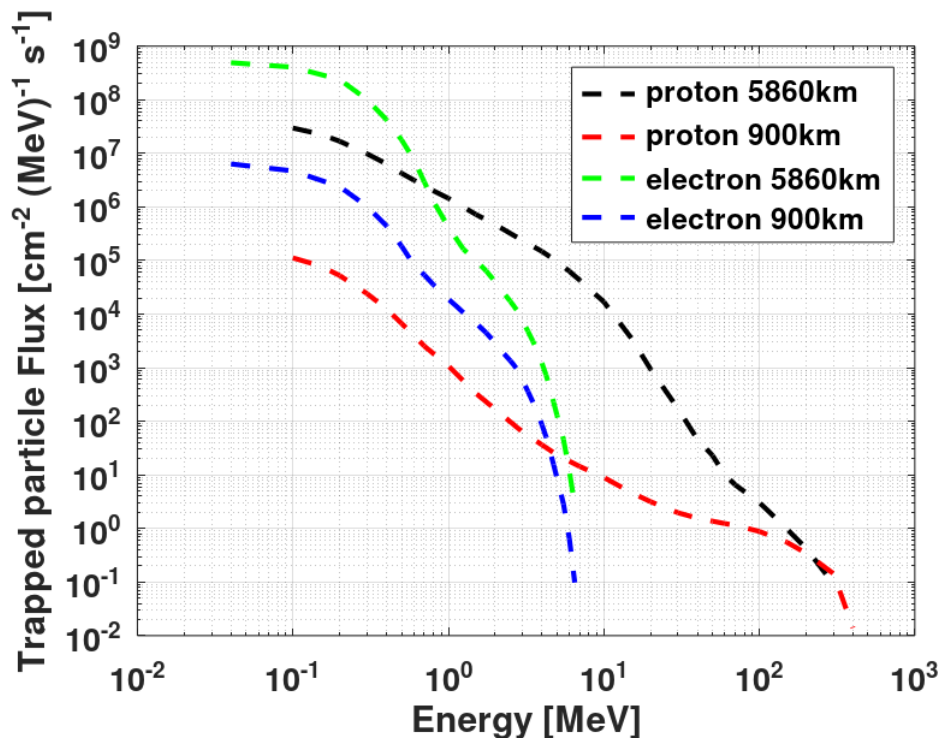


Figure 1.8: Comparison of the Trapped Particles Spectra obtained using AE8 and AP8 models embedded in SPENVIS for a solar maximum at a circular orbit of 900 km and 5860 km of altitude.

Figure 1.8 reports the energy distributions (energy spectrum) of trapped particles at 5860 km of altitude in the middle of the first Van Allen's Belt and at 900 km, which is approximately its lower limit (in particular conditions, the first Belt descendent up to 600 km of altitude). Trapped proton's energy spans from 0.1 MeV to 400 MeV, whereas electrons are more limited between 0.03 and 7 MeV. At both altitudes, trapped electron shows a greater intensity than protons. However, their narrow energy range makes them less penetrating, and the produced damages are concentrated in systems located on the external surface of the vehicle. Protons, due to the greater emission energy interval, penetrate more in deep, and they can deliver damage to the vehicle interior.

Conclusion

The classification of the total spatial source components has been obtained by discussing the Sun's cyclic activity's role and its occasional emission of SEP during SF events. Those solar sources (along with the heliomagnetic field) interact in space with the almost isotropic GCR ions coming from outside the solar system, modulating their intensity in an anticorrelated fashion concerning the solar maximum and minimum activity of each solar cycle.

Finally, SEP and GCR ions interact further with the geomagnetic field in their approach to the Earth. According to the local magnetic media threshold in magnetic rigidity, the energetic ion passes through the Van Allen Belts reaching the higher layers of the atmosphere, beginning the so-called GCR shower of secondary particles. The other ions, primarily protons, remain trapped within the Belts along with electrons and keep spiralling within the Belts. Such plasma, trapped in the Belts structure, constituted an additive radiation source for satellites and spacecraft having a fraction of their orbit intersecting that region.

Table 1.1 lists all the above-cited radiative components whose intensities and energetic spectra have been inferred by SPENVIS for a specific mission whose orbit is within the first Van Allen Belt.

Table 1.1: Total flux intensities of the orbital source components at 5860 km of altitude

Source Term	Flux [cm-2 s-1]	Fraction of the total flux	Model used
Trapped Proton	5.02E6	35.67%	AE8 min
Trapped Electron	9.05E6	64.32%	AP8 min
GCR	9.78	0.0001%	ISO-15390 Standard Model
SEP	457	0.00033%	ESP-PHYSICS (worst event fluence)

Those data are used as input for transport codes that estimate the secondary particle field generated in the interaction of the primary particles with the satellite structure. The results can be used in subsequent calculations concerning all the nuclear aspects of such a mission: payload shielding, onboard radiation detector design, dosimetry on payload, and radiation damage to electronic components and systems.

Due to the high heterogeneity in the geometric layout and material composition of the vehicles, it is convenient, despite the often high computational time penalty, to adopt Monte Carlo (MC) codes for transporting nuclear particles and ions. To fulfil this aim, we adopted the FLUKA MC codes, and the motivation for its use among other MC codes is the argument of Chapter 2.

Chapter 2 - The transport code for nuclear particles and ions

Introduction

In Chapter 1, we deal with the kind of particles and nuclei constituents of the sources that can be encountered during a spatial mission, stressing the Sun's central role in their emission and in the modulation of the GCR that approaches the solar system. The roles of the geomagnetic field in creating additional local radiation sources, such as the Van Allen Belts, have also been discussed. The tools that allow the definition of spatial sources representative of a given mission have been introduced.

As in many fields of applied science and engineering, extensive computer simulations that can be executed at the design stage and in pre and post-mission analysis help to cut costs and time, the codes used to simulate the interaction of the primary radiation sources with the vehicle's material designed for a mission are grouped under the definition of nuclear transport codes.

We can distinguish two broad categories of transport codes according to their simulation engines: Monte Carlo (MC) and Deterministic Codes (DC).

MC codes estimate user-selected quantities (such as particle fluxes, nuclear reaction rate, and doses), inferring their mean values and variance from the statistical exploration of a selected portion of the phase space problem using a sample of the source particles' target population. MC codes have a high degree of accuracy in describing the system's geometrical layout and material composition, allowing the evaluation of the heterogeneity effects. MC code's major drawback is the sometimes long computational time requested to reach an acceptable precision in the estimated values. This inconvenience is partially mitigated using variance reduction techniques [18] and massive computational resources [19].

DC codes solve the Boltzmann transfer equation tailored to the user-defined problem. The Boltzmann equation can assume different formulations according to the primary and secondary particle nature, geometry, and materials [20]. However, the DC codes are prevalently numerical solvers because of the difficulty in finding an analytical solution for the Boltzmann equation, except in the case of elementary problems [21]. Moreover, DC codes are much faster than MC ones but cannot represent complex geometries and strong material heterogeneities in density and composition.

Often in the design strategies, both types of codes are used. Typically, DC code defines the general layout during the conceptual design and the so-called "importance function" used by an MC code on a more refined layout to apply a variance reduction scheme to shorten the calculation time.

Sometimes the logic of the design strategy is reversed, the MC codes are used to simplify the design layout, controlling that the estimated parameters of interest do not change above a given tolerance, and the resulting equivalent layout is used to simulate the system with DCs.

Historically the reference DC used for space application is the HZETRN code[60], that apart from the restricted availability, does not match entirely with the requirement for this work. Therefore, MC codes, in our case, are best suited for our modelling activity. In particular, as illustrated in the following, we used general-purpose MC as FLUKA [22-25] and MCNP [26].

Generalities on MC techniques for the transport of nuclear particles

As already stated in the introduction of this chapter, the DC solves the transport equation for the averaged particle behaviour giving complete information through the phase space problem. MC obtains answers inferring the physical system's properties from the simulated particles' behaviour, limiting the information to specific (user-selected) regions of the phase space. A simple example helps to clarify those statements: we use both methods to calculate the volume of a sphere.

Using the analytical method, we derive the well-known formula to calculate the sphere volume according to

$$\begin{aligned}
 V &= \pi \int_{-r}^r (\sqrt{r^2 - x^2})^2 dx = 2\pi \int_0^r (r^2 - x^2) dx = \\
 &= 2\pi \left[r^2x - \frac{x^3}{3} \right]_0^r = \frac{4}{3} \pi r^3 \quad \text{Equation 2.1}
 \end{aligned}$$

Once resolved the integral, the analytical solution allows the Calculation of the sphere volume if the radius is known. The error in the volume calculation depends only on the uncertainties in the radius measurements.

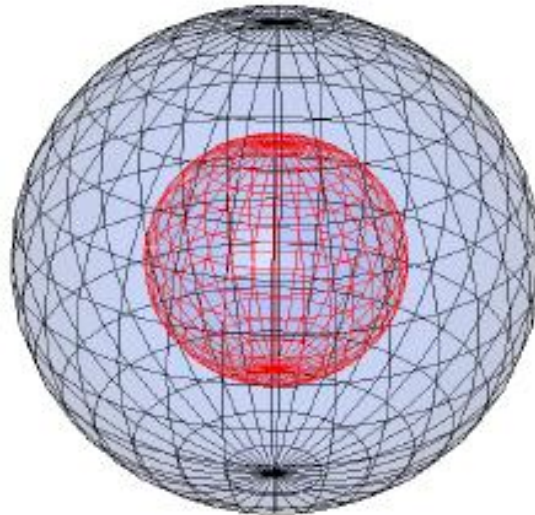


Figure 2.1: Geometric set-up for estimating the volume of a sphere of unspecified radius (red sphere) contained inside a second larger sphere of know radius R (black sphere). The surface of the black sphere emits from the surface a sample of N inward-directed pseudo-particles whose trajectories could cross the volume of the black sphere realising in its interior track of a given length. According to equation 2.2, the track length density estimates the sphere volume. The method is valid independently of the complexity of the region's shape.

The method is entirely different if the sphere volume is calculated using an MC approach. The algorithm is :

- According to Figure 2.1, Another sphere of known radius R that completely contains the sphere whose volume had to be calculated (noteworthy, its radius r is not necessarily known).
- Sample N emission points randomly on the outer sphere surface.
- Each point on the sphere surface has the same probability $W = \frac{\pi R^2}{N}$ to be sampled (This results in a total unnormalised probability πR^2).
- From each selected point starts an inward-directed pseudo particle whose trajectory could pass through the volume of the sphere under measurement.
- Estimating the track length density of the pseudo particle flux within the sphere of unknown volume V according to the following relation

$$\Phi = \frac{\sum_{i=1}^N W_i l_i}{V} = \frac{\pi R^2 \sum_{i=1}^N l_i}{N V} \quad \text{Equation 2.2}$$

Setting V=1 in arbitrary units makes Φ an estimate of the sphere volume.

MC codes such as FLUKA and MCNP can implement this algorithm to produce a volume estimated for a given finite space region.

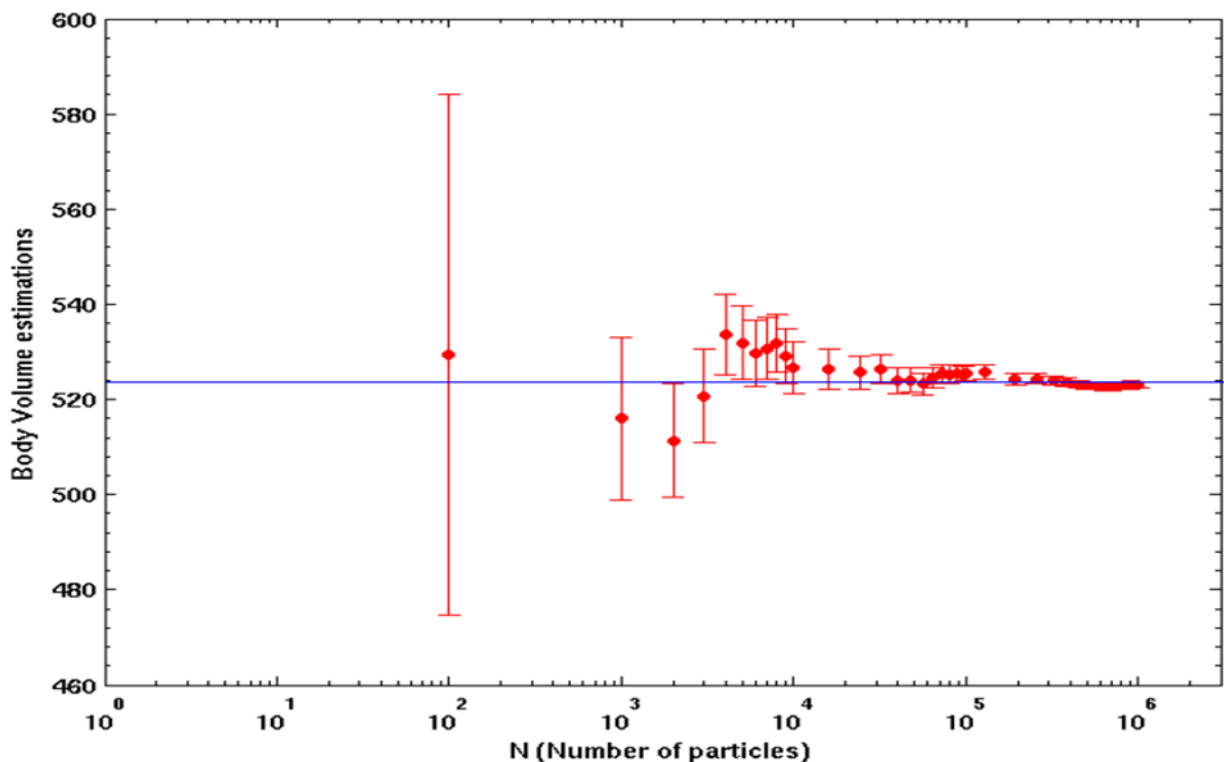


Figure 2.2: The convergence of the sphere estimated volume to the accurate volume (523.60 cm³ blue line) with the increase of the number N of pseudo particles in a ray tracing scan to infer the volume with FLUKA. The error bars of each point measured the dispersion in 1 σ . The best estimate is obtained with a mean of 523.02 cm³ (standard deviation of 0.5320 cm³, N=1e6 pseudo-particles).

Figure 2.2 reports the estimated volume in function of the number N of pseudo particles used in the estimation showing that, as usual in probability sampling, the dispersion is progressively reduced as the number of individuals in the sample grows. Furthermore, the MC method naturally introduces the stochastic nature of the estimate of a quantity very close to the laboratory interpretation of a set of measures.

In the case of volume estimation, the method has both good accuracy and precision; this is not always true for MC codes that have relatively high precision, often reached with a low speed of convergence, but they are not of proven accuracy. Therefore, accuracy depends on the sampling strategy choice and the data's level of uncertainty.

The great advantage of MC methods is in their capability to infer meaningful results even in the case of a complex problem where an analytical solution can not be found, to simplify as in the case of calculating the volume of an object with a very complex shape that does not have an analytical formulation for its volume.

The engine of an MC simulation of the nuclear particles' transport in the matter is the sampling of nuclear interaction from their Probability Distribution Functions. According to the event's PDF nature, different sampling methods optimise the sampling efficiency during a simulation.

As an example, we apply the inverse transformation sampling strategy to the problem of the diffusion of mono-energetic neutrons in a homogeneous media. Sampling a PDF via the inverse transformation is based on the sampling of the uniform distribution U, a PDF that assumes as equiprobable the outcomes of all the real numbers in the range from 0 to 1 to obtain a sample value of a random variable that obeys to a different PDF.

According to the following relation

$$R = \int_{-\infty}^X f_x(x) dx \quad \text{for all } R \text{ in } U(0,1] \quad \text{Equation 2.3}$$

the inverse transform sampling stated that for each value of R in U, it is possible to obtain a value X sampled from another PDF.

In the case of a neutron of energy E, the probability P(l) of colliding with a nucleus of a homogeneous media (resulting in a scattering) after diffusing on a path of length l from the source is

$$P(l) = \int_0^l \Sigma_t e^{-\Sigma_t s} ds \quad \text{Equation 2.4}$$

where Σ_t is the macroscopic cross-section of the media, using the inverse transform

$$\xi = \int_0^l \Sigma_t e^{-\Sigma_t s} ds$$

Being ξ a random number sampled in the uniform distribution U, calculating the integral and obtaining l the collision distance

$$l = \frac{1}{\Sigma_t} \ln(1 - \xi) = \frac{1}{\Sigma_t} \ln(\xi') \quad \text{Equation 2.4}$$

that is a well-known relationship.

This mechanism is specialised for the convenient sampling of the different PDFs that define the MC simulation, such as primary particles emission, their transport in the various materials, the generation of secondary particles at a point of interaction with nuclei, the amount of energy deposited along a particle track and the termination of a particle history are decision that the codes take sampling the relative PDF.

The code attributes a probabilistic weight to each event in the random sequence of a primary particle. Consequently, it could sum up the weight that fulfils a user-defined set of conditions building an estimate of a conditional PDF for a given physical quantity such as reaction rate, particle fluxes, currents, and energy depositions. Those conditional PDFs are generally called “estimators” or “tallies” and are a part of the simulation results.

The definition of a simulation in an MC code for nuclear particle transport

Generally speaking, the input data for an MC code are related to the source’s definition, the system’s geometry under simulation, the material density and composition, and the estimators of the quantity of interest.

Source Definition

During MC simulations, the particle state is regarded as a point P in nine-dimensions phase space that the code saves in a vector as follows

$$P(x, y, z, u, v, w, E, t, Wt) \quad \text{Equation 2.5}$$

Where [x y z] defines the spatial position; [u v w] are the direction cosines of the particle trajectory; E is its actual energy; t is the time of flight relative to its birth if primary or the birth of the primary particle if secondary; Wt is its statistical weight.

Therefore, the source definition deals with the input of data that defines a subset of the phase space that delimits the primary particle’s emission region. Consequently, the information regarding the spatial source distribution (point, surface or tridimensional source), the direction of emission (isotropic, angular-depended, collimated), the time duration (pulsed, stationary), and the energy spectrum are all defined as PDFs that the code sample to establish the initial point of the primary particles at emission time.

For example, suppose the user defines a mono-energetic, isotropic and time-stationary point source. In that case, all the primary particles will be emitted at the same energy, time, and position. What differentiates the source particle is the initial direction of flight that is equiprobable in all directions.

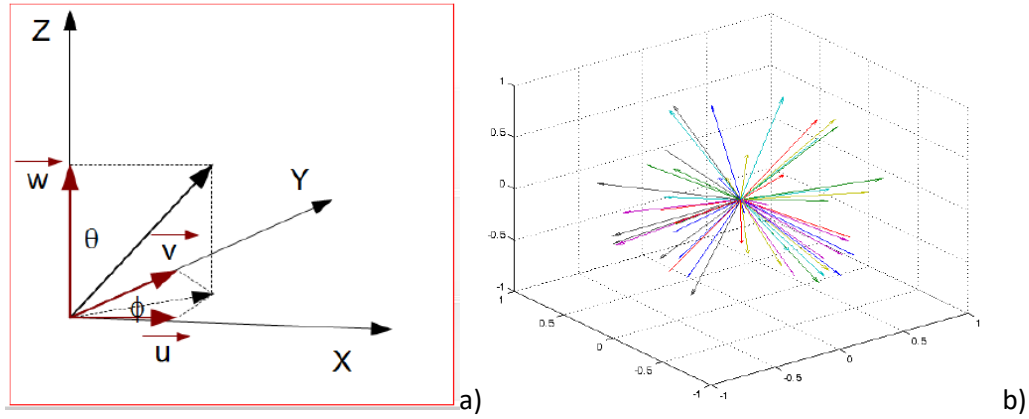


Figure 2.3: a) Graphical representation of the relationship between direction cosines and azimuthal (ϕ) and polar (θ) angles; b) Some particle's direction of flight from an isotropic point source.

Figure 2.3a shows the relation of the direction cosines for the generic flight direction of a primary source particle with the azimuthal (ϕ) and polar (θ) angles. Accordingly, the sampling algorithm operated in the subsequent four steps:

1. *get* ξ in $U(0, 1]$;
2. $|\vec{w}| = \cos \theta = -2 \xi + 1$;
3. $|\vec{u}| = \sqrt{1 - \cos \theta} \cos \phi = \sqrt{1 - \cos \theta} \cos(2\pi\xi)$;
4. $|\vec{v}| = \sqrt{1 - \cos \theta} \sin \phi = \sqrt{1 - \cos \theta} \sin(2\pi\xi) =$;

Iterating N time between steps 1-4, we sampled N particle's directions changing the cosines accordingly with the outcome of the uniform sampling in U. Figure 2.3b reports some particle' flight directions for an isotropic point source sampled according to the previous algorithm implemented in an Octave script.

It is worth mentioning that in step 1, we need to use a specific sampling technique to random sampling ξ from the uniform distribution U. Being such an algorithm at the Heart of the MC codes, it is necessary to express some consideration on this topic without going beyond the scope of the present work. The class of algorithms able to generate a vast random sequence of numbers avoiding correlation does not exist. Therefore, referring to them as Pseudo Random Numbers Generators (PRNG) is more appropriate. The PRNG are the basis of the encryption technics that make E-commerce, bank transaction on the internet and many other related activities safe and reserved. Due to their critical mission, the commercial PRNG standards are very stringent, and they must pass a severe suite of numerical tests before being declared safe. Fortunately, the PRNG used for scientific purposes requests less stringent standards. For example, FLUKA adopts a 64-bit version of the Marsenna Twister [27], and the users of MCNP can choose between four flavours of Linear Congruential PRNG [28]: none of these two kinds of PRNGs passes the standard test suite. However, they are considered numerically adequate for MC simulations.

Geometry definition

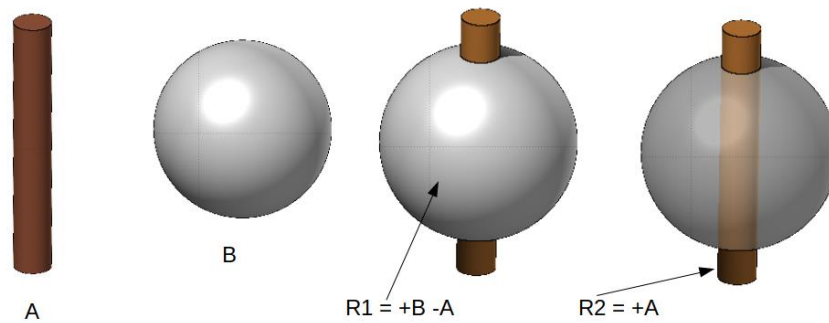


Figure 2.4: Combinatorial Geometry: Cylinder A and sphere B were combined to define two regions. The region R1 is the set of points inside the volume of B not in common with A. The region R2 are the set of points contained in the volume of A.

Using the constructs of Combinatorial Geometry (CG), the user can build very detailed and realistic 3D models of the geometric layout. The basis of CG is the solid bodies defined by the Analytic Geometry equations. The user can define a set of labelled bodies specifying their dimensions and positions and type in the input. Each solid is considered a set of space points within its volume. The user combined such sets to form a region of the space that shaped the geometry layout.

Figure 2.4 reports an example of the construction of two regions according to CG rules. First, cylinder A and sphere B were defined. The sphere B is centred in the origin of the reference system with radius R. Cylinder A is defined to have its middle height at the origin. The region R1 is the set of space points contained in B that are not in common with A, namely $+A-B$. The region R2 is the set with points contained in B as $R1= +B$. This kind of representation is very compact and efficient for the code representing the whole geometry.

During the simulation, the navigation routines established the position of each transported particle within the geometry from the emission to termination, registering all events requested by the users to estimate the quantity of interest.

The CG simplifies the definition of the geometry of a complex model because it is relatively simple to implement computer scripts to generate this part of the input. Recently, the FLAIR code [25] has changed from a dedicated pre and post-processor for FLUKA to an “advanced, user-friendly interface for several Monte Carlo codes”. Figure 2.5 shows the visualisation of the TRIGA reactor [29] core geometry from the MCNP input using FLAIR.

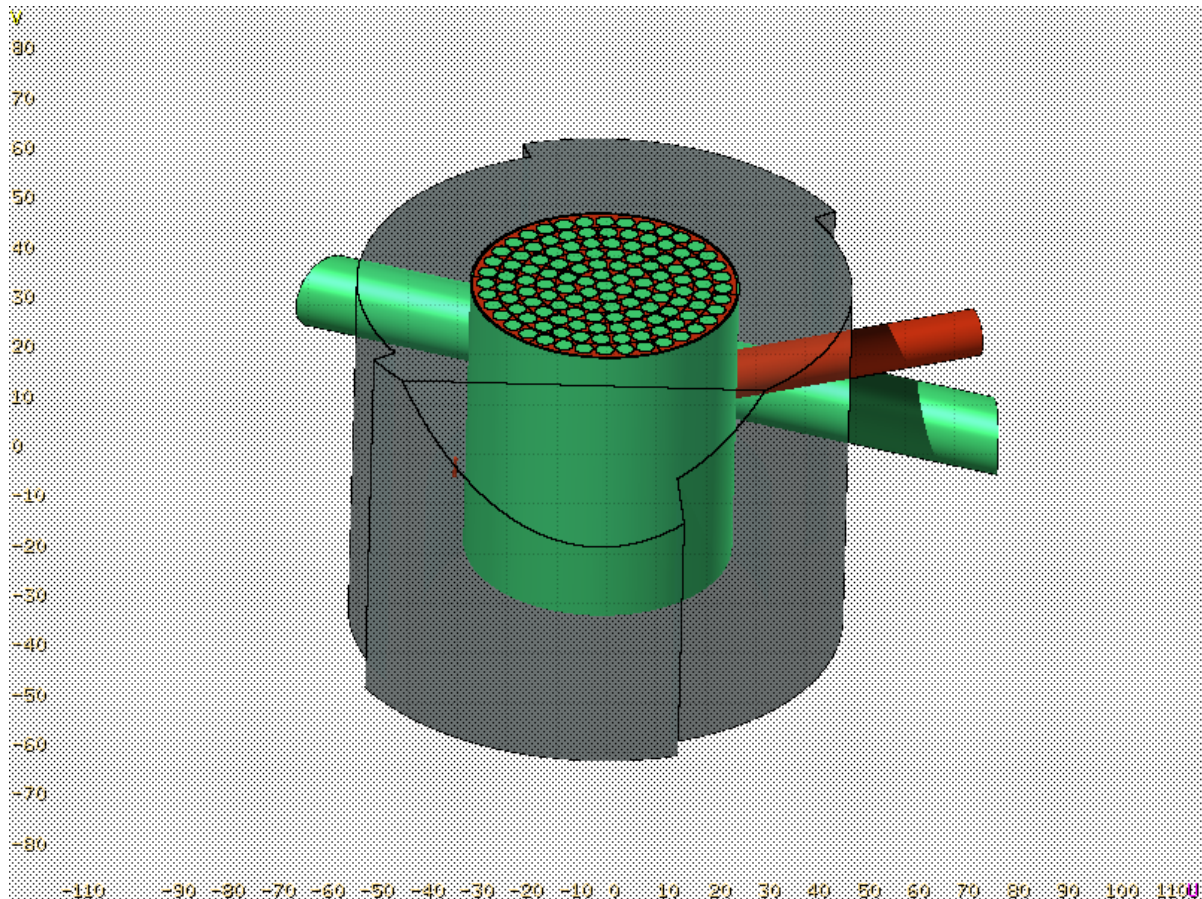


Figure 2.5: FLAIR rendering of the TRIGA [] reactor core canister model. The graphite reflector and the water pool regions were rendered highly transparent to allow the core visualisation.

Materials definition

The interaction of the nuclear particles and high-energy ions during their transport in matter depends on the kind and quantities of atoms in the material. For example, charged particles and ions interact with the external electron cloud of the material and, sometimes, undergo electrostatic repulsive interaction against the partially shielded nuclear charge with significant trajectory modifications. When the kinetic energy is sufficient, the particles and ions penetrate or ablate one of the material nuclei activating a nuclear reaction channel.

Neutral particles do not interact with the external electron cloud or nuclear charge but undergo a head-on collision with the nucleus. For example, neutron elastic interaction with a nucleus has a kinematic that can be modelled as the hit of two rigid spheres of different mass [30].

Whatever the nature of the transported particles, the expected number of interactions depends on the material composition and density that allows the Calculation of the macroscopic cross-sections of the materials. For example, the macroscopic cross-sections have the dimension $[\text{cm}^{-1}]$ and can be regarded as the spatial frequency with which a particle can interact within the material.

Consequently, it is necessary to define the elemental composition and the bulk density of each material involved in the simulations. When neutrons (or other neutral particles) are relevant in the simulation, the material composition must be specified at the isotopic level.

Each geometric region will be associated with one material, and once the simulation starts, the particles will be transported from the source to the rest of the geometry. Each time a particle crosses the boundary within two regions, the navigation routines of the codes change the media composition accordingly to consider the new transport condition peculiar to that specific region.

Estimators

Before introducing the concept of the estimator in an MC simulation, it is convenient to discuss the concept of “history”, which is at the very base of the inference mechanism of the MC codes. We can define “particle history” as the collection of all the events involving a primary particle and its progeny, from the birth event of the emission from the source to the termination of its last child.

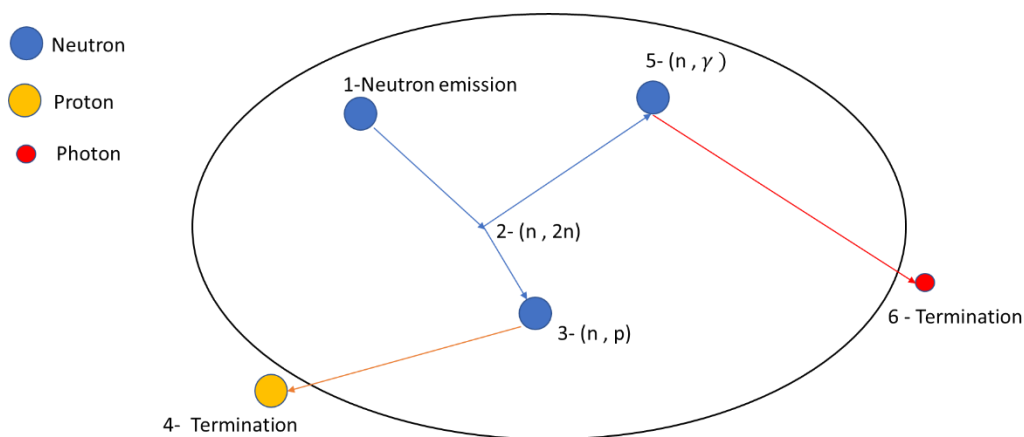


Figure 2.6: Schematic representation of a particle history with six events before termination (see text).

For example, Figure 2.6 reports the scheme of a neutron history: the first event is its emission, followed by the first track trajectory to event 2. In event 2, the neutron interacts with a nucleus activating the nuclear reaction channel for $(n,2n)$, generating two neutrons. On the path of its track, the first neutron interacts with a nucleus, and in event 3, via (n,p) reaction, terminated. The proton emitted in event 3 has a track that conducts him outside the zone of interest for the simulation and is terminated in event 4. The code rolls back to event 2, recalls from the memory the coordinates for the transport of the second neutrons generated in the $(n,2n)$ reaction and starts its transport. The neutron is captured by a nucleus via an (n,γ) reaction and terminated on its track. The γ photon born in event 5 is then transported and terminated when it crosses the boundary that limits the zone of interest for the simulation.

The MC code estimators are based on the count of the number of particle tracks entering the volume of user-selected regions, the weighting of their statistical importance, and according to the flux definition, their track lengths. The particle fluxes and current are at the basis of the

derivation of quantities as energy deposition on a material, fission rate, dose, and saturation yield in the production of nuclides via a given nuclear reaction channel.

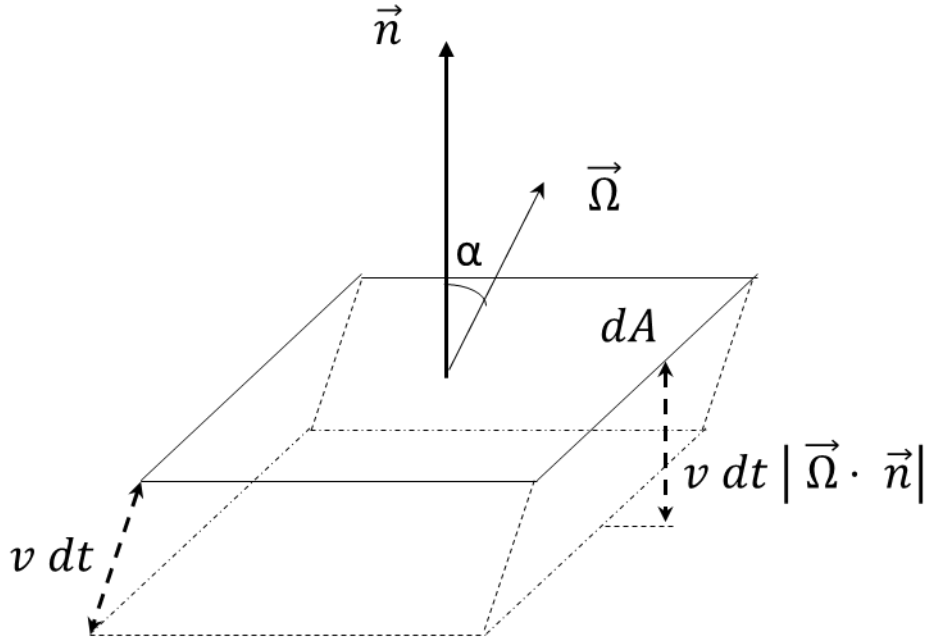


Figure 2.7: Estimation of the particle current crossing a surface. The MC code calculates the projection of the particle's track length vector $\vec{\Omega}$ on the surface's normal vector \vec{n} when crossing surface A. The track length is computed as $l = v dt$ where v is the particle's speed. The track length projection on \hat{n} is $v dt |\vec{\Omega} \cdot \vec{n}|$. The estimator summed the particles' contributions to estimate the total particles' current.

Figure 2.7 shows the mechanism used by the MC code to estimate the contribution of a particle track to the current of particles crossing a user-selected surface. The particle current I is obtained by integrating on the phase space the scalar current $J(\vec{r}, E, t, \mu)$ according to

$$I = \int_A \int_{\mu} \int_t \int_E J(\vec{r}, E, t, \mu) dE dt d\mu dA;$$

$$J(\vec{r}, E, t, \mu) = |\mu| \Phi(\vec{r}, E, t) A;$$

$$|\mu| = |\vec{\Omega} \cdot \vec{n}| = |\cos \alpha|;$$

Where $\Phi(\vec{r}, E, t)$ is the particle's vector flux, and μ is the cosine of the angle α (see Figure 2.7) between the vector of the surface's normal \vec{n} and the normal of the particles track direction $\vec{\Omega}$.

Finally, the MC code estimates the particle current \bar{I} crossing surface A according to

$$\bar{I} = \sum_{i=1}^N W t_i |\mu|_i \quad \text{Equations 2.6;}$$

Where $W t_i$ is the track statistical weight, the user could optionally subdivide the contributions to the current by energy, time and angular binning.

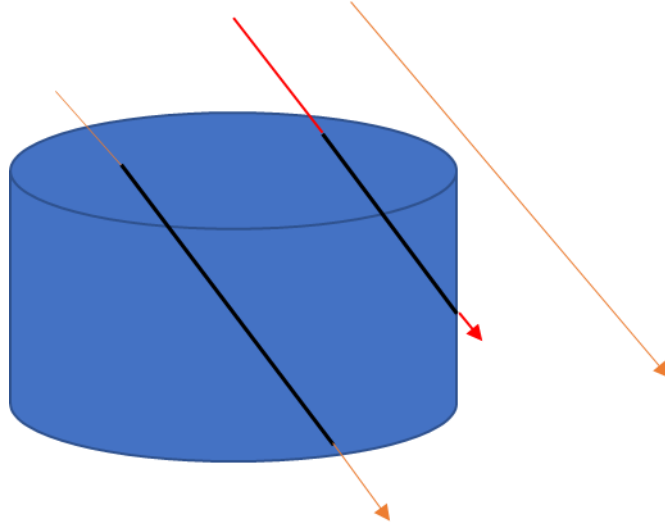


Figure 2.8: Estimation of the particle flux averaged on a volume. The particles crossing the boundaries of the cylindrical region (denoted by the black colour of the vector) contribute to the flux estimate according to Equation 2.7.

The other fundamental estimator is the particle flux ϕ averaged on the volume V of a region, which can be defined as

$$\phi = \int_V \int_t \int_E \Phi(\vec{r}, E, t) dE dt \frac{dV}{V} ;$$

The MC code estimate fluence $\bar{\phi}$ according to

$$\bar{\phi} = \frac{1}{V} \sum_{i=1}^N v_i t_i W t_i = \frac{1}{V} \sum_{i=1}^N l_i W t_i \quad \text{Equations 2.7;}$$

summing the non-null contributions given by the N sample particles in terms of the product of track length l by statistical weight Wt (see figure 2.7), the code obtains the estimate $\bar{\phi}$ of the fluence per N particles.

In some problems, it is helpful to estimate the fluence Φ_A of the particles that cross a surface of area A , which is defined as

$$\Phi_A = \frac{1}{A} \int_A \int_t \int_E \Phi(\vec{r}, E, t) dE dt dA;$$

According to Figure 2.9, generating a region of small thickness δ using a second surface in front of the crossing surface, we obtain the expression of the track length of the i th particle as $l = \frac{\delta_i}{\cos \alpha}$, being the region volume $V = A \delta$, we can obtain an estimate of $\bar{\Phi}_A$ of the fluence for surface crossing particles substituting the values of l and V in Equation 2.7

$$\bar{\Phi}_{A\delta} = \frac{1}{V} \sum_{i=1}^N l_i W t_i = \sum_{i=1}^N \frac{1}{A\delta} \frac{\delta_i}{\cos \alpha} W t_i;$$

that is, the fluence averaged on the volume of the region of thickness δ . Now, the estimate for $\bar{\Phi}_A$ is obtained in the limit of $\delta \rightarrow 0$ as follows

$$\bar{\Phi}_A = \lim_{\delta \rightarrow 0} \sum_{i=1}^N \frac{1}{A\delta} \frac{\delta_i}{\cos \alpha} Wt_i = \sum_{i=1}^N \frac{1}{A} \frac{Wt_i}{|\mu_i|A} \quad \text{Equation 2.8;}$$

It is noteworthy that Equations 2.6 to 2.8 are unnormalised estimates of the current and fluence. Usually, the code operates a normalisation dividing the estimator score by the total number of primary particles used in the simulation. The normalised results are in the form of conditional probabilities with units as [$\text{cm}^{-2} \text{ primary}^{-1}$] (fluence) and [primary^{-1}] (current).

Thus, when the user obtains a score for flux in the volume of a given region equal to $0.1 [\text{cm}^{-2} \text{ primary}^{-1}]$, one primary particle emitted by the source has an estimated probability of reaching that region of 1 tenth. If the primary source intensity is $10000 [\text{p/s}]$ then the flux in the region volume is estimated to be $0.1 [\text{cm}^{-2} \text{ primary}^{-1}] \times 10000 [\text{primary s}^{-1}] = 1000 [\text{cm}^{-2} \text{ s}^{-1}]$.

Since the MC results are expressed as the means of the estimated quantities, also the associated relative error $E_r = \frac{\sigma}{\mu}$, computed as the ratio of the standard deviation σ and the mean μ , is reported. The E_r is an index of the degree of the precision of the estimation. The accuracy of the results strongly depends on the choice of the sampling strategy and the level of uncertainty of the data.

Biasing techniques

Often to overcome the low estimator convergence to a good precision that requests a long computational time, a biasing technique was applied. Such a technique introduces a bias in the statistical weight of some events in the particles' histories: rare events' frequency will be artificially increased because the user is more interested in it than in the more common event that appears in the unbiased distribution frequently. The biasing scheme must contain some weight compensation to produce a result that is statistically congruent with the unbiased one.

A classic example is the so-called geometry splitting, where particles directed toward a more statistically significant (for the user) region were increased according to a user-selected region's importance. Conversely, particles directed toward less important regions were reduced in number.

In geometry splitting, the weight compensation mechanism that leads to the correct result is based on the event of crossing the boundary between two regions of different importance.

We are considering two regions, N and M, with a common boundary and respective importances, I_N and I_M . When a particle crosses the boundary between the two regions, according to the ratio $v = \frac{I_M}{I_N}$

1. If $v = 1$, the transport continue without modifications.
2. If $v < 1$, the particle moves to a region of lower importance, then Russian roulette is played. The track could survive with a probability v , and it continues the transport with a weight of Wt/v . Otherwise, it is killed with a probability of $1 - v$.
3. If $v > 1$, the particle moves to a region of higher importance, and then the original track is split into v particles with weight equal to w/v .

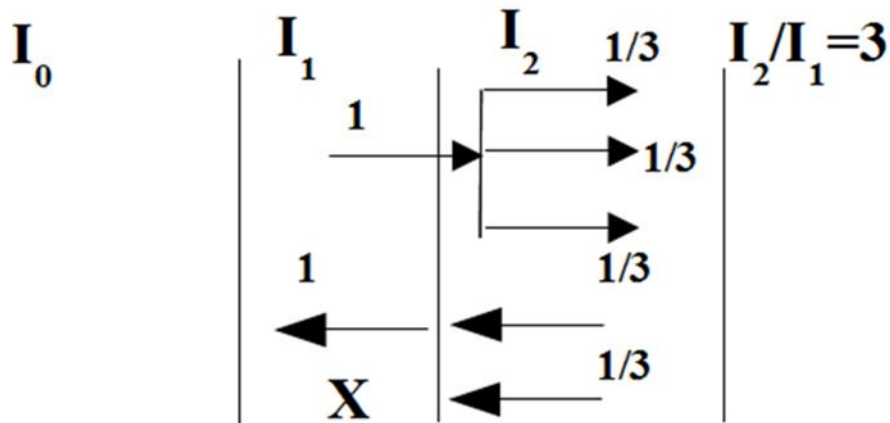


Figure 2.9: Geometry Splitting biasing scheme applied to particles that cross the common boundary between two regions having importance I_1 and I_2 and their importance ratio $I_2/I_1=3$.

Figure 2.9 shows that crossing the boundary from a region at lower importance I_1 to the region I_2 at higher importance I_3 , being, for example, the importance ratio $I_2/I_1= 3$, the particles will be split into three particles with the same trajectory but with lower statistical weight equal to $Wt = 1/3$. From that point on, the three particles differentiate their histories, allowing the more extensive exploration of the phase space zone of interest to the problem.

A particle crossing the boundary in the opposite direction passes from a zone of higher to one of lower importance. Russian roulette is played, and if the particle survives, its weight becomes $Wt = 1/3$ and continues its history. Otherwise, the particle is killed. The Russian roulette particle killing decreases the number of histories in the region of the less important problem.

At a constant number of sample particles, a more significant fraction of the simulation time is used to follow those particles giving more meaningful information and accelerating the convergence of the results.

FLUKA parallel execution

The precision of the Monte Carlo results depends on the number of primary source particles used for the simulation [16 -Chapter 5]. Higher precision is generally obtained by increasing the number of primary particles at the cost of higher calculation time. We implement FLUKA on the high-performance computing system CRESCO (Computational Research Centre on COMplex systems) [19] to shorten calculation time, executing the simulation in the “embarrassing parallel” [31] modality, resulting from several replicas of the same problem having different seeds for the pseudo-random number generator are obtained.

The results from each replica are like independent measurements of experimental quantities, and their mean μ and standard deviations σ are the final simulation results. We quantify the attained precision level using the relative error $Er= \sigma/\mu$. In an embarrassing parallelism scheme, the overall number of primary particles P , connected with the simulation precision, is

$$P = N p; \quad \text{Equation 2.9}$$

with

N = number of CPU

p = number of particles per CPU (on which run a simulation replica)

P = overall number of particles in the simulation

This calculation methodology also allows the individual analysis of each source term, optimising precision and simulation time by changing the number of particles and CPUs.

Conclusions

MC codes can infer from the transport of statistically meaningful particle samples in a complex system selected properties such as flux and reaction rate. However, their eminently stochastic approach to very heterogeneous systems allows the solution of transport problems that cannot be implemented in the so-called analytical code that needs to solve, even numerically, the Boltzmann equation.

The MC estimations are obtained as the mean and the standard deviation of a conditional probability density function integrated into a user-defined region of the phase space.

The major drawback of MC codes is the slow rate of convergence that is partially compensated by adopting the biasing techniques and using parallel computing systems.

According to the requirements for calculating the high energy particle interactions at relatively low fluxes, in this study, FLUKA is preferred to MCNP. However, being MCNP a reference code for neutronics, we will present some results based on it, as requested in the following chapters.

Chapter 3 – The atmospheric neutrons: comparisons between FLUKA models and measurements from the ground station

Introduction

Our initial intention was to investigate the FLUKA and MCNP capabilities to simulate the atmospheric particle showers of the GCR as the first step forward in understanding the potentiality of those simulation tools for aerospace.

The author has years of experience using those codes in nuclear reactor physics [31 -32] and target design for accelerators [34-36] and aerospace [37] and examining the manuals of MCNP and FLUKA, discovered a FLUKA-dedicated tool for the simulation of GCR ions shower in the atmosphere. Furthermore, it is unclear if the MCNP release license allows non-US institutions to use it for aerospace applications. Consequently, we decided to start directly using FLUKA.

In any case, MCNP is one of the state-of-art MC codes in neutronic applications. Therefore, we continue to use it to compare the neutron irradiation facility in research nuclear reactors with the charged particle irradiation carried out on accelerators and in orbital conditions. Some results will be presented in the following chapters.

The following paragraph reports the modelling and results of applying FLUKA's GCR tool to estimate the flux of the secondary neutrons at given geographic positions that host measurement stations in the USA [38]. The FLUKA results have been verified against the results furnished by an implementation of the Below, Struminsky, and Yanke (BSY) semi-empirical model [38] carried out during a Master's Thesis [39] under the author's tutorship. The simulation outcomes agree with the experimental results and the BSY model confirming our capability to manage FLUKA in aerospace applications.

Generalities on the FLUKA model to estimate local GCR ion shower at various altitudes in the Earth's atmosphere and surface

As seen in Chapter 1, the GCRs that approach the medium in the proximity of our planet have already been modulated by the Sun's activities (Period of Solar cycle) and by the interaction with the solar wind condition. Near Earth, the geomagnetic field further alters the trajectory of the GCR particles, modifying their energy spectra and intensity. The FLUKA's GCR tools model the interaction with the geomagnetic field simulating then the penetration of the ions in the atmosphere from an injection point at 71 km above the Earth's mean radius (6378.14 km) down to the planet's surface. The model could include an above portion of outer (void) space ranging from 71 to 120 km.

According to Table 3.1, which reports the classification of the orbits around Earth, the maximum altitude admitted by the FLUKA model is well below the LEO (Low Earth Orbit).

Consequently, apart from some evaluation of a local source of atmosphere escaping neutrons to be used in subsequent calculations to be coupled with higher orbits radiation source modelled as an example by SPENVIS, the main application of the GCR tools is related to the air shower-up to Earth's ground.

Table 3.1 Earth orbits classification

Denomination	Minimal Altitude	Maximum Altitude	
Low Earth Orbit (LEO)	200 km	2000 km	Space station (Mir, ISS)
Medium Earth Orbit (MEO)	2000 km	35786 km	Telecommunication (handover fleet)
Geostationary (or Geosynchronous) Earth Orbit (GEO)	35786 km		Telecommunication
High Earth Orbit and Highly Elliptical Orbit (HEO)	35786 km		Telecommunication for regions near the poles

Model geometry

The template layout used to model cosmic ray showers in the Earth's atmosphere includes the whole planet simplified as a sphere of the average Earth's radius, with the atmosphere composed of 100 spherical layers from the Earth's surface up to 70 km from the sea level. The final "outer space boundary" is at 120 Km of altitude.

The pre-processing code **atmloc** specialises the template of the geometry of the atmospheric model around the geographical coordinates furnished by the user excluding from the geometry the atmospheric regions with a negligible contribution to the local GCR shower.

Figure 3.1 reports a schematic view of the final layout obtained at the end of the pre-processing phase for a location in the northern hemisphere. Three coaxial truncated cones are added to the one hundred spherical shells representing the atmosphere layers. Two cones have their vertex in the Earth's centre, the bases are out of the atmosphere, and the heights are in the direction of the Earth's radius, passing through the north pole for a region located in the northern hemisphere (to the south pole in the southern hemisphere), the third cone with opposite orientation (i.e. with the vertex out in the atmosphere at the same elevation as the base of the other two cones) and with the height in a direction passing to the heart diameter at the south pole (north pole for the south hemisphere).

Operating with the CG on the above-described bodies, spherical crown regions are obtained using as boundaries the inner and the outer coaxial cones surfaces spiked at the Earth centre and the third cones tangent at the user-defined geographic location for the one thousand spherical shells.

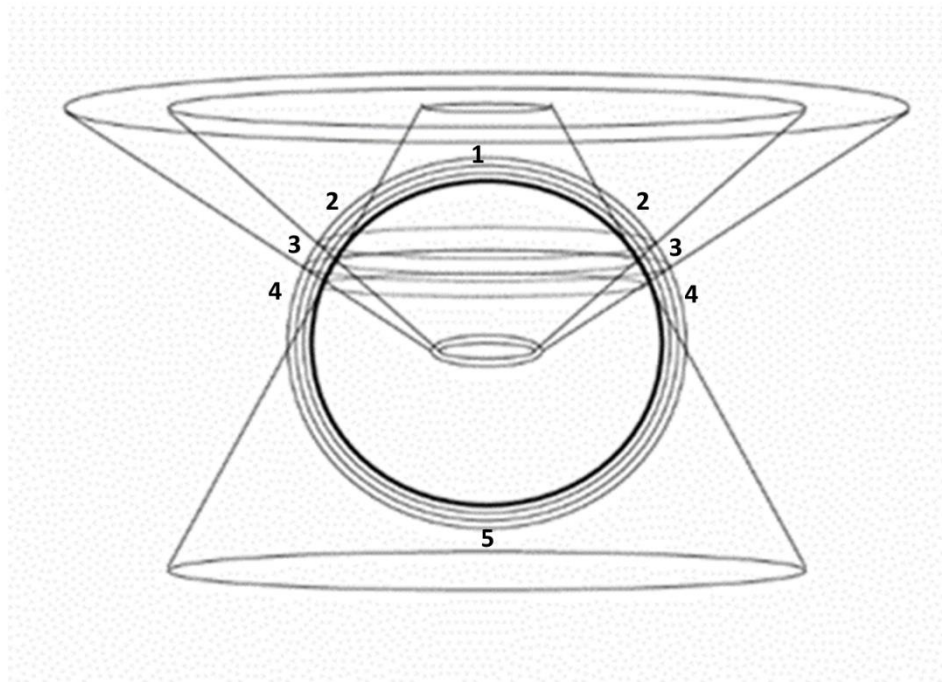


Figure 3.1 - The geometric layout specialised for the user-defined location on Earth's surface.

According to Figure 3.1, the model regions are divided into five sectors by the three cones. Sector 3 is between the two coaxial cones and defines the regions of interest to estimate the progressive penetration of the GCRs and their secondaries into the Earth's atmosphere near the location of interest.

Sectors 2 and 4 define the atmospheric shells between one of the two coaxial cones and the cone in the opposite direction. These additional regions are needed to consider the primary and secondary particles that reach the region of interest in Sector 3 from side trajectories originating from those regions.

Consequently, the spherical crown regions of Sectors 1 and 5 have a negligible probability of generating particles with trajectories that could reach Sector 3. Thus, the users marked them as filled with "black holes" material and recognised by FLUKA as regions where every kind of particle will be terminated when entering to avoid wasting computational time following useless particle histories.

During the pre-processing phase, atmloc also calculates the area associated with the spherical boundary surface between layers of Sector 3. Then the areas are used to normalise the estimator scores (flux, reaction rates, doses) directly at the user-selected GCR intensity.

Figure 3.2 reports geometric cross-sections of the full-scale Earth atmospheric model rendered by FLAIR's graphical processor. Figure 3.2a shows the whole Earth system, previously represented in the schematic view of Figure 3.1, in its natural proportion, where the set of primary and side atmospheric layers appear as unresolved black regions. In contrast, the space immediately above the atmosphere is a white layer.

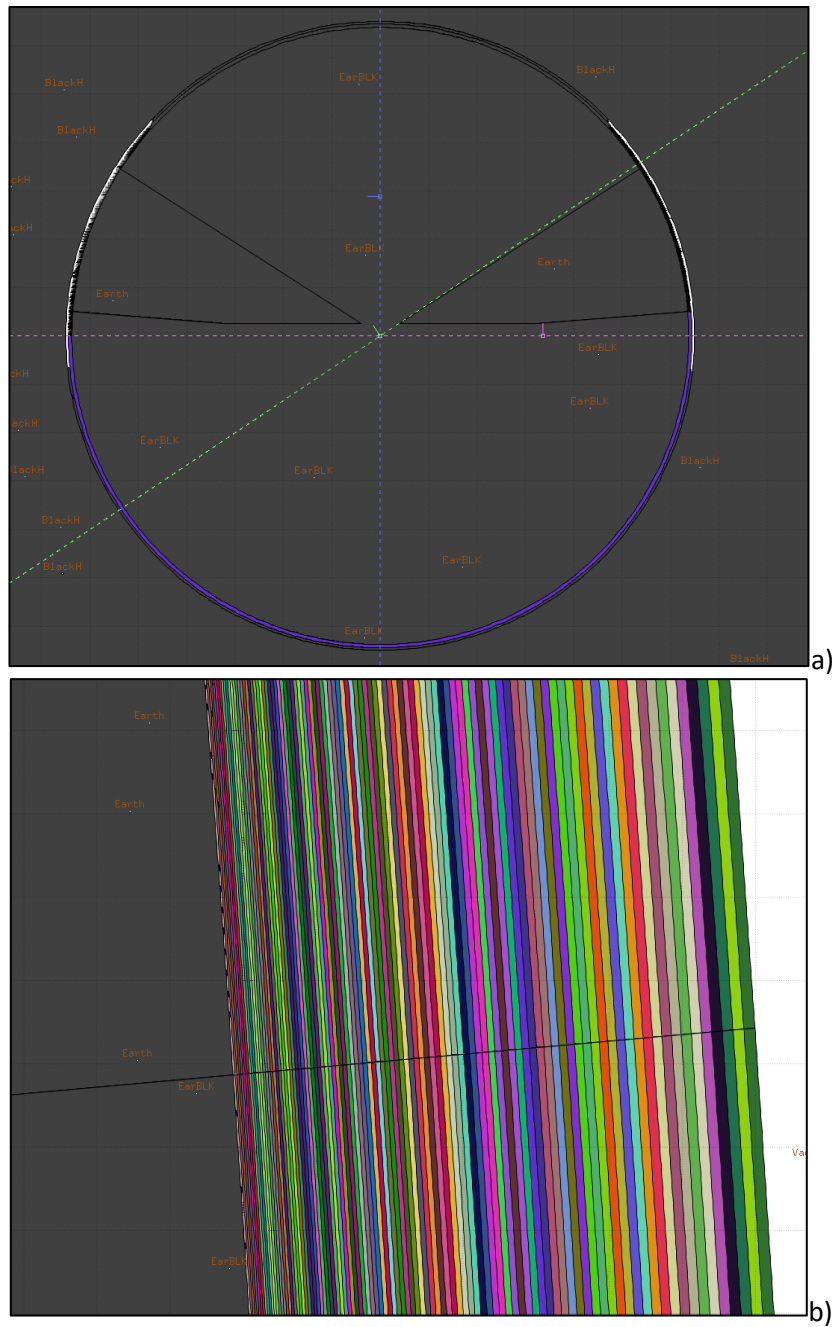


Figure 3.2 – Geometric layout of the FLUKA’s atmospheric model: a) A cross-section that includes the whole Heart, the atmosphere and the boundary with vacuum; b) A magnification of the main atmospheric layers near the border with the side atmospheric layers (whose height is 70 km).

Figure 3.2b reports the zoom on one of the halves of the main atmospheric layers near the boundary with the side layers. The one hundred layers of the atmosphere appear as regions of different colours filled with varying compositions of air and density according to the altitude (see the Materials paragraph). At this magnification level, the layers’ curvature appears minimal, as in flat atmospheric models. However, the distance from the last atmospheric layer (green colour, rightmost position in Figure 3.2b) to the black-coloured Earth’s surface is 70 km.

Materials

Concerning the model materials, the same air composition has been assumed for all the atmospheric regions (Nitrogen 75.56 %wt, Oxygen 23.16 wt%, Ar 1.28 wt%) with a layer density change calculated according to Table 3.2 specification.

Table 3.2 - Air material specification for the FLUKA atmospheric layer according to U.S. Standard Atmosphere depth.

FLUKA region	km from sea level	US St. Atm. Depth [g cm-2]	FLUKA region	km from sea level	US St. Atm. Depth [g cm-2]	FLUKA region	km from sea level	US St. Atm. Depth [g cm-2]
1	70	0.092	35	31.6	9.367	69	10.7	242.777
2	68.5	0.108	36	30.8	10.54	70	10.2	260.107
3	67.1	0.126	37	30	11.849	71	9.8	278.093
4	65.6	0.146	38	29.2	13.309	72	9.4	296.729
5	64.2	0.17	39	28.4	14.937	73	8.9	316.007
6	62.8	0.198	40	27.7	16.748	74	8.5	335.921
7	61.5	0.23	41	26.9	18.763	75	8.1	356.46
8	60.1	0.266	42	26.2	21.004	76	7.7	377.615
9	58.8	0.308	43	25.5	23.492	77	7.3	399.374
10	57.5	0.356	44	24.8	26.255	78	6.9	421.727
11	56.2	0.411	45	24.1	29.29	79	6.6	444.661
12	55	0.474	46	23.4	32.613	80	6.2	468.163
13	53.8	0.546	47	22.7	36.244	81	5.8	492.219
14	52.5	0.628	48	22.1	40.205	82	5.5	516.815
15	51.4	0.722	49	21.4	44.516	83	5.1	541.936
16	50.2	0.828	50	20.8	49.201	84	4.8	567.566
17	49.1	0.95	51	20.2	54.283	85	4.4	593.691
18	47.9	1.088	52	19.6	59.785	86	4.1	620.295
19	46.8	1.245	53	19	65.733	87	3.8	647.359
20	45.7	1.423	54	18.4	72.152	88	3.4	674.869
21	44.7	1.625	55	17.8	79.068	89	3.1	702.807
22	43.6	1.854	56	17.2	86.506	90	2.8	731.155
23	42.6	2.112	57	16.7	94.493	91	2.5	759.898
24	41.6	2.404	58	16.1	103.057	92	2.2	789.016
25	40.6	2.734	59	15.6	112.224	93	1.9	818.493
26	39.6	3.106	60	15	122.023	94	1.6	848.311
27	38.7	3.525	61	14.5	132.482	95	1.3	878.453
28	37.7	3.996	62	14	143.628	96	1.1	908.9
29	36.8	4.526	63	13.5	155.489	97	0.8	939.636
30	35.9	5.121	64	13	168.094	98	0.5	970.643
31	35	5.789	65	12.5	181.471	99	0.3	1001.903
32	34.1	6.538	66	12	195.646	100	0	1033.4
33	33.3	7.378	67	11.6	210.649			
34	32.4	8.317	68	11.1	226.507			

GCR Source

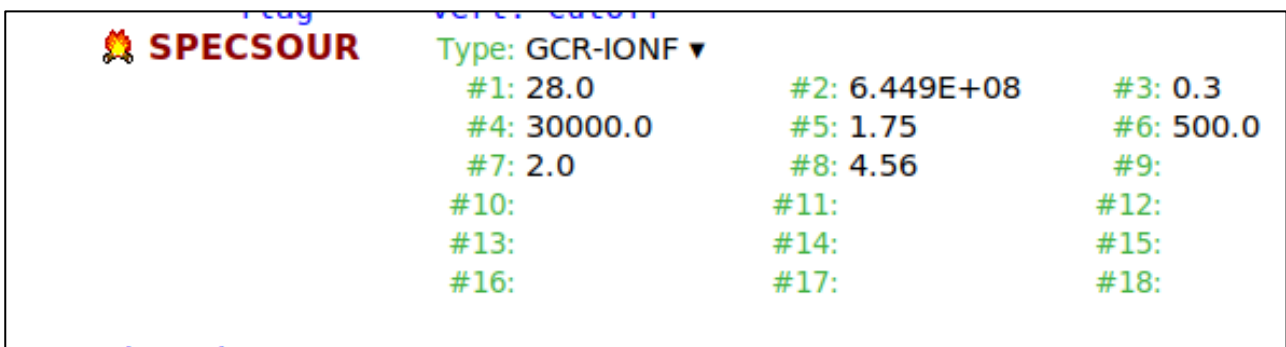
Before we discuss the set-up of the GCR source, it is important to stress that all the input directives of FLUKA originate from the FORTRAN fixed format cards. Originally, each card had six numerical fields (WHAT) and a character field (SDUM). When a directive requests more than one card, the user places the continuation symbol '&' to continue the data input on a new card—a blank WHAT input field often means that the code assumes a default value.

Due to the vast transport conditions allowed by FLUKA to speed up the Calculation without incurring wrong approximations or missing some crucial settings, the code has several default settings that meet the typical simulation requirements called DEFAULT. Thus, we use the DEFAULT setting called “Precision”, adding some particular setting for the high-energy ions transport in the Calculation executed for this argument.

Implementing a complex model by directly editing the FLUKA input file is time-consuming and error-prone. Fortunately, the user has the aid of the FLAIR pre-processing code in which the users can insert all the directives in free format. After syntax checking, the code writes the final input in a fixed format. It also allows the 3D geometry visualisation and the use of geometric sections in orthogonal projection to debug the geometry layout.

The GCR ions source can be implemented using the GCR-SPE option of the SPECSOUR directive. SPECSOUR (SPECial SOURce) is the general card to define sources as colliding beams, galactic cosmic rays, solar particle events, synchrotron radiation, and multiple beams using up to 18 entries (3 consecutive cards).

Table 3.3 reports an example of SPECSOUR input defining a CGR source. Figure 3.33 shows the FLAIR’s SPECSOUR card entries to call the GCR source, and Table 3.3 reports the meaning of each entry.




 SPECSOUR	Type: GCR-IONF ▼		
	#1: 28.0	#2: 6.449E+08	#3: 0.3
	#4: 30000.0	#5: 1.75	#6: 500.0
	#7: 2.0	#8: 4.56	#9:
	#10:	#11:	#12:
	#13:	#14:	#15:
	#16:	#17:	#18:

Figure 3.3 – Definition of the ion’s GCR source at an injection point above Houston using the FLAIR processor.

Table 3.3 – Definition of all particles flux GCR source using the SPECSOUR card

		Value	
Card 1	What(1)	28	Definition of the ion composition (What (1)= $Z_{max} + Z_{min} * 100$ with $1 < Z < 28$), FLUKA reads the spectrum from files with the naming convention $Z < \text{PhiMV} > .\text{spc}$. For example, 01phi0465.spc is the spectrum for hydrogen ions modulated by a Solar Event minimum at 465 MV. Those files are combined to produce the overall spectrum between Z_{min} and Z_{max} . These spectra do not have a geomagnetic cut-off, and FLUKA executes a calculation of rigidity cut-off according to a user-selected description of the geomagnetic field.
	What(2)	6.449e8 cm	Ion Injection Radius in cm (the earth centre is at the origin of the FLUKA reference system);
	What(3)	0.3	Ion minimum energy (GeV)
	What(4)	30000.0	Ion maximum energy (GeV)
	What(5)	1.75	Spectral index for sampling (below transition energy)
	What(6)	500.0	Transition energy (GeV) for sampling (above it, sample from $1/E$)
	SDUM	GCR-IONF	Specify that the galactic source is expressed as all particles' flux
Card 2	What(1)	2	Select geomagnetic cut-off: <ul style="list-style-type: none"> • 0 - no geomagnetic cut-off. • 1 – geomagnetic cut-off is requested. • 2 – geomagnetic cut-off in what(2)
	What(2)	1.75	Vertical geomagnetic cut-off at central latitude (GV) for What(1)= 2, no entry otherwise
	What(3)		Number of energy points in the spectra (default 50)
	What(4)		For testing (> 0 vertical run)
	What(5)		Unused
	What(6)		Unused
	SDUM	&	'&' this card is a continuation card

Once defined the GCR by SPECSOUR, the user initialises the local cosmic-ray source using the GCR-SPE cards. In this case, we invoke a GCR source at a minimum solar wind yielding a maximum intensity of the cosmic rays. Figure 3.4 reports the corresponding input card in FLAIR.

```

100 atm shells, dipole field, read spectra from zzphi0465.spc
GCR-SPE                               Type: Spectra
Field: naive dipole ▼ Shells: 101      Radius:
Equatorial Field:      Dump shell: 0    Unit: 0                               DateFile: phi0465

```

Figure 3.4 – Initialisation of the GCR source as constituted by ions emitted at an injection point above Houston.

The routine starts sampling one GCR ion, first sampling its nucleus (selecting A and Z), their kinetic energy from its energy spectrum (modulated at the chosen Solar activity), and finally, their spatial positions. Then, the information was passed to the tracking routine that began its transport within the Earth's geomagnetic field represented in the dipole approximation.

Transport options

As stated in the previous paragraph, the geomagnetic field is simulated as a dipole and, in such a first-order approximation, is tilted to the Earth's rotation axis by ~ 11.5 degrees.

The geomagnetic field shielding capabilities are more effective in the function of the field orientation than the intensity. Consequently, the magnetic polar regions with greater field intensity are more poorly shielded than the equatorial.

FLUKA modulated the GCR primary spectrum imposing a vertical threshold on the ions' magnetic rigidity (see Equation 1.4), also called geomagnetic cut-off. The vertical geomagnetic cut-off used in the present simulation has been calculated at each location using the online calculator [40].

The GCR ion, whose energy is above the geomagnetic vertical cut-off, penetrates the atmosphere and interacts with its nuclei (O, N, C and Ar in the actual model), generating an elaborate shower of particles (up to 180-190 secondaries for each primary particle history – see Figure 3.5) whose energy interval ranges from TeV to keV.

For this reason, we use the code version in which the relativistic interactions can be simulated using the Dual Parton Model [41], the relativistic Quantum Molecular Dynamics [42], Boltzmann Master Equation [21], and including the effect of the geomagnetic fields up to sea level.

Due to the large scale of the model and the complex nuclear reaction sequence, the simulation needs a long computational time to obtain a meaningful estimator convergence.

Our typical simulation uses 96 CPUs in “embarrassing parallelism modality” (see [31] and Chapter 2), each running a sample population of 100000 particles (a total of $9.6e6$ primaries) following 1.7 billion secondary particles. The typical running time is between 4-7 hours.

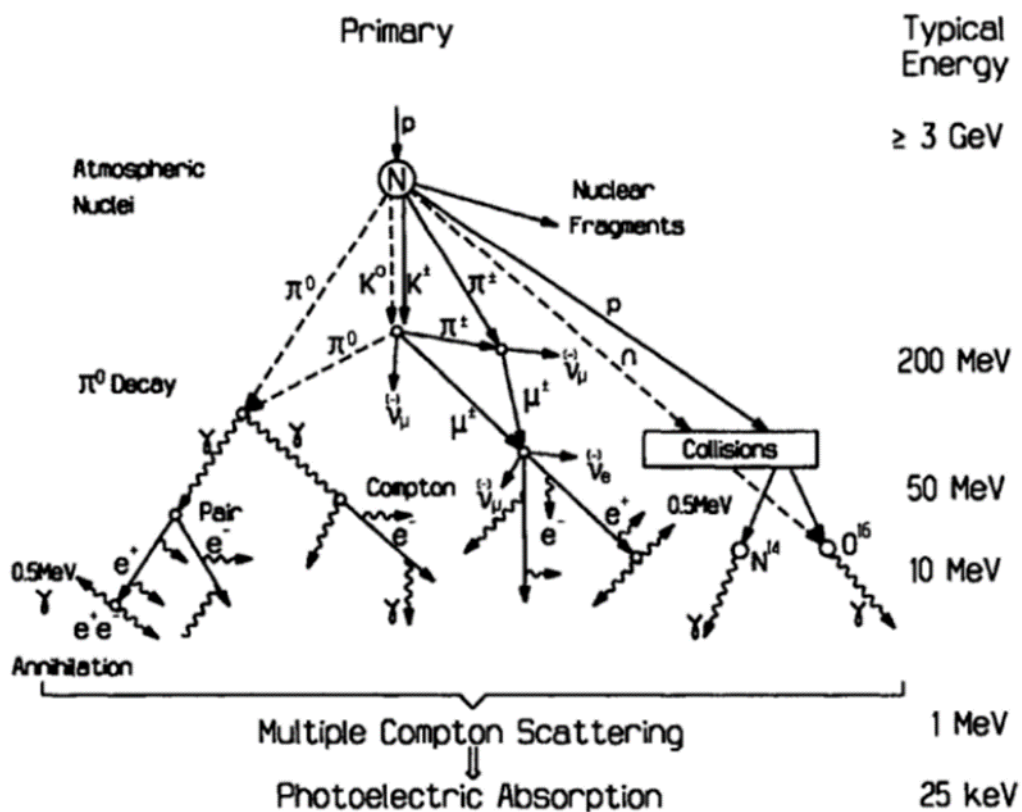


Figure 3.5: CGR ion's secondary particle shower in the Earth's atmosphere.

We reduced the computational by excluding the gamma photons transport and applying a biasing scheme for all unstable particles produced in the shower.

In this scheme, all the unstable particles whose decay length is below a minimum are promoted to user-defined mean decay length. At the biased decay length, the code randomly decides whether the particle will survive after creating the decay products or not (Russian Roulette). In the case of survival, the statistical weight of the decay products is adjusted to balance the weight bias. In this way, tracks of unstable particles generate many decay events whose scores are re-normalised at their unbiased original probability (see Chapter 2, paragraph on Biasing techniques and [43] for details).

Simulations set

In the present simulation set, we use the FLUKA atmospheric model to estimate the radiation field induced by CGR at the location of three neutron measurement stations: two at sea level (Houston-HOU and New York City - NYC) and one at 1950 m of altitude (Mount Wilson – MW). Table 3.2 reports the geographic coordinates and the local vertical cut-off.

Each FLUKA simulation estimates the complete distributions of the primary and secondary particles generated in the GCR shower.

Table 3.4: The three locations selected for the neutron flux estimations

Location	Altitude [km from sea level]	Geographic Coordinate	Magnetic Cut Off [GV]
NYC	0.000	40N 74W	2.47
HOU	0.000	30N 95W	4.56
MW	1.950	44N 74W	1.85

Table 3.5 resumes the data collected at various altitudes above each of the considered location fluxes and their angular dependence at separation surfaces at various altitudes. Table 5 resumes the estimator used in the present Calculation.

Table 3.5: List of estimators, binnings and scoring altitudes

Estimator Type	Particles	Energy Binning	Angular binning	Altitude
USRDBX Flux on a surface	BEAMPART	0.3-30000 GeV (20 log-Bins)	40	0 km, 2 km, 10 km, 70 km
	Proton			
	Neutron			
	Muon+			
	Muon-			
	Pion-			
	Pion+			
Helium-4				
USRTRACK Flux averaged on a volume	Hadron flux greater than 10 MeV (Scales as SEU)	0.01 - 30000 GeV (40 bins)	---	

Here, we limit comparing the simulation outcomes with experimental data to the neutron fluxes. In contrast, we discuss the other secondary particles' simulated data in inner congruency checks.

As reported in Table 5, we consider the estimation of some more exotic particles as muons (μ^+ and μ^-) and pions (π^+ and π^-) that are of interest for material radiation damage.

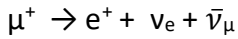
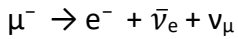
Pions are secondary particles that belong to the GCR shower in the atmosphere, and muons are their decay product (half-life 26 ns). The name pion is used for any of the three elementary particles: π^+ , which is charged positively; its anti-particle π^- ; and the neutral form π^0 . Because of the absence of charge and their short half-life (8.4×10^{-17} s), π^0 are challenging to detect. The π consists of a quark and an anti-quark and therefore are the lightest mesons. The charged pions have a mass of $139.6 \text{ MeV}/c^2$, and their decay scheme is based on two branches

$$1) \quad \begin{aligned} \pi^+ &\rightarrow \mu^+ + \nu_\mu && \text{Decay in a muon and a muon neutrino (Branching ratio 0.9998)} \\ \pi^- &\rightarrow \mu^- + \bar{\nu}_\mu \end{aligned}$$

$$2) \quad \begin{aligned} \pi^+ &\rightarrow e^+ + \nu_e && \text{Decay in an electron and an electron anti-neutrino (Branching ratio 0.0001)} \\ \pi^- &\rightarrow e^- + \bar{\nu}_e \end{aligned}$$

thus, the muons present in the atmospheric GCR shower belong to the decay of pions. μ^- are similar to electrons but with greater mass and should not have any sub-structure. The half-life is

relatively long (2.2 μs) compared with other subatomic particles. It has an anti-particle denoted by the μ^+ symbol. The decays scheme is



Because of their greater mass and minor bremsstrahlung compared with electrons of the same energy, Muons penetrate deeper into the matter. That is why muons generated at great altitudes reach the ground and penetrate deep mines.

FLUKA's estimates of some selected particles in the GCR atmospheric shower

The following compares the simulated energy differential flux for some primary GCR ions and secondary shower products (neutrons, pions and muons) at 0 km, 1.9 km, 10 km and 70 km of altitude.

Table 3.6: uncollided (BEAMPART generalised particles- see FLUKA manual [43]) GCR ion flux for the three considered locations at various altitudes estimated by FLUKA

Altitude	0 km		1.9 km		10 km		70 km	
Location	Ion flux [cm ⁻² s ⁻¹]	% of Relative Error	Ion flux [cm ⁻² s ⁻¹]	% of Relative Error	Ion flux [cm ⁻² s ⁻¹]	% of Relative Error	Ion flux [cm ⁻² s ⁻¹]	% of Relative Error
Houston (4.56 GV)	6.50e-12	99%	2.96e-6	13.0%	3.80e-3	0.46%	0.50	0.15%
New York (2.47 GV)	6.73e-7	49.9%	4.28e-6	19.2%	7.58e-3	0.45%	1.02	0.16%
Mount Washington (1.85 GV)	0.0	0.0	4.45e-6	24.6%	9.69e-3	0.55%	1.36	0.15%

Table 3.6 compares the uncollided primary particle fluxes and the relative error associated with the inner MC convergence. The table also shows the vertical cut-off of each location (first column of Table 3.6).

As the CGR ions penetrate deeper into the atmosphere, travelling in air layers of increasing density, the interaction probability also increases, causing a progressive extinction of the primary particles. This trend fully justifies the significant increases in the relative error at lower altitudes.

As expected, the ion flux intensity increases with the vertical cut-off decrease. For example, at 70 km of altitude, moving from Houston to Mount Washington, we observe progressive flux increases of factor 2. and 2.7, respectively, for a decrease of the geomagnetic cut-off of 0.54 and 0.41. The trend is similar also for the other altitude.

The zero scores for the flux at 0 km of altitude at Mount Washington (the location with the lowest vertical cut-off) find its explanation in a mixed effect of geomagnetic modulation of the GCR spectra and poor statistical sampling. Comparing the energy spectra reported in the series of Figures 3.13a-3.15a, we can see that the flux increase at Mount Wilson is due to the growth of the low-energy particle population admitted into the atmosphere by the lower vertical cut-off.

Conversely, the high-energy tails of the spectra remain at almost similar intensities. Consequently, in the Mount Wilson simulation, the high-energy particles having a higher probability of penetrating the atmosphere are less sampled than the low-energy particles causing an absence of score at the altitude of 0 km. In principle, a meaningful score at 0 km of altitude for Mount Wilson can be obtained, increasing the sample of primary particles in the simulation. However, the simulation of the deep penetration of uncollided GCR ions into the Earth's atmosphere goes beyond the scope of the present thesis and, in any case, could become a very intensive calculation task that could be motivated only by a strong interest in the estimations of this data.

Table 3.7: Proton flux for the three considered locations at various altitudes estimated by FLUKA

Altitude	0 km		1.9 km		10 km		70 km	
Location	flux [cm ⁻² s ⁻¹]	% of Relative Error	flux [cm ⁻² s ⁻¹]	% of Relative Error	flux [cm ⁻² s ⁻¹]	% of Relative Error	flux [cm ⁻² s ⁻¹]	% of Relative Error
Houston (4.56 GV)	5.56e-4	1.34%	3.01e-3	0.63%	0.15	0.32%	0.51	0.16%
New York (2.47 GV)	6.11e-4	2.04%	3.41e-3	0.91%	0.21	0.16%	1.02	0.17%
Mount Washington (1.85 GV)	6.15e-4	2.42%	3.42e-3	1.26%	0.23	0.18%	1.36	0.17%

Table 3.7 compares the proton flux intensities at the considered locations and altitudes. As already reported (Figures 6-7), protons are the dominant particles in the CGR population. However, despite the progressive attenuation of its primary flux, there are continuously re-created during the interaction of the secondary particles with the atmosphere. Consequently, the attenuation of the proton flux is less severe (3 orders of magnitude) than the one of the uncollided GCR ions flux (from 8 to 12 orders of magnitude).

The fluxes intensities scale correctly with the vertical cut-off, and the relative error ranges from 0.5 to 2.5%, ensuring the statistical congruency of MC results. A hypothesis that explains the proton spectral pattern (see Figures 13b, 14b and 15b) is characterised by a broad maximum in the energy range from 100 keV to 0.1 GeV followed by a fast decreasing high energy tail (up to 10 TeV), is that the substitution of the primary protons with secondary proton sustain the intensity in the first energy range. Conversely, the latter energy range, which has a higher probability of containing protons of cosmic origin, attenuated more during the penetration into the atmosphere.

Table 3.8: Neutron flux for the three considered locations at various altitudes estimated by FLUKA

Altitude	0 km		1.9 km		10 km		70 km	
Location	flux [cm ⁻² s ⁻¹]	% of Relative Error	flux [cm ⁻² s ⁻¹]	% of Relative Error	flux [cm ⁻² s ⁻¹]	% of Relative Error	flux [cm ⁻² s ⁻¹]	% of Relative Error
Houston (4.56 GV)	2.18e-2	0.63%	0.12	0.27%	2.67	0.1%	0.75	0.10%
New York (2.47 GV)	2.57e-2	0.94%	0.14	0.42%	3.85	0.12%	1.27	0.13%
Mount Washington (1.85 GV)	2.61e-2	1.14%	0.15	0.56%	4.25	0.14%	1.52	0.12%

The results reported in Table 8 concern secondary neutrons generated within the atmospheric showers at various depths that travel in all directions from their origin. The maximum neutron flux intensity is at 10 km of altitude for all the considered locations.

To explain this result, we must consider neutrons directed toward higher altitude travel in a less dense medium, experimenting with progressively less extinction. Conversely, travelling along the opposite path toward the heart surfaces they have a higher capture probability.

Furthermore, the secondary particles that could generate neutrons increase the probability of undergoing such reaction channels in the densest atmospheric layers located at low altitudes.

The combination of this effect maximises the flux of secondary neutrons at altitudes between 10 to 70 km. The neutron flux intensities scaling according to the local magnetic cut-off, inherited by their parent, is another confirmation of their production as secondary particles in the FLUKA model.

Table 3.9: Alpha (^4He) flux for the three considered locations at various altitudes estimated by FLUKA

Altitude	0 km		1.9 km		10 km		70 km	
Location (Mag. cut-off)	flux [$\text{cm}^{-2} \text{s}^{-1}$]	% of Relative Error	flux [$\text{cm}^{-2} \text{s}^{-1}$]	% of Relative Error	flux [$\text{cm}^{-2} \text{s}^{-1}$]	% of Relative Error	flux [$\text{cm}^{-2} \text{s}^{-1}$]	% of Relative Error
Houston (4.56 GV)	3.89e-7	34.8%	3.03e-6	20.6%	9.37e-5	4.41%	6.35e-2	0.41%
New York (2.47 GV)	6.30e-7	57.7%	4.64e-6	28.02%	1.32e-4	5.47%	0.12	0.35%
Mount Washington (1.85 GV)	4.78e-7	95.2%	8.51e-7	47.7%	1.35e-4	6.86%	0.146	0.29%

Alpha particles (^4He) are included in the primary emission of the GCR ions and, as reported in Table 3.9, show their maximum emission at 70 km altitudes for all locations (see also Figures 13d, 14d, and 15d). The flux intensities agree with the vertical cut-off modulation.

Table 3.10: π^+ flux for the three considered locations at various altitudes estimated by FLUKA

Altitude	0 km		1.9 km		10 km		70 km	
Location (Mag. cut-off)	flux [$\text{cm}^{-2} \text{s}^{-1}$]	% of Relative Error	flux [$\text{cm}^{-2} \text{s}^{-1}$]	% of Relative Error	flux [$\text{cm}^{-2} \text{s}^{-1}$]	% of Relative Error	flux [$\text{cm}^{-2} \text{s}^{-1}$]	% of Relative Error
Houston (4.56 GV)	4.86e-6	13.0%	1.78e-5	4.43%	8.60e-4	0.85%	2.99e-6	18.0%
New York (2.47 GV)	3.31e-6	13.2%	1.92e-5	7.32%	9.44e-4	1.53%	8.20e-6	27.7%
Mount Washington (1.85 GV)	4.43e-6	16.4%	1.70e-5	7.51%	9.57e-4	1.98%	1.04e-5	57.5%

Table 3.11: π^- flux for the three considered locations at various altitudes estimated by FLUKA

Altitude	0 km		1.9 km		10 km		70 km	
Location (Mag. cut-off)	flux [$\text{cm}^{-2} \text{s}^{-1}$]	% of Relative Error	flux [$\text{cm}^{-2} \text{s}^{-1}$]	% of Relative Error	flux [$\text{cm}^{-2} \text{s}^{-1}$]	% of Relative Error	flux [$\text{cm}^{-2} \text{s}^{-1}$]	% of Relative Error
Houston (4.56 GV)	4.06e-6	7.47%	2.26e-5	4.35%	8.32e-4	0.83%	2.84e-6	22.3%
New York (2.47 GV)	3.64e-6	12.7%	2.49e-5	6.84%	9.37e-4	2.02%	7.59e-6	36.7%
Mount Washington (1.85 GV)	6.90e-6	22.9%	2.55e-5	8.59%	9.21e-4	2.14%	1.88e-6	51.3%

Tables 3.10-3.11 report the total flux intensities for π^- and π^+ at the considered locations, whereas Figures 3.13 to 3.15 (g and h) report the energy spectra. Pions, like neutrons, are pure secondary particles belonging to the GCR atmospheric interactions. Thus, in analogy with neutrons, the maximum pion fluxes are at 10 km of altitude.

Table 3.12: μ^+ flux for the three considered locations at various altitudes estimated by FLUKA

Altitude	0 km		1.9 km		10 km		70 km	
Location (Mag. cut-off)	flux [$\text{cm}^{-2} \text{s}^{-1}$]	% of Relative Error	flux [$\text{cm}^{-2} \text{s}^{-1}$]	% of Relative Error	flux [$\text{cm}^{-2} \text{s}^{-1}$]	% of Relative Error	flux [$\text{cm}^{-2} \text{s}^{-1}$]	% of Relative Error
Houston (4.56 GV)	1.05e-2	0.18%	1.55e-2	0.16%	7.62e-2	0.13%	1.83e-4	7.32%
New York (2.47 GV)	1.05e-2	0.26%	1.56e-2	0.24%	8.38e-2	0.72%	2.22e-4	7.04%
Mount Washington (1.85 GV)	1.05e-2	0.57%	1.55e-2	0.28%	8.36e-2	0.23%	1.72e-4	7.30%

Table 3.13: μ^- flux for the three considered locations at various altitudes estimated by FLUKA

Altitude	0 km		1.9 km		10 km		70 km	
Location (Mag. cut-off)	flux [$\text{cm}^{-2} \text{s}^{-1}$]	% of Relative Error	flux [$\text{cm}^{-2} \text{s}^{-1}$]	% of Relative Error	flux [$\text{cm}^{-2} \text{s}^{-1}$]	% of Relative Error	flux [$\text{cm}^{-2} \text{s}^{-1}$]	% of Relative Error
Houston (4.56 GV)	8.67e-3	0.18%	1.30e-2	0.18%	6.73e-2	0.13%	1.24e-4	6.02%
New York (2.47 GV)	8.65e-3	0.30%	1.30e-2	0.28%	7.27e-2	0.23%	1.81e-4	11.6%
Mount Washington (1.85 GV)	8.67e-3	0.38%	1.31e-2	0.30%	7.30e-2	0.28%	1.27e-4	9.45%

Muons belong to the decays of Pions, and their flux intensities have the same pattern as the secondary particles (see Tables 3.12-3.13, Figures 3.13 to 3.15, e-f). A possible explanation for the absence of vertical cut-off modulation could be mainly imputed to the fact that, as tertiary particles within showers, they lost memory of such modulation.

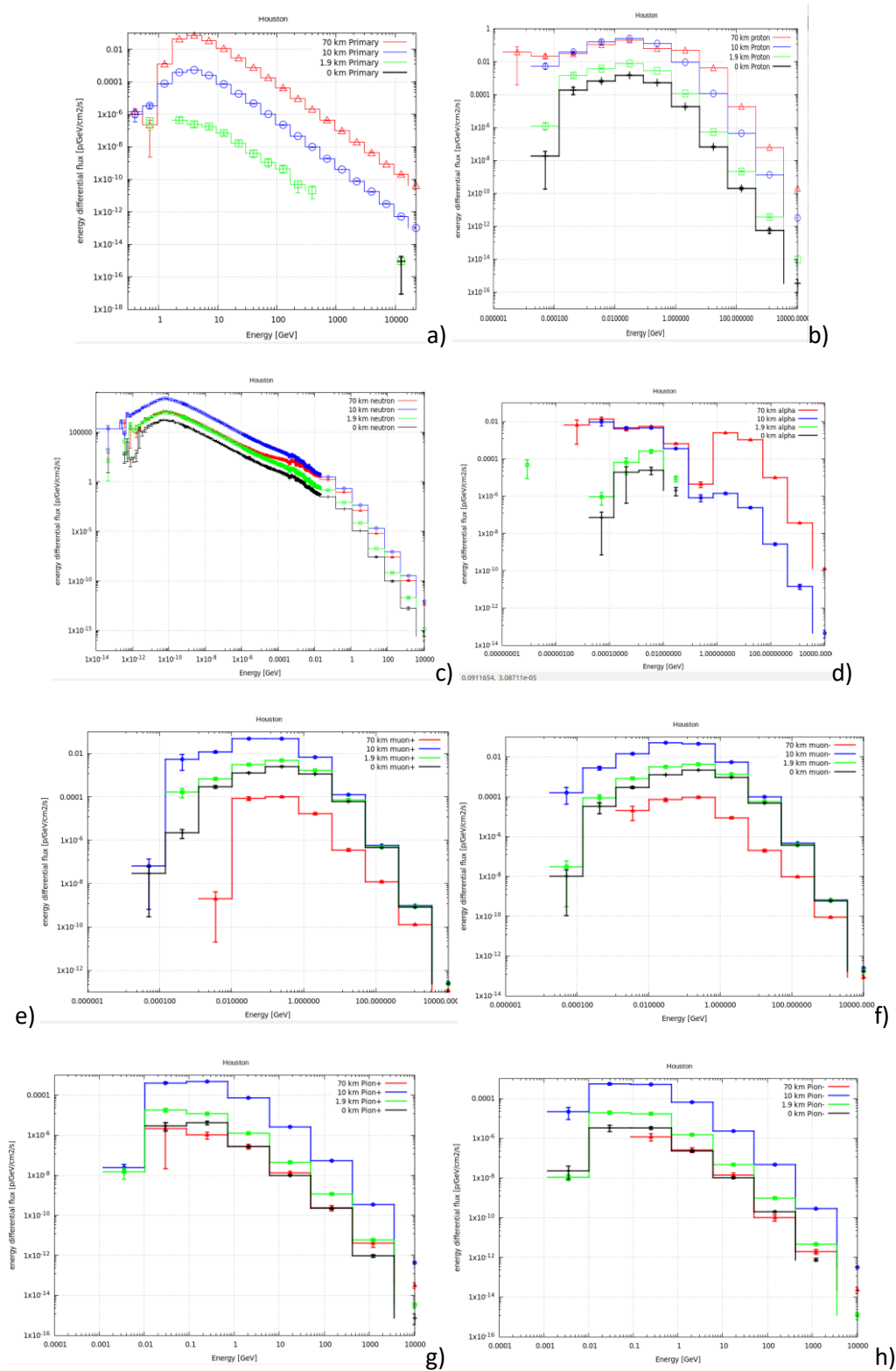


Figure 3.13 - Estimates of the energy distribution of particle fluxes at 70 km, 10 km, 1.9 km, 0 km above Houston: a) Primary GCR ions; b) Protons; c) neutrons; d) alpha; e) Muon+ ; f) Muons-; g) Pion+; h) Pion-.

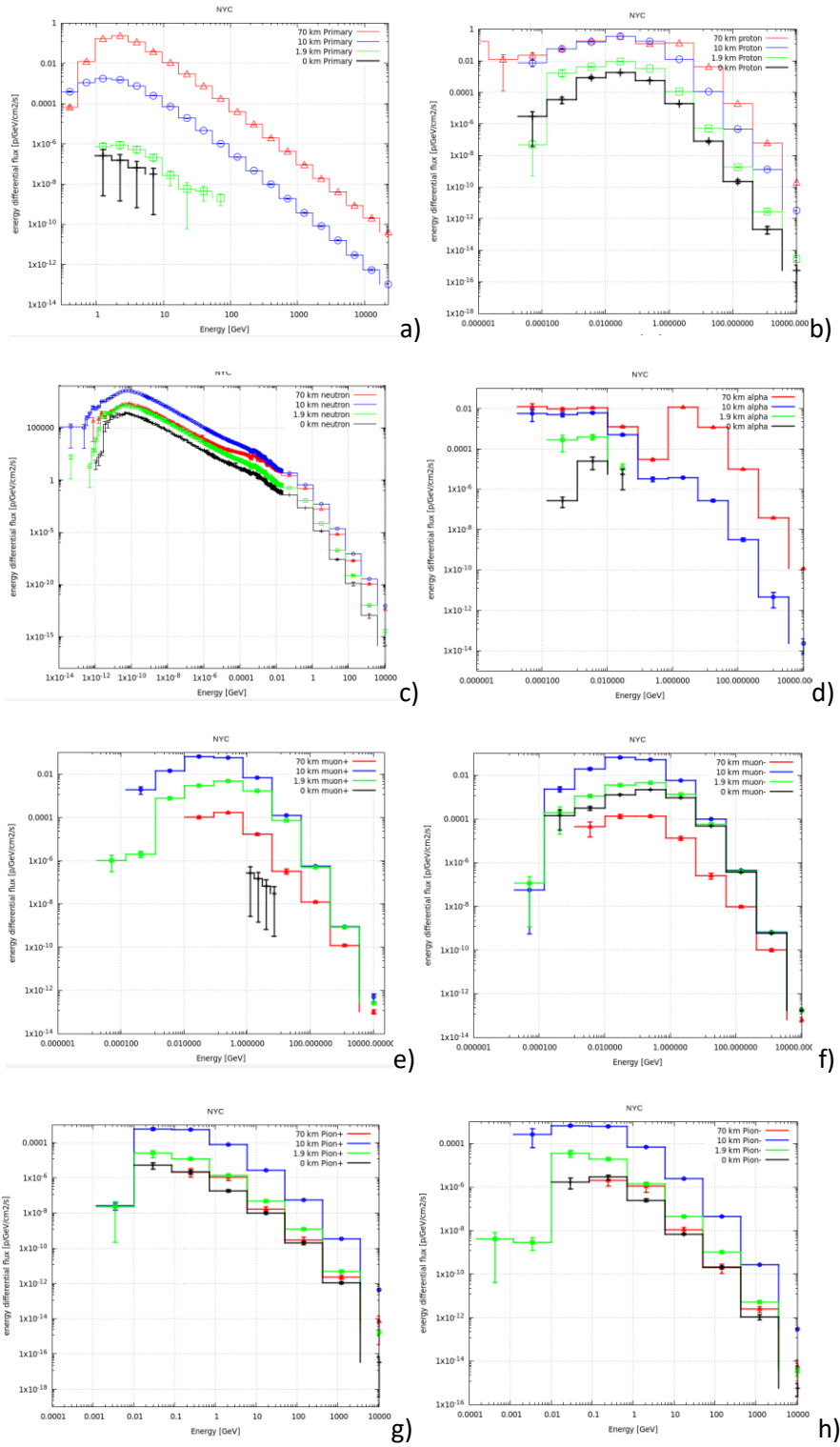


Figure 3.14 - Estimates of the energy distribution of particle fluxes at 70 km, 10 km, 1.9 km, 0 km above New York: a) Primary GCR ions; b) Protons; c) neutrons; d) alpha; e) Muon+ ; f) Muons-; g) Pion+; h) Pion-.

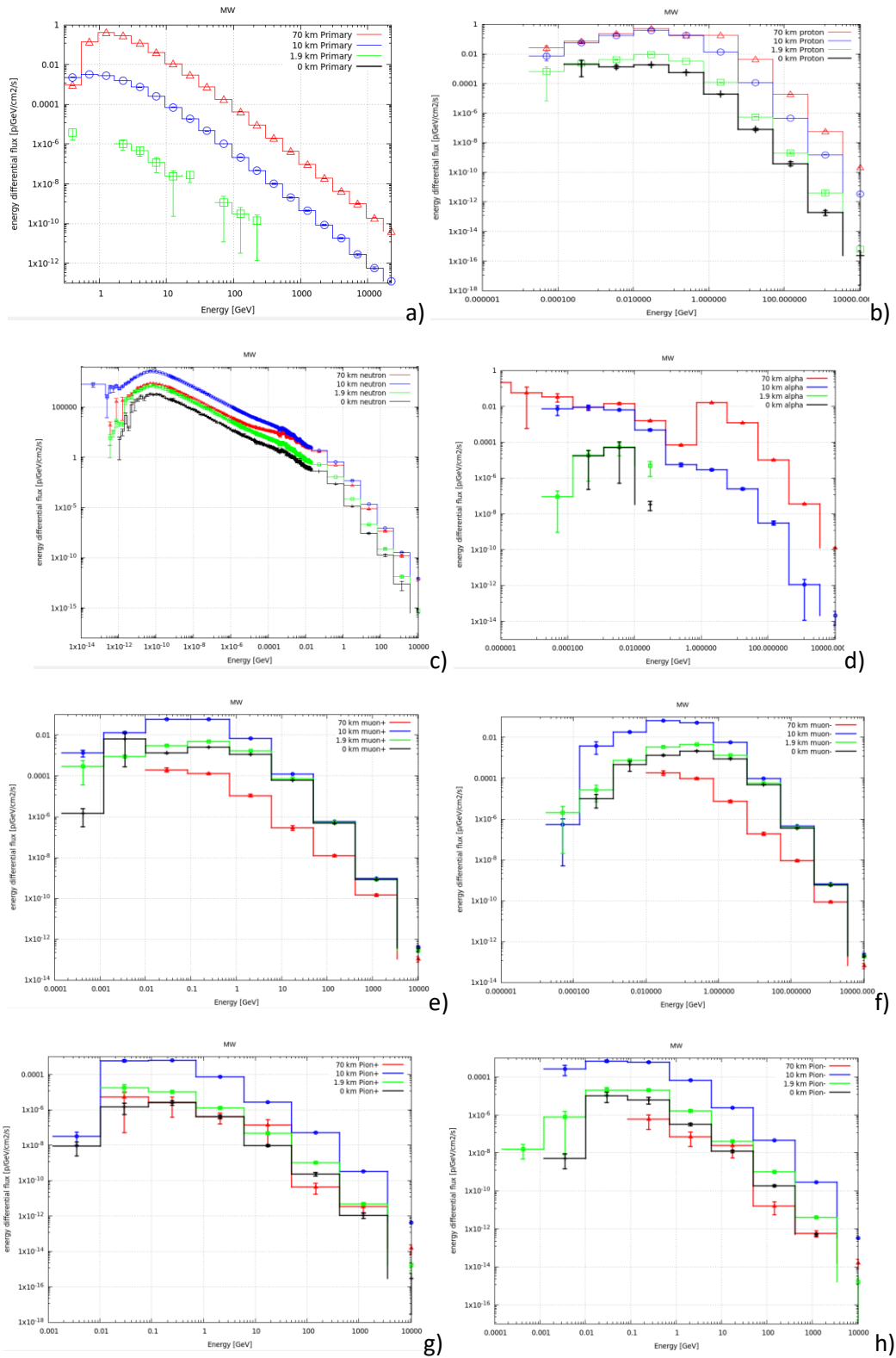


Figure 3.15 - Estimates of the energy distribution of particle fluxes at 70 km, 10 km, 1.9 km, 0 km above Mount Washington: a) Primary GCR ions; b) Protons; c) neutrons; d) alpha ; e) Muon+ ; f) Muon-; g) Pion+; h) Pion-

Single Events Upset estimation

Table 3.12 reports the estimates of the cumulative hadron flux with energy above 20 MeV. FLUKA allows the users to estimate cumulative hadron flux (generalised particle HADGT20M) in user-selected energy binning using a track-length estimator.

Table 3.12: Hadron flux greater than 20 MeV (proportional to Single Event Upset)

Altitude	0 km		1.9 km		10 km		70 km	
Location	HADGT20M	% of Relative Error	HADGT20M	% of Relative Error	HADGT20M	% of Relative Error	HADGT20M	% of Relative Error
Houston (4.56 GV)	0.0077	0.40%	0.034	0.23%	0.776	0.08%	0.913	0.08%
New York (2.47 GV)	0.0088	0.61%	0.042	0.29%	1.099	0.09%	1.713	0.11%
Mount Washington (1.85 GV)	0.0092	0.73%	0.043	0.35%	1.206	0.12%	2.186	0.10%

This estimator is handy because the hadron fluxes above 20 MeV are proportional to the amount of Single Event Upset in the electronic device during irradiation with hadrons. Therefore, knowing the SEU cross-section for a given electronic device [44], we can calculate the probability of SEU for a given irradiation field.

For example, we compare the HADGT20M total flux irradiation of the same material at 70 km at Houston, New York and Mount Wilson. According to the geomagnetic modulation, the SEU probability concerning Houston increases by a factor of 1.87 in New York and 2.39 at Mount Washington.

Neutron Flux Comparison between FLUKA and BSY model

This paragraph compares the FLUKA estimates of the neutron fluxes obtained for the Houston, New York and Mount Washington locations with the correspondent experimental outcomes elaborated through the Below, Struminsky, and Yanke (BSY) semi-empirical model.

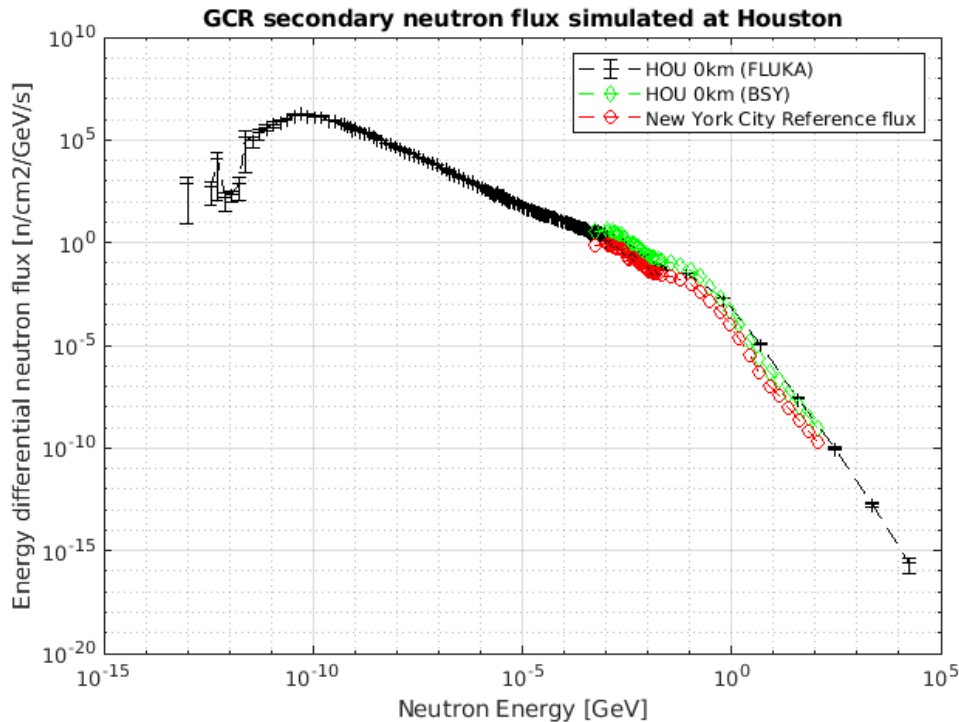
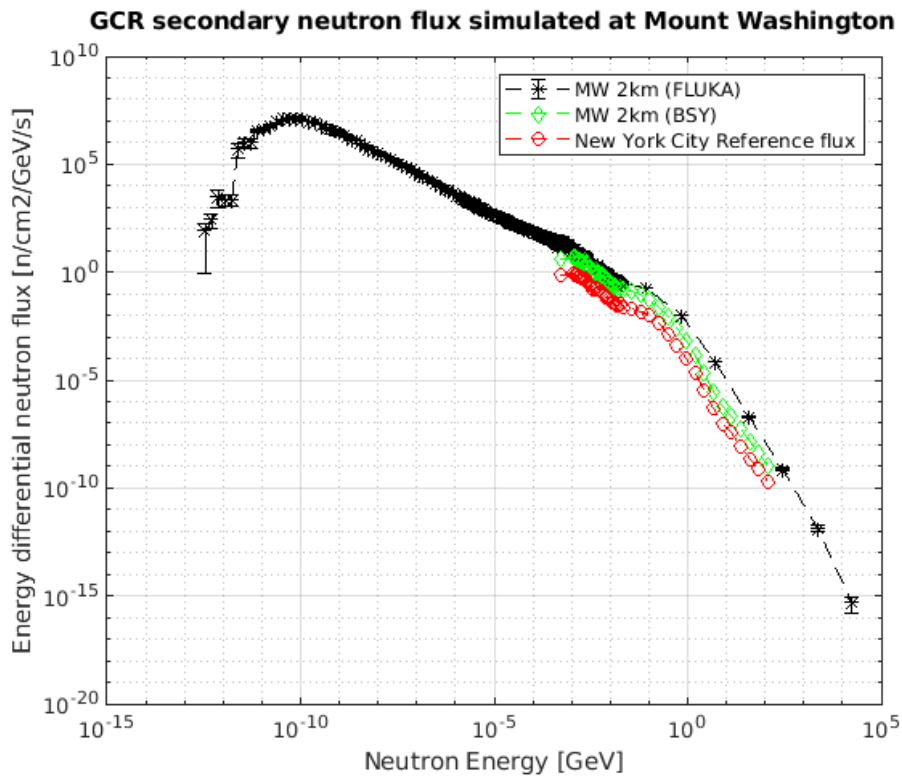


Figure 3.16 - Comparison of neutron energy distribution flux from GCR shower at HOUSTON measurement station: FLUKA estimate (Black), Calculation with the BSY model (Green), and the experimental reference flux of New York measurement station (Red).

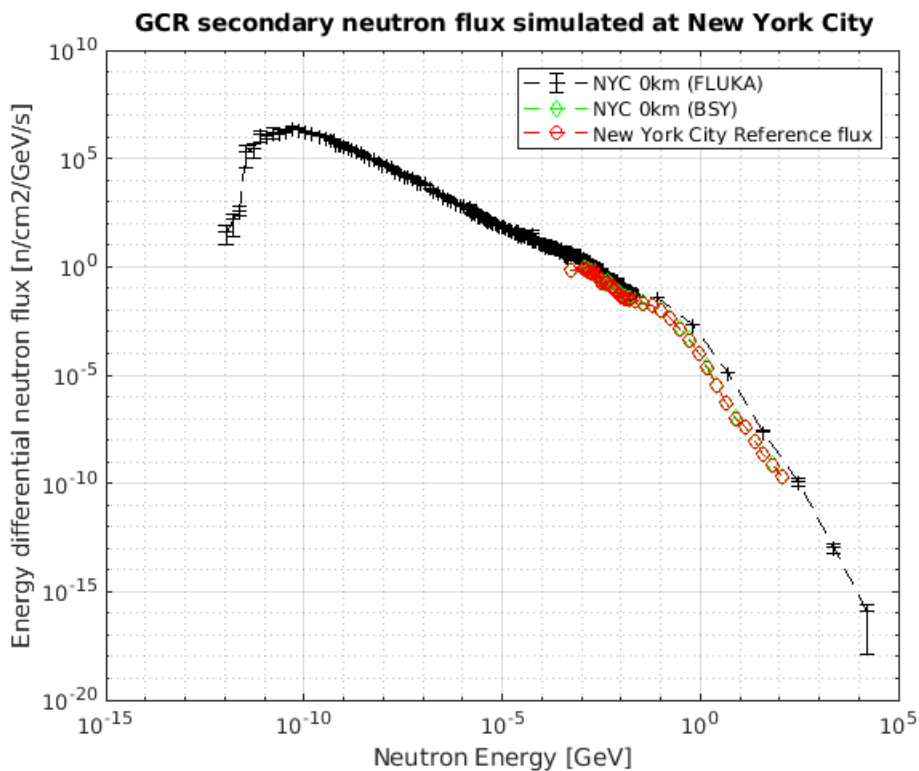
Figure 3-16 compares Houston's neutron flux (green curve) obtained with the BSY model and the FLUKA simulation (black curve). The experimental reference flux of New York used in the BSY model (red curve) to rescale the data at the local geomagnetic cut-off is also reported.

Due to their experimental nature, BSY and reference fluxes cover a narrower energy interval (5e-4 - 118 GeV) than the FLUKA estimate (1e-13 – 16.9 TeV). Despite such limitations, the agreement between the green and the black curve is satisfactory.

However, in the low energy range (5e-14 – 0.6 GeV), FLUKA underestimates the experiments, whereas, in the high energy range (0.6 – 118 GeV), FLUKA overestimates it. Such deviations should derive from the reconstruction process with the answer function of the Bonner sphere set used for the Houston measurements that need to filter away the contributions of down scattered neutrons from a higher energy. This hypothesis is reinforced by the systematic lower intensity of Houston's data at higher energy, probably due to the down scattering of a fraction of such neutrons within the Bonner Sphere apparatus. Another contribution to the FLUKA overestimation could be imputed at the progressive detection efficiency loss with the neutron's kinetic energy.



a)

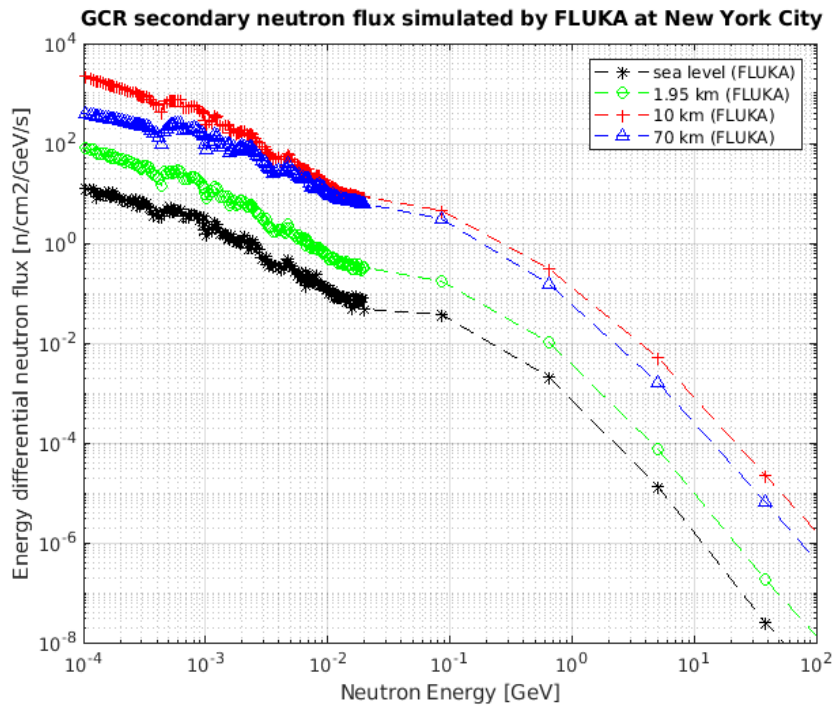


b)

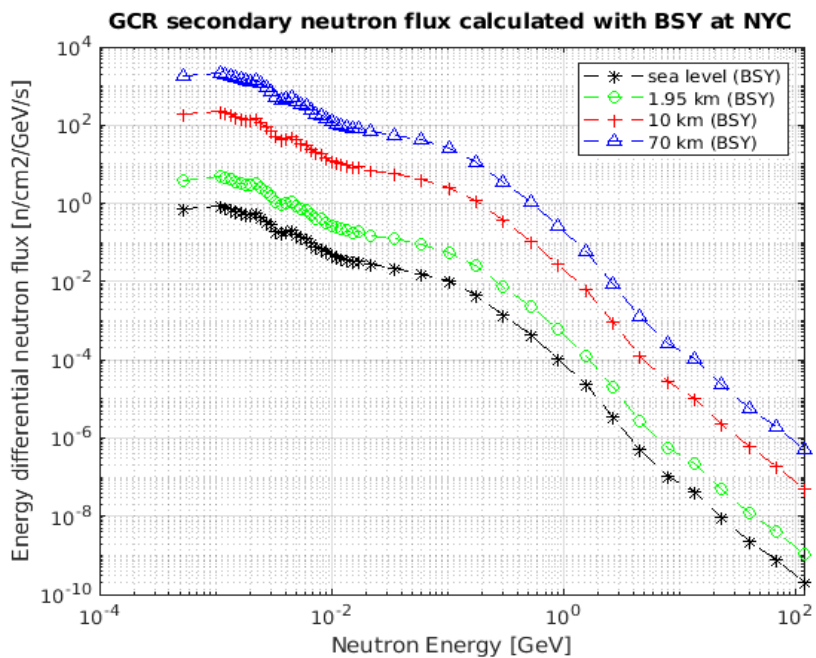
Figure 3.17 - a) Comparison of FLUKA estimates and experimental data for the neutron spectrum at Mount Washington; b) the same comparison for New York City measurement stations.

Figures 3.17a compare Mount Washington data with the same FLUKA estimations and show the same trends as those obtained for Houston. Figure 3.17b shows the same comparison with the New York station.

In both comparisons, the flux overestimation in the high-energy region is slightly more significant than in the case of Houston. However, the neutron spectra flux are in good agreement, and the difference in intensity should be reduced by refining the FLUKA with the inclusion of the ground albedo effect, the modelling of the detector answer function, the fine-tuning of the geomagnetic cut-off, and a solar modulation closer to the experimental one.



a)



b)

Figure 3.18 - Comparison of neutron energy distribution flux from GCR shower at New York measurement station: a) FLUKA estimate b) Calculated with the BSY model.

Finally, Figure 3.18 shows the neutron spectra of the New York station at the altitudes of 0, 1.9, 10 and 70 km as obtained from the FLUKA simulations (Figure 3.18a) and the same spectra from the BSY model (Figure 3.18b). In the case of the BSY model, the neutron flux intensity is proportional to the altitude and reaches its maximum at 70 km of altitude. Conversely, in the FLUKA simulation, the maximum neutron flux intensity is at 10 km and progressively decreases for further altitude increases. The FLUKA behaviour is compatible with a neutron source delocalised across the whole atmosphere, as in the case of secondary particles generated from a GCR primary during an atmospheric shower. The BSY responses are compatible with a neutron source located outside the atmosphere with the neutron progressive neutron penetration in the atmospheric layer, and their consequent intensity decrease.

Conclusions

We look for simulation tools capable of evaluating the GCR radiation field and its transformation during the interaction with Solar activities, the Earth's geomagnetic field and the atmosphere.

Based on a careful examination of the MCNP license agreement, we discover that the code release to foreign institutions is not allowed for aerospace applications.

However, FLUKA is best fitted for high-energy simulations and coupling with magnetic fields. Its standard package has a built-in model for the simulations of CGR and SE sources, including a model of the Earth's atmosphere. According to this fact, choosing FLUKA for this first round of preliminary activities is mandatory.

The main objectives of the activities are to learn how to use the GCR tools of FLUKA, acquire the skill to critically review some simulation results and compare them with experimental outcomes.

For this scope, we selected the measurement of the atmospheric neutron spectra carried out in three experimental stations in the USA (Mount Wilson, Houston, and New York).

The FLUKA simulation of each experimental station requests the selection of the local properties of the geomagnetic field, its interaction with the incoming GCR particles, and the progressive penetration of all the particles in the atmospheric layers up to the estimation zones.

Finally, the model definition offers the possibility to increase our knowledge of the general problem and a deep understating of the actual limit of the model.

The resulting simulated spectra are in relatively good agreement with the measurements. However, modelling the detector answer function in FLUKA should probably decrease the discrepancy.

During the simulation, we collected results regarding the secondary particles that belong to the high-energy channels of the interaction of the GCR ions with the matter. In many cases, the range of inspecting energy is entirely above the limit of the rQMD. Therefore, it needs the DPM event generator fully implemented in FLUKA.

Chapter 4 - The ground irradiation facilities

Introduction

The new generation of electronic components is faster, cheaper, and more versatile than the traditional “radiation hardening components” used in aerospace [45]. However, their reduced dimensions are more prone to radiation-induced faults and need dedicated qualification tests.

Based on what was discussed in the previous chapters, it is clear that the mixed and dynamic radiation fields encountered in spatial missions are not fully reproducible in the traditional nuclear irradiation facilities (accelerators, research nuclear reactors, radioisotope sources) and dedicated new facilities are under design [46].

In the meantime, to overcome the lack of representativity of the actual irradiation facilities, testing components and systems is often a matter of cross-checking between results obtained from the different types of irradiation facilities [47].

There are tests carried out to establish the merchandise category of a component, calibrate a system, collect failure data for availability assessment, explore the possibility of using a new component instead of an old one, and develop sensors for research and exploration.

Apart from the problems connected to the representativity of a test relative to a given mission, there are also accessibility problems connected with safety and radioprotective concerns. For example, tests carried out with neutrons on research nuclear reactors that request one of the most strict irradiation protocols among the irradiation facilities need a dedicated feasibility study where all the concerns regarding the safety of the reactor operations, the samples' integrity and their post-irradiation status, as well as the specific radioprotection measures, must be investigated and correctly solved. Furthermore, at the end of the irradiation, the sample is often activated and needs a cooling period before it can be manipulated (this is also valid for some accelerator irradiation tests) in a laboratory for further tests.

Thus, selecting the irradiation facilities for a set of meaningful irradiation tests on systems and components for a given mission scenario is based on their representativity, accessibility, safety, and economic viability.

However, a first performance comparison between facilities based on general metrics can be made by modelling the interaction of their source particles in reference material and estimating some standard quantities. For example, in the following, using a set of simple FLUKA simulations, we estimated the levels of damage in a Silicon slab irradiated with distinct sources of neutrons, protons, electrons, ^{56}Fe ions and mixed electrons and γ photons radiation field from the spontaneous β^- decay of ^{60}Co source.

The motivation for the use of pure Silicon is that its damaging radiative mechanism is well assessed, allowing the introduction of concepts like the Displacement Per Atom (DPA), 1 MeV Neutron Silicon Equivalent (1MEVNSiEQ) fluence that are very useful to compare the damage level produced by different kind of radiative sources. Furthermore, Silicon is extensively used in micro-

electronics, and the radiometric characteristics of semiconductors with alternative compositions (such as GaAs [48]) were assessed using similar procedures.

Finally, the ^{60}Co source is also used to simulate the calibration of a radFET [49-51], often used as an integral dose radiation monitor in aerospace. The quantities obtained in the radFET calibration procedure were compared to those obtained using the Van Allen Belt's whole radiation field.

The Si slab model definition

Generalities on solid irradiation

During their transport in solids, the nuclear particles interact with the atoms of the crystal network and, locally and globally, modify the lattice structure. Those crystalline network modifications are generically referred to as "damages". According to the particles' nature, elastic or inelastic interactions produce the recoiling of the atoms, also known as Primary Knock-on Atoms (PKA) [52], that start travelling across the crystal network until the crystalline field dissipates their recoil kinetic energy. The PKAs return to rest in positions that are misplaced from the one expected for a perfect crystalline network generating defects and accumulating residual energy into the crystalline network.

Sometimes, the particle's kinetic energy is sufficiently high to activate various nuclear reaction channels generating a daughters' particle shower that induces further defects in the material.

Displacement Per Atom

The unit frequently used for measuring radiation damage in materials is the Displacement Per Atom (DPA). Displacement damage can be produced by charged particles, neutrons, ions and high-energy photons. The DPA quantity is directly related to the total number of induced defects according to the relation

$$DPA = \frac{A}{\rho N_A} N_F \quad \text{Equation 4.1}$$

Where

A = Mass Number;

ρ = bulk density g/cm³;

N_A = Avogadro Number;

N_F = number of Frenkel pairs;

Starting from the Frenkel pair, we briefly review some concepts at the base of the induction of the defects in solids by radiation.

Frenkel pair

A Frenkel pair is a defect constituted by a vacancy aside from an interstitial atom in a crystalline compound [52], defining the Total number of defects as

$$N_F = \kappa \frac{\xi(T)T}{2 E_{th}} \quad \text{Equation 4.2}$$

κ = displacement efficiency (typical value 0.8);

T = kinetic energy of the PKA;

E_{th} = is the displacement damage threshold;

$\xi(T)$ = is the Lindhard partition function;

The factor $2E_{th}$ is due to the hard-sphere model, which assumes that the energy is equally shared between the two atoms on each collision. The threshold displacement energy E_{th} constitutes the minimum energy, averaged in all crystallographic directions, necessary to promote the creation of the defects. Its value is tens of eV depending on the material.

The displacement efficiency $\kappa = 0.8$ compensates for the deviations from the hard-sphere model due to the forward scattering in the displacement cascade. It can be considered independent of T only in the $T \leq 1-2$ keV range, and at higher energies, the development of collision cascades results in defect migration and recombination of Frenkel pairs due to overlapping of different branches of a cascade which translates into the decay of $\kappa(T)$. The efficiency in question only slightly depends on atomic number Z and the temperature.

The first model for the calculation of N_F was developed by Kinchin and Pease, assuming that the atom cascade is created by a sequence of two-body elastic collisions between atoms, that becoming ions acquire a certain amount of kinetic recoil energy. In such collisions, it is assumed that there is no energy transferred to the lattice. When the ion recoil energy is below an ion-specific cut-off energy E_c , the electronic stopping force is neglected, and only atomic collisions occur. Above the cut-off energy E_c , no additional displacement occurs. The hard-sphere model gives the energy transfer cross section. According to the above assumptions, the number of defects $v(T)$ are

$$\begin{aligned} v(T) &= 0; & \text{for } T & 0 < T \leq E_{th}; \\ v(T) &= 1; & \text{for } E_{th} & < T \leq 2E_{th}; \\ v(T) &= \frac{T}{2E_{th}}; & \text{for } 2E_{th} & < T \leq E_c; \\ v(T) &= \frac{E_c}{2E_{th}}; & \text{for } T & > E_c; \end{aligned}$$

The relation between the displaced atoms and the kinetic energy of the PKA is reported in Figure 4.1, where collision generating ions recoil below E_{th} do not yield any defect. When the ion recoils with kinetic energy $E_{th} < T \leq 2E_{th}$ just one defect per hit is generated. Conversely, when the kinetic energy is in the range $2E_{th} < T \leq E_c$ the number of defects grows up linearly with T. Above E_c , where nuclear collisions dominate, the ions produce a constant number of defects independently from the ion kinetic energy, and the curve reaches a new plateau.

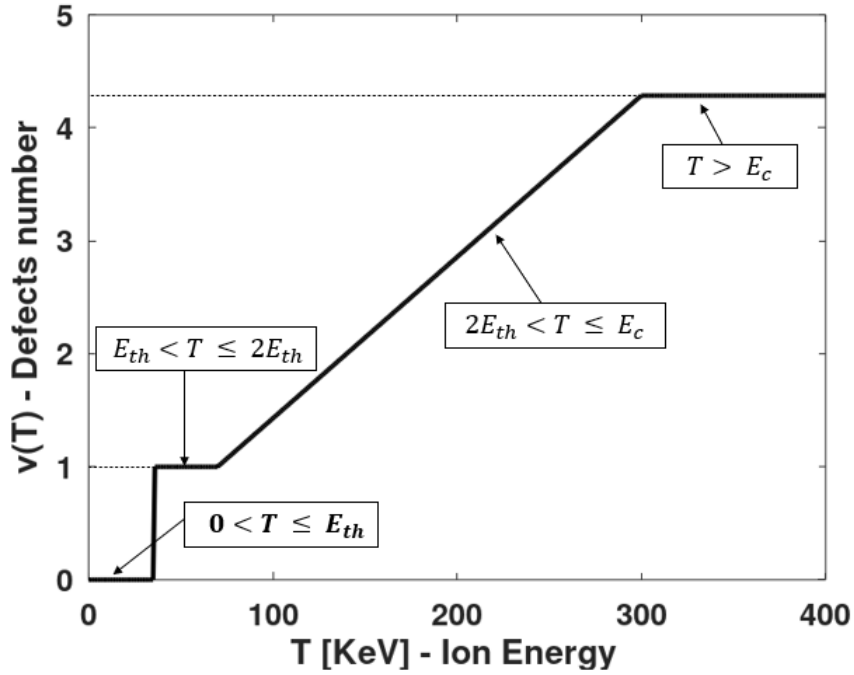


Figure 4.1 - Number of defects $v(T)$ vs the recoiling atom kinetic energy T modelled by Kinchin and Pease.

Lindhard Partition Function $\xi(T)$

In the Kinchin and Pease model, the product $\xi(T) T$ is closely related to the so-called non-ionizing energy loss (NIEL). The term non-ionizing can be confusing because ion species are, in any case, involved in the NIEL interactions. It refers essentially to the interaction between an ion "hitting" the nucleus of an atom and recoiling away against the nucleus's electrostatic barrier. In the general case, NIEL is determined by the relation:

$$NIEL(E) = \frac{N_A}{A} \int_0^{\gamma E} \xi(T) T \frac{d\sigma}{dT} dT \quad \text{Equation 4.3}$$

$$\gamma E = T_{max}; \quad \gamma = \frac{4mM}{(M+m)^2}$$

Where E is the projectile's energy, m and M are the masses of the projectile and material atom, respectively. The value of $\xi(T)$ gives the fraction of the stopping force $S(T)$ (see below for stopping force definition) that goes into NIEL. Therefore $\xi(T) = S_n(T)/S(T)$, with the $S_n(T)$ being the nuclear stopping force. Lindhard approximated the value of $\xi(T)$ as

$$\xi(T) = \frac{1}{1 + F_l (3.4008 \epsilon(T)^{1/6} + 0.40244 \epsilon(T)^{3/4} + \epsilon(T))};$$

$$F_l = 30.724 Z_1 Z_2 \sqrt{Z_1^{2/3} + Z_2^{2/3}}; \quad \text{Equations 4.4}$$

$$\epsilon(T) = \frac{T}{0.0793 \frac{Z_1^{2/3} \sqrt{Z_2} (A_1 + A_2)^{3/2}}{(Z_1^{2/3} + Z_2^{2/3})^{3/4} A_1^{2/3} \sqrt{A_2}}};$$

Here subscript 1 refers to the projectile, 2 to the target, Z is the charge, and A is the mass number. The Lindhard partition function fits quite well with more accurate calculations up to the energy of 1 keV. The reason for the deviation mainly resides in the Lindhard assumption that electrons do not produce recoil atoms, the atomic binding term is negligible, the energy transfer to electrons is small (in a relative measure), and the kinetic energy of the PKA is small compared with the projectile kinetic energy;

Nuclear Stopping Force

For the estimation of DPA with the NRT model, Equations 4.2 and 4.3 use the NIEL and the Lindhard partition function $\xi(T)$. Both are based on the unrestricted energy nuclear stopping force:

$$S_n(E) = N \int_0^{\gamma E} T \frac{d\sigma}{dT} dT \quad \text{Equation 4.4}$$

where N is the atomic density, T is the energy transfer during ion-solid interaction, and $d\sigma/dT$ is the differential scattering cross-section. With the above approach, we are overestimating the DPA since we are also summing up all recoils with T that is smaller than the damage threshold E_{th} .

More appropriate estimation of the DPA will imply using the restricted energy nuclear stopping force for recoils with energy T above the damage threshold E_{th} as:

$$S_n(E, E_{th}) = N \int_{E_{th}}^{\gamma E} T \frac{d\sigma}{dT} dT \quad \text{Equation 4.5}$$

The main feature of this approximation is that it can be employed for any projectile-target combination with any charged particle.

Equivalent Damage

The proportionality of neutron damage to the non-ionizing energy deposition of the PKA (and its damage cascade) in silicon has been widely validated. Consequently, the displacement kerma as a function of energy is used as a damage function defined as follows

$$\bar{F}_D = \frac{\int_0^{\infty} \phi(E) F_D dE}{\int_0^{\infty} \phi(E) dE} \quad \text{Equation 4.5}$$

Where:

\bar{F}_D = average damage produced per neutron (damage constant);

$\phi = \int_0^{\infty} \phi(E) dE$ the total neutron fluence;

Since $\bar{F}_D * \phi_1$ is the total amount of displacement damage, a particle fluence that would produce an equivalent amount of displacement damage is

$$\bar{F}_{DE_{Ref}} * \phi_{E_{Ref}} = \bar{F}_D * \phi_1 \quad \text{Equation 4.6}$$

Where E_{ref} is the reference energy of 1 MeV, and the damage cross-section for Si at 1 MeV is selected as a reference $\bar{F}_{D,1MeV} = 95 \text{ MeV mbarn}$.

Consequently, the 1 MeV equivalent fluence [53] for a given particle is

$$\phi_1 = \frac{1}{F_{D,1MeV}} \int_0^\infty \phi(E) F_D(E) dE \quad \text{Equation 4.7}$$

It is also advantageous to define the ‘‘Silicon Hardness parameter’’ [53] as the averaged damage caused by the present spectrum compared to 1 MeV neutron:

$$HP_{Si} = \frac{\int_0^\infty \phi(E) F_D(E) dE}{\phi(E > 3 \text{ MeV}) SP F_{D,1MeV}} = \frac{\int_0^\infty \phi(E) F_D(E) dE}{\phi F_{D,1MeV}} \quad \text{Equation 4.8}$$

Where $SP = \frac{\phi}{\phi(E > 3 \text{ MeV})}$ is the total particle fluence ϕ ratio over the fluence above 3 MeV.

FLUKA simulations tests

Concerning the test geometry reported in Fig. 4.1, a Silicon (see Table 4.1 for composition and bulk density) slab of 0.2 cm thickness and a surface of 7 x 7 cm² is considered. The slab is irradiated by a spatially homogeneous, ideally-collimated particle field normally impinging on one of the large surfaces. This almost unrealistic emission modality simplifies understanding the modelling of radiation damage. It also allows a quantitative comparison between interactions with the different sources representative of the various irradiation facilities.

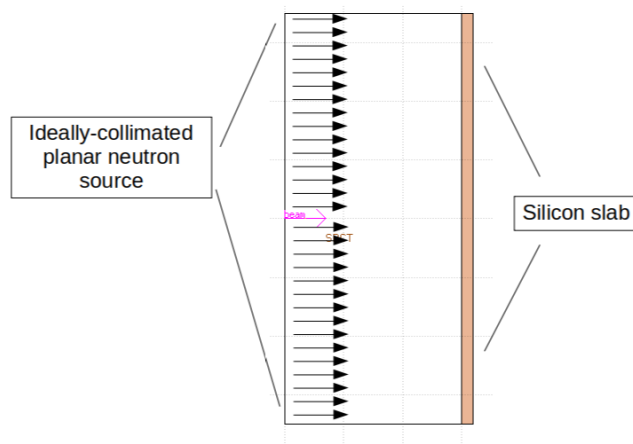


Figure 4.2- Side view: The black arrows show the direction of the collimated neutrons current emitted from the source: it evenly impinges the 7x7 cm² surface of the Si slab.

Table 4.1 - Silicon Isotopic Composition (Bulk Density = 2.29 g/cm³)

Isotope	ZAID	atom fraction
Si ²⁸	14028	0.9223
Si ²⁹	14029	0.0467
Si ³⁰	14030	0.0310

Table 4.2 resumes the FLUKA simulation set and the principal quantity estimated to compare the damage induced in the silicon slab with the various simulated source. The 1 MeV neutron source is exemplificative of the fission spectrum of the TAPIRO nuclear reactor [32] at the ENEA Casaccia research centre, whereas 30 MeV electrons and 70 MeV protons [59] are the maximum energies of the beams available at the ENEA Frascati Research centre. Finally, ⁵⁶Fe has been selected because of its relatively high abundance in GCR (see Chapter 5).

Table 4.2 - Resume of the FLUKA simulation set

Source	Source description	Estimated quantity
⁶⁰ Co	Mixed electron (continuous emission up to 1.5 MeV) and γ photons (discrete emission with primary peaks at 1.17 and 1.33 MeV) from the ⁶⁰ Co decay	Dose, 1 MeV Si equivalent fluence, DPA
1 MeV neutron	A collimated beam from a planar source	
30 MeV electron		
70 MeV proton		
⁵⁶ Fe ions 7 GeV/n		

Simulation results

Table 4.3 reports the results from the FLUKA simulations normalised for one primary particle. As reported in the second column, the deposited energy increases for charged particles with kinetic energy, except for the protons. Due to their particular mechanism, protons suddenly concentrate the deposited energy at the end of the range (Bragg peak). At 70 MeV of kinetic energy, the proton Bragg peak is of the order of centimetres. Consequently, only 5% of the proton energy is deposited in the thin Si slab. The ⁵⁶Fe ion imparts the greatest energy deposition due to its high kinetic energy.

Table 4.3 - Resume of the FLUKA simulation set

Source	Deposited energy	%Fraction of absorbed energy	DPA	1 MeV Si eq. Fluence
	[GeV primary ⁻¹]	%	[primary ⁻¹]	[cm ⁻² primary ⁻¹]
⁶⁰ Co*	6.84E-5	3%	1.43E-25	4.87E-06
1 MeV neutron	1.96E-06	0.19%	3.44E-22	2.38E-02
30 MeV electron	2.20E-02	73%	1.23E-23	1.40E-03
70MeV proton	3.67E-03	5%	3.33E-22	3.31E-02
7GeV/nuc. ⁵⁶ Fe	0.484	0.12%	1.15E-20	4.54E-02

* For ⁶⁰Co, the results are per decay \rightarrow Bq⁻¹

Examining the third and fourth columns of Table 4.3, where the fraction of energy deposited by each particle in the Si slab and the DPA per primary particle are reported, it is possible to compare the radiation damage of each particle.

The low 3% amount of energy deposited by ^{60}Co is mainly caused by the less penetrating electrons that carry a small amount of energy, according to the β^- decay's energy balance. In contrast, the most significant fraction of the decay is carried by γ photons that quickly escape the Si slab.

The 1 MeV neutrons generate a DPA amount of the same magnitude as 70 MeV protons using only 0.19% of the emitted energy versus the proton 5%. The neutrons' high efficiency in generating displacement is due to their electric-neutral nature. Neutrons do not develop an electronic stopping force and collide with the nuclei maintaining their original kinetic energy and justifying the reported high DPA level for neutrons.

30 MeV electrons, in line with their energy deposition modality composed of both electronic and nuclear stopping force, realise the second lower score for DPA after the ^{60}Co despite having the most significant deposited energy fraction (70%) of all series.

Noteworthy, the ^{56}Fe releases only 0.12% of its kinetic energy in the interaction with the slab, but, being its total kinetic energy of 392 GeV, it corresponds (see the last row of the second column of Table 4.3) to an absolute energy deposition of 484 MeV per primary that induced the highest DPA amount.

Coming to the 1 MeV Si equivalent fluences (Table 4.3- fifth column), the reported values reproduce the findings obtained for DPA values on a different scale. This last consideration deserves further studies in perspective using neutrons to accelerate the damage accumulation generated by protons and electrons of higher energies.

The FLUKA simulation of the radFET calibration

Generalities on radFETs and the VT-02 Varadis radFET

The usability of MOSFET, the Metal Oxide Semiconductor Field Effect Transistor, as a radiation dosimeter was first introduced by Holmes-Siedle in 1974 [49]. radFET (Radiation sensing Field effect transistor, a p-channel MOSFET) dosimeters are based on a radiation-induced charge trapping at the Si/SiO₂ interface, causing a variation of the threshold voltage (V_{th}), measured at a constant source-drain current. V_{th} is then a measure for the dose deposited in the gate oxide.

According to Figure 4.3, when the radFET is exposed to ionising radiation, electrons and holes are generated in the gate oxide. A fraction of the carriers recombine immediately, and the remaining part drifts under the electric field, which is present in the oxide. If a positive bias is applied to the gate, the electrons will quickly travel to the gate electrode and leave the oxide. The holes move more slowly towards the silicon substrate and accumulate at the SiO₂/Si interface, where a certain number of them get trapped, causing an increase of positive charges that shift the device flip-on at a higher threshold voltage V_{th} .

When a dose-calibrated radFET is mounted on a proper circuit and located in the zone of interest, it is possible to measure the time-integrated dose in real time.

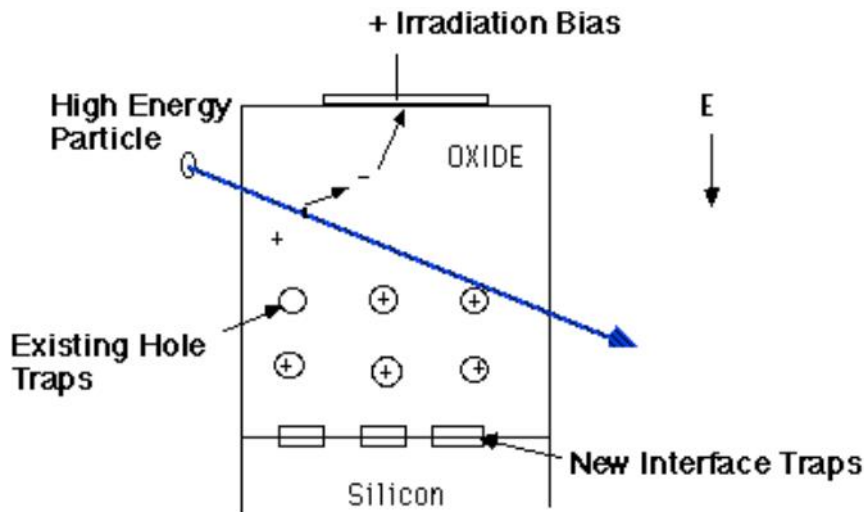


Figure 4.3 – Schematic view of irradiation's radFET mechanism of electron and hole formation.

Consequently, it is interesting to simulate the radFET calibration procedure using FLUKA to investigate the individual contribution of primary and secondary particles within the sensitive volume of the radFET and then compare such results with the ones obtained with particles and energies that cannot be evaluated experimentally, such as the one encountered in the ABCS mission orbit (see Chapter 6).

Specifically, in the limit of the maximum dose of 100 krad [Si] imparted to the Varadis-Vt02 radFET (dose rate of 5 krad/h [Si]) during an experimental calibration procedure with a ^{60}Co source [54], we define a set of FLUKA simulations to compare the doses delivered to the SiO_2 gate and Si substrate of the radFET.

The VT02 is Varadis 400nm RADFET chip packaged in a height lead ceramic side braze package. The part consists of two identical RADFETs, R1 and R2, and a diode (Figure 4.4). The radFETs' gate oxide thickness is 400nm, width = 300 μm , length = 50 μm . The radFETs have individual gate and drain terminals, while the source and bulk are common and connected; this is also the diode bulk contact.

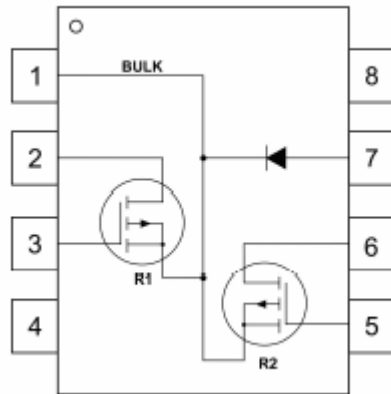


Table 1: VT02 pin-out description.

Pin Number	Description
1	Source/bulk (common)
2	Drain of R1
3	Gate of R1
4	Not connected
5	Gate of R2
6	Drain of R2
7	Diode Anode ¹
8	Not connected

Figure 4.4 – The Varadis VT02 scheme and pins description.

Implementation of the VT-02 radFET geometry in FLUKA

Figure 4.5 reports the dimensions of the actual VT02 radFET on the left side of the picture when a geometric cross-section of the FLUKA model geometry is reported on the right side. The planar source is above the radFET upper surfaces and uniformly irradiates the device.

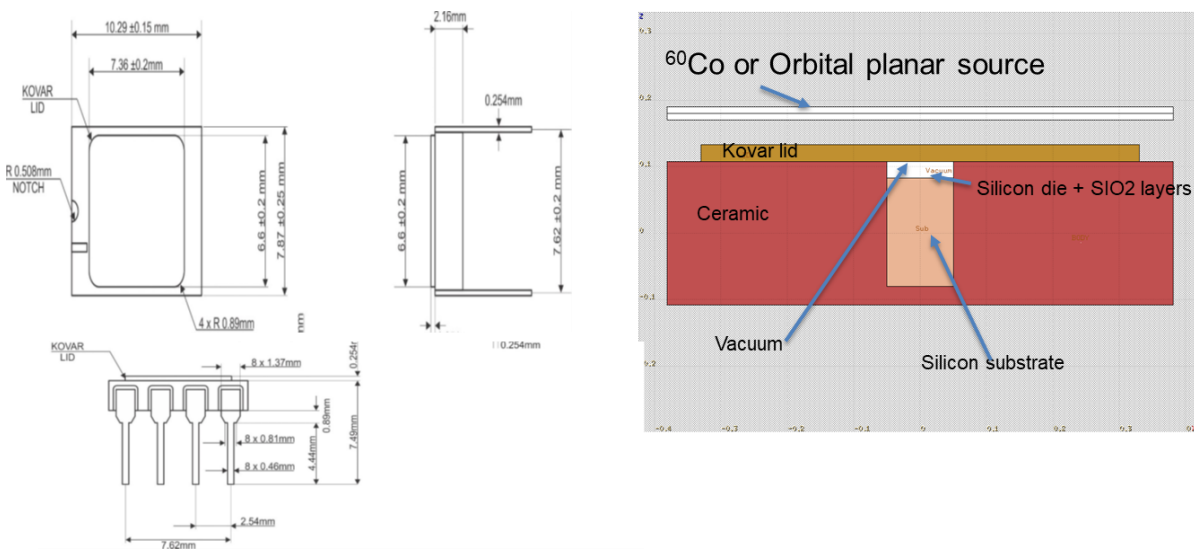


Figure 4.5 – Comparisons of the FLUKA model with the technical drawing of the Varadis VT02 radFET.

Radiation source selected for the simulation

As an orbital radiation source, we use the spectra and intensities of some of the radiation terms determined by SPENVIS for the ABCS mission (see Chapter 5). The ⁶⁰Co source intensity has been derived from the data reported in [54]. Table 4.4 reports the source intensities for trapped particles and some GCR ions used in this simulation. As already said, the orbital source terms will be emitted from a planar source in which the particles are ideally collimated to impinge orthogonally on the radFET surface. Conversely, the electrons and photons originating from the decay have the

direction and energy distributions generated according to the β - decay modality and are not collimated as the orbital sources.

Table 4.4 – Source intensity to normalize the FLUKA results

Source	Source intensity	Units
^{60}Co	4.92E+09	Bq=decay/s
Trap. Electron	7.48E+06	*p/s
Trap. Proton	3.93E+06	p/s
GCR-H	7.0912	p/s
GCR-He	0.51914	p/s
GCR-Fe	1.74E-03	p/s

*p=particle or ion.

The intensity values will be used to normalise the FLUKA results that are given in terms of per primary unit. For example, the volume integrated deposited energy estimated in Table 4.3 by FLUKA for the irradiation of the Si slab with trapped proton is $6.84\text{e-}5$ [GeV primary⁻¹]. Using the source intensity reported in Table 4.4, we obtain the deposited power P in a steady irradiation state according to

$$P = 1.96\text{E} - 6 \left[\frac{\text{GeV}}{\text{primary}} \right] \times 3.93\text{E}6 \left[\frac{\text{Primary}}{\text{s}} \right] = 7.76 \left[\frac{\text{GeV}}{\text{s}} \right];$$

FLUKA simulations set

Table 4.5 reports the simulation set carried out with FLUKA. Due to the challenging task of evaluating the total dose deposited in a layer with a thickness ranging from 400 nm to 50 μm wrapped in materials with relative good shielding properties, we adopted a parallelization strategy for the simulations using quantities of CPU ranging from 288 to 432 according to the simulation complexity. The calculation time ranges from 5 to 20 hours to achieve a meaningful convergence.

Table 4.5 - Resume of the FLUKA simulation set for the radFET model

SOURCE	RADFET	Tot Core	N of Particle Sample (NPS)	excution time (hours)	Estimated quantities
^{60}Co	VT02	288	1.44E+11	4.733	Total dose in Si substrate and SiO2 layer for the contribution of primary and secondary particles
Trapped proton		432	8.64E+10	6.24	
Trapped electron		288	1.44E+11	6.07	
GCR proton		432	6.48E+10	11.94	
GCR ^{56}Fe		432	4.32E+07	13.99	
GCR ^4He		288	1.73E+10	9.68	

Simulation results

Table 4.6 reports estimations of the total ionisation dose (TID) normalised to twenty hours of irradiation on the Silicon substrate and SiO₂ gate of the radFET. The dose estimate in the two target regions was reported in separate contiguous rows. The dose contributions of primary and secondary particles are reported separately in columns.

Concerning the ⁶⁰Co source, the emitted electrons and photons primaries generate secondary ions or protons below the standard energy cut-off during interacting with the radFET structure. Instead, the estimators summed secondary electrons and photons with the primaries. As expected, the total ionisation dose is 100 krad for the silicon substrate, confirming the consistency of the simulation, and the dose for the SiO₂ gate is considerably higher (58%, see first and second rows of Table 4.6).

Table 4.6 – Results for the Total Ionisation Dose accumulated in 20 hours of irradiation (contributes reported in ***bold/italic*** are from primary source particles)

Source	RADFET	Proton	Electron	Gamma	Heavy Ion	Neutrons	Alpha	Total (*)
		TID (krad)	TID (krad)	TID (krad)	TID (krad)	TID (krad)	TID (krad)	TID (krad)
⁶⁰ Co	Si		<i>9.99E+01</i>	<i>6.40E-02</i>				1.00E+02
	SiO ₂		<i>1.58E+02</i>	<i>6.35E-02</i>				1.58E+02
Trapped Electron	Si		<i>1.23E-02</i>	3.18E-06				1.23E-02
	SiO ₂		<i>4.80E-02</i>	2.60E-05				4.80E-02
Trapped Proton	Si	<i>4.58E-02</i>	1.28E-05	3.36E-10	9.28E-07	2.47E-08	4.86E-06	1.66E-01
	SiO ₂	<i>1.62E-01</i>	9.84E-06				3.07E-06	1.87E-01
GCR-H	Si	<i>9.13E-06</i>	1.22E-06	1.99E-11	2.39E-07	1.61E-09	5.00E-07	1.17E-05
	SiO ₂	<i>9.51E-06</i>	9.88E-07	1.22E-11	2.71E-07	2.55E-09	5.72E-07	1.20E-05
GCR-Fe	Si	2.82E-09	2.11E-07	2.64E-12	<i>1.31E-06</i>	5.03E-12	1.02E-09	1.53E-06
	SiO ₂	1.92E-09	1.75E-07	1.49E-12	<i>1.42E-06</i>	6.04E-13	8.40E-10	1.60E-06
GCR-He	Si	1.81E-07	3.51E-07	5.12E-12	3.21E-08	3.91E-10	<i>2.77E-06</i>	3.45E-06
	SiO ₂	1.50E-07	2.88E-07	1.97E-12	3.46E-08	4.32E-10	<i>2.97E-06</i>	3.54E-06

The doses released by the source orbital radiation terms are all well below the 100 krad radFET calibration (see Table 4.6), and all the doses estimated for the orbital condition are well below this calibration limit. Considering that the FLUKA simulations were executed in a very conservative modality, in which no shielding or structural materials attenuate the radiation fields' dose delivery, the effective dose outcomes in mission conditions could remain within the calibration range of the detector.

Table 4.7 reports the contributions of each source term to the cumulative orbital dose showing that trapped protons are the principal dose contributor, followed by trapped electrons. The GCR ions give a minimal contribution to the dose in this orbital condition.

Table 4.7 – Results for the Total Ionisation Dose accumulated in 20 hours of irradiation

Target	Si		SiO2	
Source	TID Rate (rad/day)	% of dose	TID Rate (rad/day)	% of dose
Trapped Electron	14.748	6.892%	57.620	20.42%
Trapped Proton	199.198	93.098%	224.561	79.58%
GCR-H	1.41E-02	0.0066%	1.44E-02	0.0051%
GCR-Fe	1.84E-03	0.0009%	1.92E-03	0.0007%
GCR-He	4.14E-03	0.0019%	4.25E-04	0.0002%
Total	213.966		282.197	

Even though GCR contributions are rare, they may promote stochastically single event upset (SEU) or single event latch-up (SEL) in the surrounding system. Figure 4.6 reports the fluxes of the primary particles into the Si substrate volume. The trapped particle fluxes show a greater intensity characterised by a sharp decrease at increasing energy. Conversely, The GCRs ions show a flat flux with a slow increase toward high energies. These results are not surprising, having in mind that the track-length algorithm estimates the fluxes from the length of the particles' flight within the volume of the selected region: the higher the energy, the higher the probability of a particle track to crossing the region with a single straight track with minimum struggling. Therefore, it is important to stress that the primary particles interact with the whole radFET structure under the irradiation conditions used in the simulations. The secondaries not generated in the target regions may enter inside them to further interact.

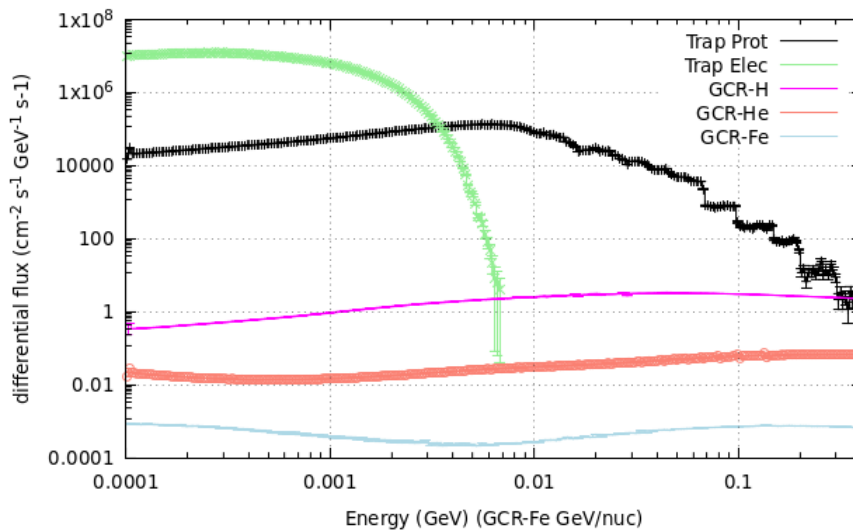


Figure 4.6 – Comparison of the flux energy distribution within the volume of the Si active substrate of the radFET. The energy scale for GCR-Fe is GeV/nucleon.

As the first example, figure 4.7 reports the secondary fluxes of the relevant particle shower generated by the trapped proton in the silicon substrate. The primary proton flux reported in Figure 4.6 is above $1E4 \text{ cm}^{-2} \text{ GeV}^{-1} \text{ s}^{-1}$ in the range of 0.0001 – 0.4 GeV. Conversely, in the same energy region, Figure 4.7 shows that secondary neutrons, electrons, and photon fall immediately below such an intensity. Neutrons are the secondaries that show a significant intensity up to 0.01 GeV indicating that a high fraction of the primary trapped proton has kinetic energy above the threshold

for (p,n) reaction. In absolute, their flux does not significantly contribute to the dose delivery but can induce SEE in other neighbour electronics.

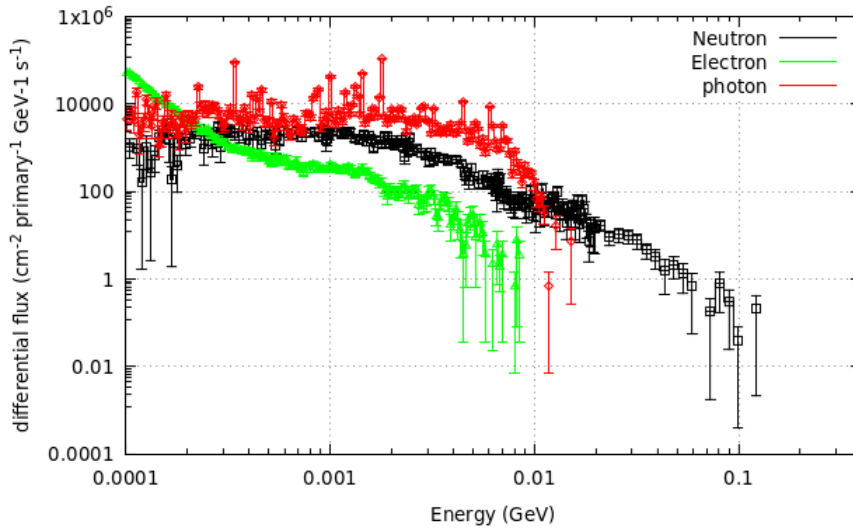


Figure 4.7 – Comparison of the secondary particles flux energy distributions generated within the Si substrate of the radFET by the trapped proton source: neutron (black), electron (light green), and photon (red).

Coming to the more energetic GCR proton, Figure 4.8 shows a richer set of secondary particles: besides neutron, electron, and photon, there are ions such as ^4He (α particles) and heavy ions (i.e. nuclei whose $Z > 2$) that originated from spallation reactions with the nuclei of the whole radFET structure. All the secondary particle spectra have a high-energy tail that candidate them to be responsible for SEE.

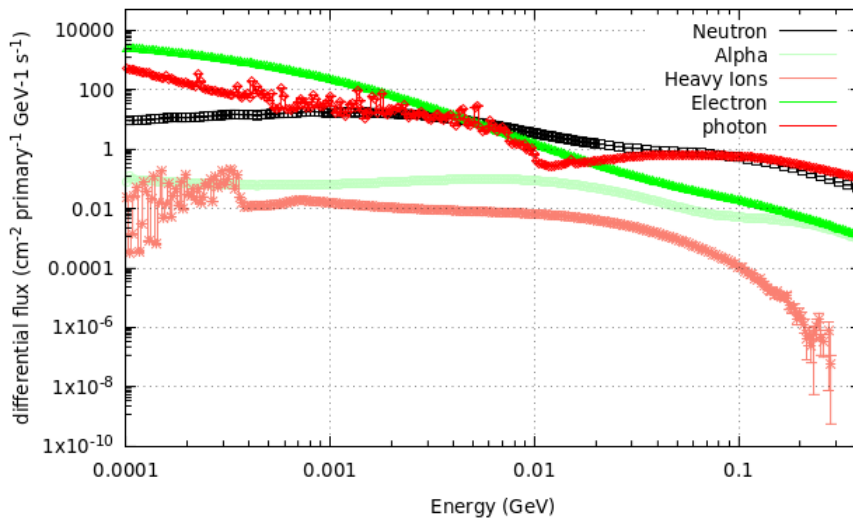


Figure 4.8 – Comparison of the secondary particles flux energy distributions generated within the Si substrate of the radFET by GCR-H source: a) neutron (black), α (green), Heavy ion (salmon), photon (red), and electron (light green) in the Si substrate.

The secondary particle fluxes generated by the GCR-HE (Figure 4.9) show a very similar pattern of GCR-H but shifted to low intensities. Figure 4.10 reports the secondary particle fluxes generated by the ^{56}Fe , where heavy ions and neutron shows very similar energy distributions above 0.1 GeV with a tail up to 100 GeV.

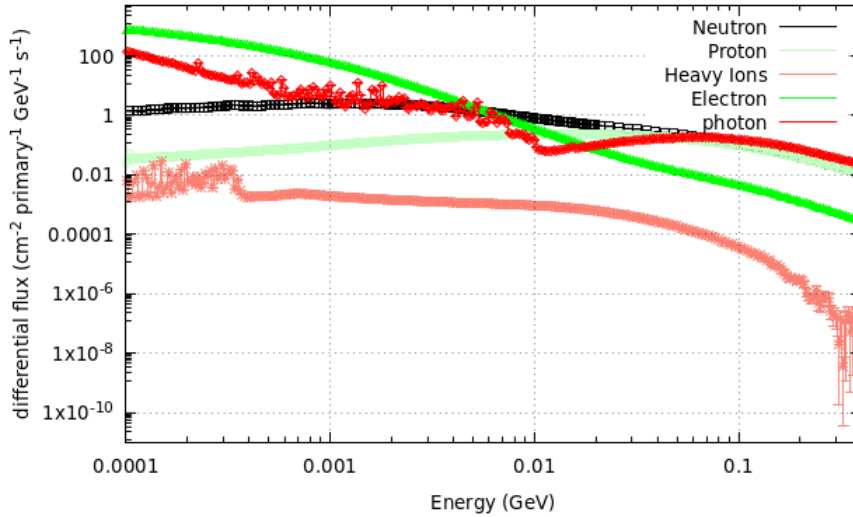


Figure 4.9 Comparison of the secondary particles flux energy distributions generated within the Si substrate of the radFET by GCR-He source: Secondary neutron (black), proton (green), Heavy ion (salmon), photon (red), and electron (light green) in the Si substrate.

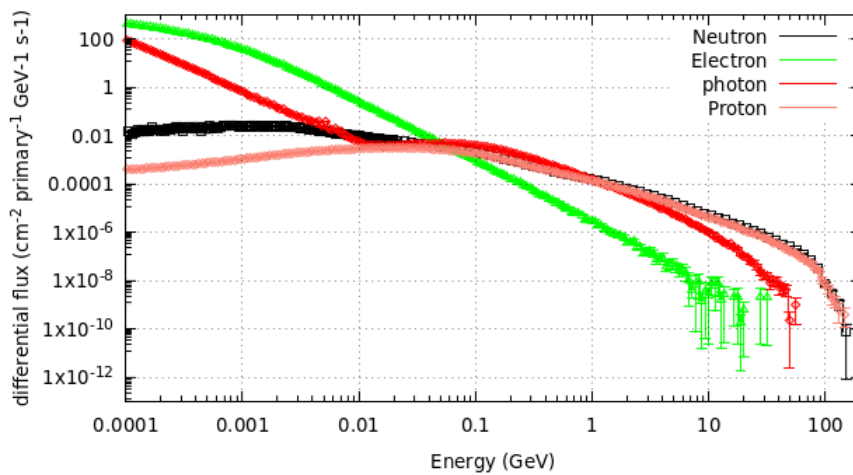


Figure 4.10 – Comparison of the secondary particles flux energy distributions generated within the Si substrate of the radFET by the GCR-⁵⁶Fe source: neutron (black), proton (salmon), photon (red), and electron (light green) in the Si substrate.

Conclusions

The new electronic components must be qualified for the diverse and dynamic radiation fields encountered in aerospace activities. However, the existing irradiation facilities individually do not cover the whole spatial radiation environment.

Expecting the new generation of dedicated irradiation facilities under design, a comparative study of the specific features of the irradiation test carried out on existing ground facilities can be compared to look at the differences and complementarities.

Being the accessibility, safety and security requirements of the irradiation plant (accelerators, research nuclear reactors, and decay sources) very different, the first comparison of

such facilities has been made using a simple irradiation model of a silicon slab to simulate the radiation damage of neutrons, protons, electrons, and ^{60}Co electrons/photons irradiation.

The results, in light of a brief review of the radiation-induced damages on solids, show that the 1MeV equivalent silicon damage fluence could be an essential quantity to be used to compare the level of damage introduced by irradiation tests executed on different facilities to the same electronic components.

The radFET dosimeter has been adopted as an integral radiation monitor within the payload of the ABCS mission (see Chapter 6). Their calibration has been carried out, as usual, with the ^{60}Co radiation up to the limit of an integral dose of 100 krad [Si]. In addition, a set of comparative FLUKA simulations show that the usual dose delivered during the mission could be within the calibration dose range.

The simulation outcomes also show that planning accurate irradiation experiences should be possible to study the secondary particles' radiation fields to quantify the level of SEE in the electronic systems.

Chapter 5 – Radiometric Analysis of the ABCS payload

Introduction

AstroBio Cube Sat (ABCS) is a 3U CubeSat [55] designed and developed in partnership between INAF, the Italian National Institute of Astrophysics, Sapienza University of Rome, and Alma Mater Studiorum University of Bologna, on the Vega C Maiden Flight launch opportunity offered by European Space Agency (ESA) with the support of the Italian Space Agency (ASI) [56]. The project aims to test an automated onboard laboratory in space environments based on Lab-on-Chip (LoC) technology [57] to provide a highly integrated in-situ multiparameter platform that uses immunoassay tests to exploit chemiluminescence detection.

In-orbit validation of the proposed technology would represent a significant breakthrough for the autonomous execution of bio-analytical experiments in space with potential application in planetary exploration for biomarkers detection, astronauts' healthcare, space stations' environmental monitoring and more (see, for example [58]).

The ABCS will be deployed within the inner Van Allen belt (5830 km altitude). At this altitude, ABCS will experience radiation dose orders greater than Low Earth Orbit, where CubeSats usually operate. According to the calculation carried out with SPENVIS [3], the total flux intensity in the mission orbit is $1.41E+07$ particles/cm²/s. Trapped particles (electron and proton) are the main component of the total flux that also comprises GCR ions and occasionally SEP. As already seen, the interaction of each source particle with the satellite structure generates a cascade of secondary with lower kinetic energy and a higher probability of interacting further within the satellite interior, releasing dose, causing damage to the material, and potentially altering the subsystem's functionality.

This work reports the preliminary modelling activity performed with the FLUKA Monte Carlo code to estimate the Total Ionising Dose (TID) and the 1 MeV neutron Silicon equivalent damages (SI1MEVNE) fluence on some components of the ABCS payload and the external Solar Panels (SPs) delivered by the mission orbital source terms. We also estimate the effectiveness of a shielding solution for the payload designed within the mass mission budget.

Finally, we started a preliminary comparison of the orbital simulation results with the one obtained from a full-scale simulation of an ABCS neutron irradiation within the Thermal Column Cavity (TCC) of the TAPIRO nuclear reactor facility at ENEA-CASACCIA Research Centre that is included in the ASIF initiative between ASI, ENEA, and INFN [7-9] for the qualification of electronics components and system for aerospace application.

These results will constitute the basis for defining an experimental setup within the TCC of the TAPIRO to test some LoC functionality during neutron irradiation. Also, comparing the simulation results with the data collected during the ABCS mission will allow a quantitative tuning of the modelling tools.

Calculation Assumption and Model definitions

Implementation of the ABCS layout's relevant features in the FLUKA and MCNP models

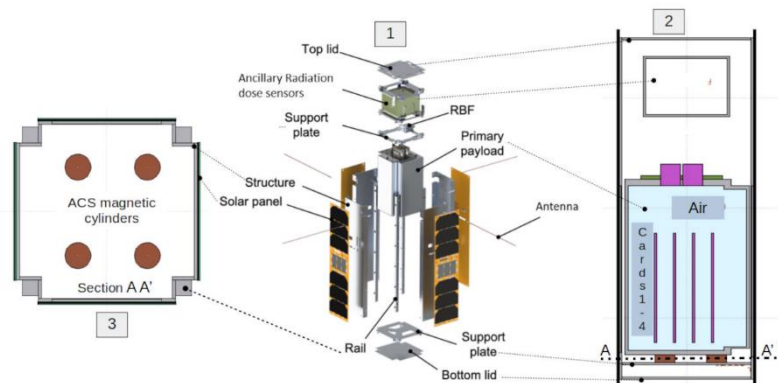


Figure 5.1 - Comparison of the satellite's exploded view (1) with the layout's sections obtained by FLAIR (FLUKA Advanced Interface) in the FLUKA model. The model layout retains only the geometrical features and the materials necessary for particle transport and shielding considerations. In particular, section (2) shows the pressurized primary payload, the ancillary radiation dose sensors box, and the upper and lower support plate. Section (3) shows the position of the Attitude Control System (ACS) magnetic cylinders.

As reported in the exploded view of Fig. 1, we can distinguish the satellite skeleton made in aluminium Al5046 alloy constituted by four side panels, a top and bottom lids, all mounted on four rails. On the external surface of each side, there is a solar panel. The pressurized primary payload (the ABCS payload in the following) is contained in an Al5046 box, in which is located an LoC with its readout board, the interface board with pumps and drivers for fluid injection, radFETs for radiation dose measurements, a pack of rechargeable batteries, and a heater coupled with a passive multi-layer insulation system ensures payload temperature control.

The primary payload aims to perform immunoassays using light detection of immobilized target molecules within the chip, exploiting chemiluminescence reaction at controlled temperature and pressure.

As a secondary payload, the satellite interior hosts an Al5046 aluminium alloy box containing the ancillary radiation sensor system to monitor the orbital radiation dose levels.

Due to the mass budget restriction, the implemented Attitude Controller System (ACS) is based on hysteresis rods and permanent magnets passive system that should ensure an orthogonal orientation relative to the Earth's magnetic field lines after the satellite deployment. The magnetic cylinders are located between the bottom lid and the support plate (see section AA' in Fig. 1). In contrast, the hysteresis rods are inserted in each side panel of the satellite structure.

Our simulation goals are preliminarily limited to estimating shielding solution effectiveness in the ABCS payload and the design of irradiation experiments with fission neutrons, so we simplify the layout as reported limiting the number of components to the elements that act as primary

shielding materials for the ABCS payload, also simplifying the interpretation of the secondary particles showers generated during the simulations. Furthermore, the design of the neutron irradiation requires a future study of the level of activation of the materials to avoid long cooling periods that prejudicated the execution of post-irradiation tests in external laboratories.

Figure 5.2 shows plant and side cross-sections obtained by FLAIR [25] on the model implemented for the particle transport simulation. The components implemented in the FLUKA model are the skeleton structure of the satellite, the solar panels, the ABCS and secondary payload boxes, the support plates, the magnetic cylinders, the connector plugs on the top of the ABCS payloads and four Print Circuit Board (PCB) and the air volume contained within it. Comparing the model layout with the exploded view of fig. 1, we realize that the estimation of the dose rates or the equivalent damages, due to the absence of the excluded components shielding contribute, overestimates the quantities experimented in the complete satellite layout.

In the future, we will model the complete ABCS layout to compare the estimated dose response with the data obtained from the mission telemetry. Finally, we will perform a complete radiometric study.

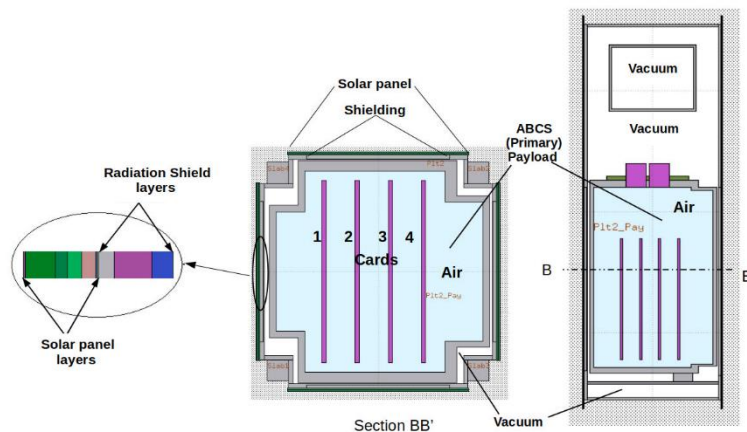


Figure 5.2 - On the left, the image reports the magnification of the external layers structure of the solar panel and the shielding solution, corresponding to the ones illustrated in Table 1. The central cross-section, from which the magnification belongs, is taken along the B-B' direction located at the height of the ABCS payload, as shown in the rightmost part of the figure. The two sections help to clarify further the simplified mass distribution assumed in the FLUKA model.

Figure 5.2 also shows a magnification of the structure of one of the ABCS long sides constituted by a sequence of layers, from out to in, representing the materials of the solar cell, the PCB Stack-Up, and the aluminium panel constituting the innermost boundary.

Due to the satellite mass budget limit, we limit the shielding to an area (6.7 cm x 15.05 cm) to protect further the ABCS payload around the four side panels' borders. In such an area, we remove from the external the aluminium for a total thickness of 0.2 cm, substituting it with a first tungsten layer (thickness = 0.06 cm) to stop charged particles, followed by a second layer of epoxy resin (thickness = 0.1 cm) that stops secondary charged particles, maintaining a residual aluminium thickness of 0.04 cm.

This solution, whose materials layer sequence has been optimized in preliminary simulations of a simple slab model, takes into account the alternation of high Z materials that stop charged particles with light nuclei material able to slow down secondary neutrons, increases the total ABCS total mass of 300 g remaining within the mass mission budget. Table 5.1 resumes the layers sequence, material compositions for the solar cell, and the adopted shielding solution.

Table 5.1 - Materials used for each FLUKA region constituting Solar cell and further shielding layers

Component	*Layer	Material
Solar panel	Anti-Reflex	SiO ₂
	Top Cell	InGaP (N/P)
	Middle Cell	GaAs (N/P)
	Bottom Cell	Ge
	Substrate	Ge (P)
	Contact layer	Ag
Shielding Solution	1 st layer	Metallic Tungsten
	2 nd layer	Epoxy
	3 rd layer	Aluminium

*All layers are listed going from the outside to the inside of the structure.

To simulate the ABCS's neutron irradiation in the TCC position of the TAPIRO, we export the ABCS geometry definition contained in the FLUKA input to the MCNP formalism using a utility contained in the FLAIR package. As reported in Figure 5.3, we insert the ABCS geometry into the TAPIRO's MCNP input deck, locating it inside the TCC irradiation position.

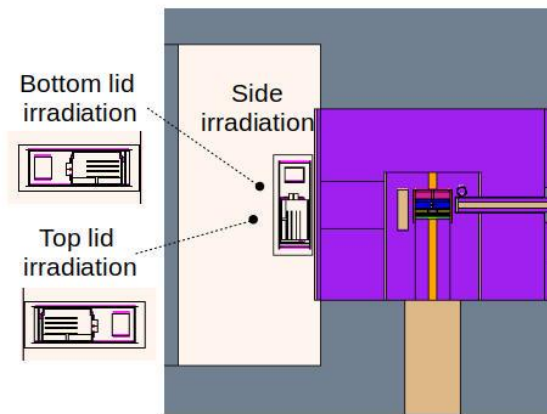


Figure 5.3 - Geometric cross-section obtained with the MCNP plotter shows the ABCS geometry's integration into the TAPIRO's MCNP model. The TCC hosts the whole satellite on the outermost reflector surface. The RC1 (Radial Channel 1) irradiation position is also visible on the opposite side of the core. The iconic representations of the ABCS on the left side of the image describe two alternative static orientations considered for irradiation in the preliminary calculations (see text).

In some preliminary simulations, we consider three different irradiation layouts to evaluate the differences in the responses due to the ABCS orientations within the TCC (see Figure 5.3) in the MCNP simulations. First, we locate one of the ABCS sides in the proximity of the external reflector (side irradiation). In the second, we place the ABCS to position the bottom lid near the reflector

(bottom lid irradiation). Finally, we locate the top lid near the reflector (top lid irradiation).

Comparing the intensities of the SI1MEVNE fluxes (see Chapter 4) to card four in preliminary MCNP simulations, we find that the side irradiation maximizes the equivalent flux. In contrast, the equivalent fluxes of the bottom and top lid irradiation positions have 63% and 30% of the side positions.

Having this figure in mind, we decided to perform the simulations using the side irradiation position, reserving, for future study, the search for an optimized irradiation geometry.

Orbital source term definitions

The Van Allen radiation source includes trapped particles (protons and electrons), GCR, and SEP ions. As already seen, the SW cyclic emission has, on average, an energy distribution less energetic than the GCR's one that reaches ultra-relativistic kinetic energies. Therefore, to define the whole orbital radiation source, we implement in SPENVIS the ABCS mission at the altitude of 5830 km on a circular orbit.

The quantification of the trapped particles' source term deserves some clarification based on the information reported in the online manual of the SPENVIS code.

For example, in SPENVIS, the standard package to evaluate the trapped protons and electron source terms uses the A8 model based on the data collected from a series of satellites up to 1970.

SPENVIS software is black-boxed, as often happens for engineered codes, and the A8 system is called, requesting an alternative evaluation at maximum or minimum generic solar activity.

Despite the modification of the geomagnetic field and the new data collected during recent years assigning the AP8/AE8 estimation a factor two of uncertainty, it remains the reference for the satellite design.

For this reason, the AP9/AE9 models have been introduced into a separate module that the users can invoke for the sole evaluation purpose. Based on a statistical foundation, the A9 infers the trapped particles' source terms from more recent data and updates geomagnetic field models considering the solar activity of the specific mission period.

In order to quantify the possible response differences in the simulation due to the trapped particle source terms, we calculate the intensity and the energy spectra of the trapped particles using the AP8/AE8 models at both solar minimum and maximum and also using the AP9/AE9 models.

Figure 5.4 reports the considered ABCS' s orbital trajectory and the trapped proton's total flux intensity along the track, comparing the AP8 maximum and minimum responses. According to SPENVIS AP8 calculation, trapped protons are the most effective radiative component, and the ABCS is subjected to maximum irradiation for a significant part of its orbit. This situation can be worst if a SEF takes place during the mission.

It is also apparent that the flux intensity level reported in the chromatic scale for solar minimum and maximum are very close. Therefore, to remain conservative, we always rescale all the presented

simulation results to the total intensity averaged on the mission time using A8 for the trapped particles and the condition of solar minimum for GCR. Finally, we considered the averaged flux intensity during the week of maximum activity within the mission period concerning SEP emissions.

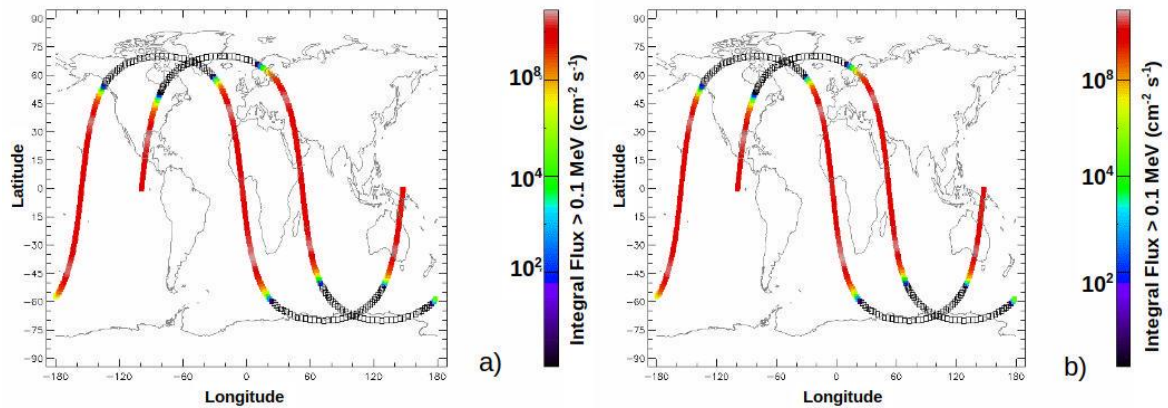


Figure 5.4 - ABCS ground track on a world map: The proton flux intensity along the ABCS orbit, estimated by the AP8 models, is reported for solar minimum (a) and maximum (b) on the side logarithm chromatic scales. In both cases, ABCS is subjected to the maximum flux intensity for a significant part of its orbit.

Figure 5.5a compares the trapped electron energy distribution for the averaged mission fluxes obtained with the AE8 and AE9 models. The AE8 results yield identical spectra and almost the same total flux intensity at solar minimum and maximum (see Table 2). In contrast, the AE9 model foresees a lowering of the electron population in the energy range from 0.001 to 0.005 GeV and a higher total flux intensity (Table 5.2).

Figure 5.5b and Table 5.2 report the same comparisons for trapped protons. The AP8 energy spectra are coincident for solar maximum (total flux intensity $5.08E+06 \text{ cm}^{-2} \text{ s}^{-1}$) and minimum (total flux intensity $5.02E+06 \text{ cm}^{-2} \text{ s}^{-1}$).

The AP9 model shows a more marked spectral difference for trapped protons relative to AP8: the flux intensity from $1E-04$ to $1E-03$ GeV is higher than in AP8. Conversely, for energy greater than $1e-03$ GeV, up to 0.2 GeV, the AP9 flux intensity is systematically lower than AP8 one. The AP9 total flux intensity is $7.95E6 \text{ cm}^{-2} \text{ s}^{-1}$.

Although it goes beyond the scope of the present work, a possible explanation of the closeness of the spectral properties of trapped particles at solar minimum and maximum could be attributed to the altitude of the ABCS, where, according to the SPENVIS manual, the model becomes inaccurate.

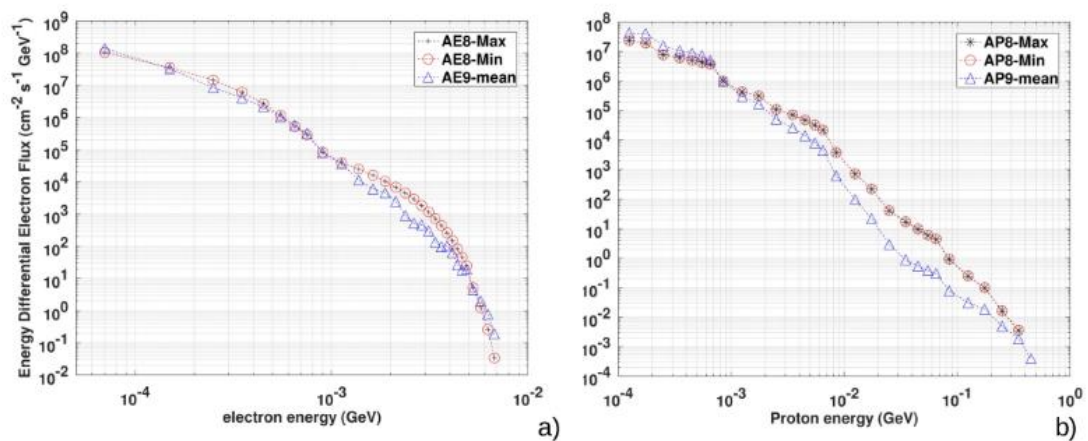


Figure 5.5 - Comparison of the energy distributions of the trapped electron (a) and proton (b) fluxes at the ABCS orbit according to AE8/AP8 (at solar maximum and minimum) and the AP9/AE9.

In light of the data outcomes, we decided to carry out the FLUKA simulations using trapped particle source terms obtained from AP9/AE9 and AP8/AE8 models and discuss the differences in the simulation results.

The complete SPENVIS output generates information for GCR and SEP ions emission with atomic numbers between hydrogen and uranium ($Z=1-92$). We use pre-processing software to separate the SPENVIS ion data into individual files with a format accepted by FLUKA. Figure 5.6 compares the total emission intensities for GCR and SEP ions in a limited range of the atomic number Z from 1 to 30 (from hydrogen to zinc) foreseen by SPENVIS in the ABCS orbit.

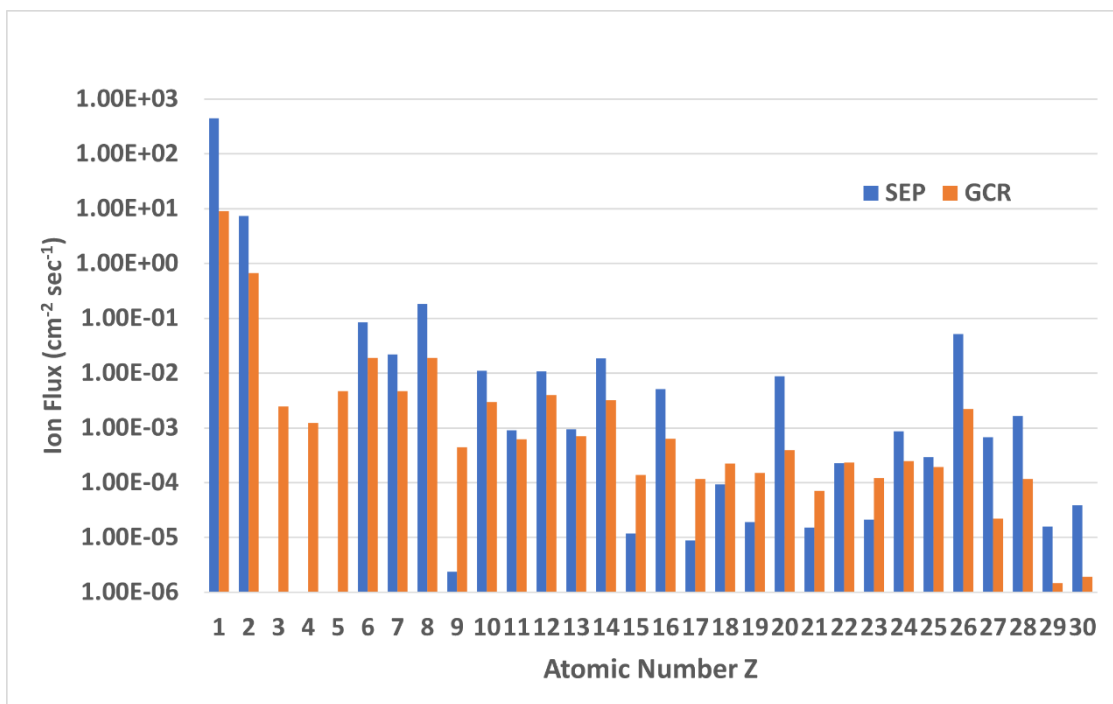


Figure 5.6 - Comparison of the flux intensity (logarithm scale) for ions emission from GCR and SEP (Ions Atomic Number range $Z= 1 -30$).

Table 5.2 shows the selected particle contributions based on their intensity and transport characteristics: trapped electrons and protons, protons, and helium from GCR and SEP. Despite their weak intensity, we also selected GCR iron and SEP oxygen because their transport involves high-energy nucleus-nucleus collisions between nuclei heavier than helium and yield peculiar particle shower patterns that we want to investigate. Trapped proton and electron worth 99.99% of the total flux. The GCR accounts for only 0.001-0.003%, and the SEP ions represent 0.0033-0.0016 % of the total emission.

Table 5.2 - Total flux intensities of the orbital source components from SPENVIS

Source Term	AP8/AE8 min Total Flux [cm ⁻² s ⁻¹]	AP9/AE9 Total Flux [cm ⁻² s ⁻¹]		
Trapped Proton	5.02E+06 (35.67%)	7.95E+06 (28.54%)		
Trapped Electron	9.05E+6 (64.32%)	1.99E+07 (71.45%)		
Source Term	Total Flux [cm ⁻² s ⁻¹]	H Flux [cm ⁻² s ⁻¹]	⁴ He [cm ⁻² s ⁻¹]	ion representative of Z > 2 [cm ⁻² s ⁻¹]
GCR	9.78 (0.0001%)*	9.05 (92.53%)**	0.663 {6.77%}	0.00222 {0.02%}; ⁵⁸ Fe
SEP	457 (0.0033%)	450 {98.31%}	7.33 {1.68%}	0.182 {0.04%}; ¹⁶ O

*% fraction of the total flux is between brackets; **% fraction of the total flux in the specific source term is between curly brackets.

Figure 5.7 compares the energy spectra used in the FLUKA simulation for electrons and ions reported in Table 2. The most intense emission is for the trapped electron, showing the lowest maximum kinetic energy compared with the other components. Trapped proton and SEP emissions show their maximum energy emission at 0.1 GeV/nucleon. In contrast, GCR emissions reach the 100 GeV/nucleon that, for example, sets the maximum total kinetic energy of ⁵⁶Fe to 5.6 TeV. Consequently, we used the FLUKA version that includes the DPM (Dual Parton Model DPM) [12] module to simulate the nucleus-nucleus collision in this energy regime.

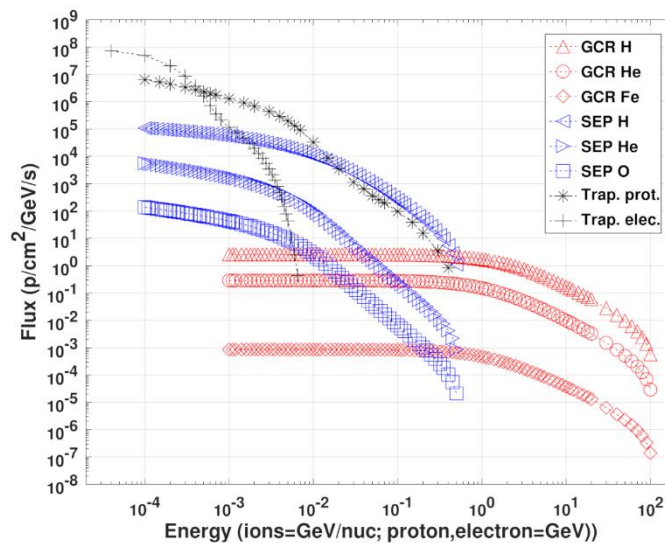


Figure 5.7 - Comparison of the energy differential fluxes of the source terms used in the FLUKA simulations.

The data furnished by SPENVIS belongs to the solution of the dynamic interaction of the geomagnetic field with the plasma of charged particle distribution on a large spatial scale. The ACS control allows pointing the Z axes (i.e. the axis normal to the bottom and the top lids - see Figure 5.1) of the ABCS parallel to the Earth magnetic vector after a short period of rotational kinetic dissipated thermal energy. Several ACS analysis was performed to assess ABCS pointing performance, assuming different starting angular velocities after the deployment. Regardless of the initial condition, the results indicate that ABCS reached the desired attitude reported in Table 5.3 within one day after the deployment.

Table 5.3 - ABCS target orbit

Mean orbit	
Semi-major axis	12218.209 km
Inclination	70.1432 degree
Height of the perigee	5830 km
Height of the apogee	5849 km
True anomaly	3.38 degree
Mean anomaly	3.37 degree

To define the emission source to be used for the FLUKA simulations on the ABCS space scale, we consider the following:

1. From some preliminary FLUKA simulations tests carried out with protons on the ABCS geometry, we test several irradiation geometries, similar to the ones reported in Fig. 3 for the neutron irradiation in TAPIRO, realizing doses rate in the ABCS payload ranging from 4% to 50% of the doses imparted from isotropic particles emission on a spherical surface having the satellite in its centre that is very similar to assume a random satellite rotation. Consequently, the most severe irradiation geometry encountered by the satellite should be in the period in which the ACS control has not yet stabilized the satellite in the target orbit.
2. On the local satellite scale, ions and electrons have a negligible probability of mutual interaction, allowing the source's decomposition in additive non-interacting terms.
3. The GCR and SEP radiation terms have weaker intensity than trapped particles. Light ions (proton and α) dominate the heavier ions.

Consequently, we defined a spherical surface (radius 20 cm) with the satellite in its centre. The emission points are randomly sampled on the sphere surfaces and inward-directed with a uniform distribution within the admitted angular range.

This spatial distribution ensures an isotropic particle flux in the interior sphere space that maximizes the fraction of the particles impinging the satellite body and corresponds to a conservative irradiation geometry against which evaluates the shielding solution. As stated at point 2, we split the whole source into many sources, one for each kind of particle, to run in separate simulations. We sum up the individual source contributions to obtain the overall values of each estimated quantity.

Finally, we simplify the GCR and SEP radiation terms, considering the proton and alpha primary emission and neglecting, according to point 3, the contribution of all the heavy ions except ^{56}Fe for GCR and ^{16}O for SEP.

The source term for simulation with MCNP in the TAPIRO reactor

The TAPIRO reactor, located in the ENEA-Casaccia Research Centre of Rome-Italy, is a fast neutron spectrum irradiation facility. Since 1971, TAPIRO has been used to design shielding solutions for fast nuclear reactors, test radiation damage for electronic components, and do dosimetry studies. TAPIRO's nominal power is 5 kW. The Helium-cooled core is a cylinder of Uranium-Molybdenum alloy surrounded by a Copper reflector.

The control rod system, housed in the copper reflector, comprises five movable cylindrical sectors that regulate the reactor power by increasing or reducing the neutrons' escape from the core. A complete MCNP [32] model of the facility has been developed and validated over the years (see, for example, [33]) and continuously upgraded to perform the design of neutron irradiation experiments.

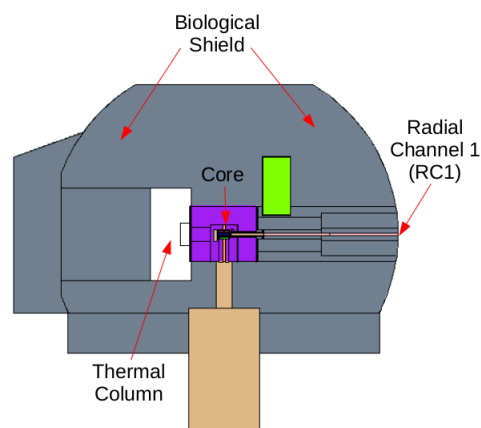


Figure 5.8 - Geometric cross-section of TAPIRO reactor MCNP model showing the TCC and the Radial Channel 1 irradiation position: the area near the external reflector is the region in which ABCS will be located (see also Figure 5.3).

Figure 5.8 shows the irradiation position selected for the comparative simulation tests. The Radial Channel 1 (RC1) irradiates a relatively small sample, and its energy neutron spectrum is stable and has been experimentally measured [33].

As confirmation of the goodness of the TAPIRO model, a comparison of the measured and simulated neutron spectra in the RC1 channel is reported in Figure 5.9 (blue and black curve, respectively), showing a good agreement between the two curves. The simulated spectrum has the maximum relative error of 1% in the energy range from 0.1 eV to 20 MeV. The experimental spectrum has been measured using the unfolding method based on the activation of metallic foils and the measurements of the activation rate by γ -spectrometry: in this case, the error is 4%.

Due to its significant volume, which can host the whole ABCS satellite, the thermal column has a neutron flux and energetic distribution that could change according to the experiment layout, and it needs, each time, a dedicated qualification. For this reason, figure 5.9 also reports the simulated spectrum in an air-filled volume of the TCC that will host the ABCS layout (blue curve).

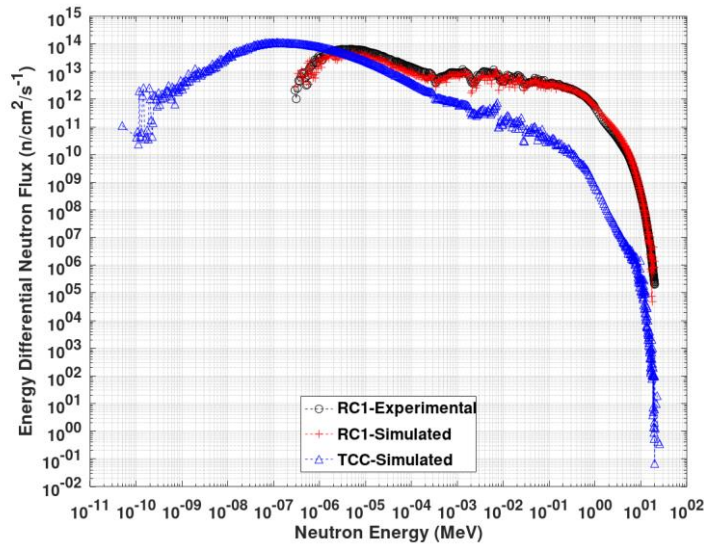


Figure 5.9 - Comparisons of the neutron energy distribution obtained in RC1. The black curve is obtained from experimental measurements, and the red from the TAPIRO MCNP model: the two curves are in good agreement. An MCNP estimate of the neutron flux in the TCC is also reported (blue curve) for the discussion on the design of the ABCS irradiation experiment.

As expected, RC1 has a more intense neutron flux because it is closer to the core, and its energy distribution retains the characteristics of a pure fission spectrum. Conversely, the neutrons arriving in TCC from the core must escape from the reflector and slow down in the reactor structure. Consequently, they show a lower flux intensity and a low-energy distribution with a broad maximum in the epithermal neutron energy range (1-100 keV). However, since those features are entirely congruent with the expected neutron transport pattern for the TAPIRO and considering the agreement between experimental and simulated results in RC1, the model appears adequate to simulate the ABCS neutron irradiation in the TCC.

Consequently, we run an MCNP simulation in the KCODE [26] modality that generates the fission distributions of the reactor core using an iterative fission scheme and transports the generated fission neutrons through the system. The MCNP iteration scheme refines the fission distributions until it becomes compatible with the reactor configuration and the fission chain reaction's self-sustain condition. Thus, the model approaches a steady state that could be rescaled to a user's defined fission power. In a previous work [32], the MCNP model reproduces the experimental TAPIRO critical configuration.

Description of the MCNP and FLUKA Simulation Sets

To investigate the shielding solution effectiveness, we need to run two simulations for each source term, respectively, with the unshielded and shielded layout, for a total of sixteen simulations.

Table 5.4 reports the parameters adopted to minimize the relative error, within a sustainable simulation time, for each source term used on the configurations with the shielding protection of the satellite structure (“No Further Shielding” – NFS) and the one with further shielding (“Further Shielding” – FS) due to the layered shield solution (see paragraph 2.5).

A detailed analysis of the optimization of the estimator’s relative error goes beyond the scope of the present paper. For example, the relative errors reported in the last columns of Table 5.4 deal with the absorbed doses in the ABCS payload. Their values are below the 2% of relative error except for trapped electrons that, due to their low mean emission energy, were severely attenuated by the satellite structure and the shielding materials yielding more dispersed values of the mean TID rate with a relative error ranging from 6% to 10% that is still acceptable for this type of simulation.

Table 5.4 Resumes of the simulations executed in the present work and performance on CRESCO

Source Term	Case	number of particles per CPU (p)	Number of CPU per simulation (N)	Overall number of particles per simulation (P)	CPU time per particle (seconds)	Simulation execution time (hours)	Relative error ($E_r = \frac{\mu}{\sigma} \times 100$)
Trapped Proton	NFS ⁺	4.00E+08	64	2.56E+10	5.43E-05	6.0	1.47%
	FS ⁺⁺	4.00E+08	64	2.56E+10	4.94E-05	5.5	1.88%
Trapped Electron	NFS	4.00E+08	64	2.56E+10	5.03E-05	5.6	6.24%
	NFS	4.00E+08	64	2.56E+10	4.94E-05	5.5	9.89%
GCR Proton	FS	1.00E+07	64	6.40E+08	8.27E-04	2.3	1.14%
	NFS	1.00E+07	64	6.40E+08	8.27E-04	2.3	1.07%
GCR α (⁴ He)	FS	5.00E+06	64	3.20E+08	1.76E-03	2.4	1.26%
	NFS	5.00E+06	64	3.20E+08	2.17E-03	3.0	1.27%
GCR ⁵⁶ Fe	NFS	1.00E+05	192	1.92E+07	2.76E-01	7.7	1.21%
	FS	1.00E+05	192	1.92E+07	3.24E-01	9.0	1.13%
SW Proton	NFS	1.00E+08	64	6.40E+09	1.81E-04	5.0	1.18%
	FS	1.00E+08	64	6.40E+09	1.81E-04	5.0	1.17%
SW α (⁴ He)	NFS	1.00E+08	64	6.40E+09	1.64E-04	4.6	1.52%
	FS	1.00E+08	64	6.40E+09	1.62E-04	4.5	1.55%
SW ¹⁶ O	NFS	1.00E+08	64	6.40E+09	2.75E-04	7.6	1.18%
	FS	1.00E+08	64	6.40E+09	2.81E-04	7.8	1.16%

*NFS= “No Further Shielding” configuration; **FS= “ Further Shielding” configuration; (see paragraph 2.5, Eqs 5 and 5b for details);

Also, in the case of the TAPIRO MCNP model, we performed the first simulation test with the NFS and FS layouts. Next, we use an MCNP 6.2 parallel version compiled and linked with the OPENMPI library (Open Message Passing Interface) on the CRESCO computational facility. The simulations run on 288 CPUs for five hours, obtaining a relative error E_r of approximately 1% for all the estimators.

Estimation of the TID and SI1MEVNE in selected satellite components

It is convenient to recall that a user-defined region is a space volume filled with a single homogeneous material in the Monte Carlo transport jargon. During the implementation of the geometry, we defined the components of the satellite as regions on which we requested the estimation of the quantities of interest for ABCS are:

1. All the regions define the SP components (see Table 5.1);
2. All the regions define the four cards and the filling air of the ABCS payload interior (see Figure 5.2);

We refer to those components as “target components” in the following.

Table 5.5 reports the list of estimators used in the present work with a brief recall of their main characteristics and scope. The 3rd column of Table 5.5 specifies which satellite components we choose to apply the estimators. For example, a track-length-based estimator [18] evaluates particle flux or flux-derived quantities (nuclear reaction rates, equivalent damages) averaged on one region volume. We also use a variant of the track length estimator to estimate the same quantity in a user-defined spatial mesh (see, for example, Figure 5.9) or in a matrix of user-defined geometrical regions.

Table 5.5 – list of the estimators used in the FLUKA simulations related to the present work

Estimator	Scored Quantity	Regions to score	Comment
Track length	SI1MEVNE Silicon 1 MeV Neutron Equivalent damage fluence (p/cm ² /primary)	Card 1 to 4 in ABCS payload and all the SP layers.	1 MeV Si equivalent damage fluence considers the equivalent damages induced in the material by each primary particle and their secondaries (See Chapter 4).
Mesh track length	TID on a user-defined spatial mesh (Gy/primary)	Whole satellite body	This modality allows the spatial visualization of the scored quantity (see Fig. 9), defining a spatial mesh independent of the geometry
	TID deposited in the region volume (Gy/primary)	All layers of the solar cell. Air and Card 1 to 4 in ABCS Payload	Primary particles and their secondaries deposit the dose score in each region's volume.

In column two of Table 5.5, the SI1MEVNE fluence and TID estimates have the units of particles/cm² and Gy per primary source particles, respectively. Consequently, we must rescale each response to its source’s intensities reported in Table 5.2, obtaining a dose rate (Gy/s) for TID and flux (particles/cm²/s) for SI1MEVNE. The overall estimated response R was finally obtained, summing up all the individual source term responses ($R = \sum_i R_i$) of the selected estimator.

We use TID and SI1MEVNE fluence estimates to evaluate the relative effectiveness of the shielding solution. Defining the shielding effectiveness η as

$$\eta = \frac{(R_2 - R_1)}{R_1} * 100; \quad \text{Equation 5.1}$$

R_2 is the overall estimator’s response after adopting the additive shielding solution, and R_1 is the overall estimator’s response to the configuration without such a shielding solution. Therefore, η quantifies the shielding effectiveness of configuration 2 relative to configuration 1. Negative values of the η indicate an increase in the shielding effectiveness; conversely, positive values indicate a decrease in the shielding effectiveness. Table 5.6 reports some TID rate estimations from FLUKA simulations with a trapped proton source term to clarify this point. Figure 5.10 can also help visualize the spatial distribution of the TID rates of the three considered configurations.

Table 5.6 – Estimated TID rate for card 4 in the progressive construction of the ABCS layout around the target components

Void configuration	NFS configuration	FS configuration
7.43E-04 Gy/s	1.02E-06 Gy/s	7.98E-07 Gy/s
Shielding effectiveness η relative to Void configuration	-99.86%	-99.89%
Shielding effectiveness η relative to the NFS configuration		-21.50%

The “Void” configuration is set to vacuum all the materials in the satellite model except for the ABCS payload air volume and the four cards. The “No-Further Shield” (NFS) configuration refers to the satellite layout without the additive shielding solution adopted to protect the primary payload further. Finally, the “Further Shield” (FS) configuration comprises the additive protection for the primary payload.

The TID rate data reported in the second row of Table 6 show a significant decrease in passing from the VOID to the NFS configuration. In contrast, the transition from NFS to the FS configuration decreases the TID rate slightly.

According to Equation 5, the third row of Table 6 reports the values of η for the NFS and FS configurations relative to the Void configuration: the satellite’s structure (NFS configuration) is responsible for the decreases in the TID rate of $\eta = -99.86\%$, whereas the FS configuration adds just a 0.03% of the TID rate decrease.

Since we are focused on the shielding effectiveness of the FS configuration, we decided to calculate its η relative to the NFS configuration, obtaining $\eta = -21.50\%$. Consequently, we adopt the NFS as a reference configuration for the calculation of η , having the advantage of starting from a more realistic configuration than the Void.

In the following, we compare the contributions to the overall TID and SI1MEVNE responses from the different source terms (see Tables 5.8, 5.10, 5.12). To avoid confusion, we use the shielding effectiveness in a different relation

$$\eta^* = \frac{(R_{FSi} - R_{NFSi})}{R_{NFS}} * 100; \quad \text{Equation 5.2}$$

where $R_{NFS} = \sum_i R_{NFSi}$ is the overall response of the estimator obtained as the sum of each considered source term for the NFS configuration and η^* is the shielding effectiveness due to the single source term relative to an overall response. Finally, we obtain the total shielding effectiveness as $\eta = \sum_i \eta_i^*$.

Results and discussion

TID rate estimation in ABCS Payload

Table 5.7 compares the overall TID rate and the shielding effectiveness η (see Equation 5.2) in the target components of the ABCS payload. Due to the source isotropy, both in the absence and in the presence of further shielding, the four Cards show very close dose rates.

The lower TID rates of the innermost Cards (2 and 3) are due to the shielding effects of Cards (1 and 4) in extreme positions. In all the considered cases, the η value is from -18% to -19.9% with AP8/AE8 dataset, and it decreases for the AP9/AE9 dataset in a range of values from -14.6% to 18.7%. In terms of absolute values, we observe that, on average, the AP9/AE9 dataset leads to a decrease of factor 3.4 in the dose rate.

Table 5.7 - Comparison of TID rates deposited in Air and PCB cards into the ABCS payload.

Payload	Overall Dose Rate with AP8/AE8			Overall Dose Rate with AP9/AE9		
	NFS configuration	FS configuration	η	NFS configuration	FS configuration	η
	Gy/s	Gy/s		Gy/s	Gy/s	
Air	1.44E-06	1.16E-06	-19.7%	4.03E-07	3.31E-07	-18.0%
CARD1	1.34E-06	1.10E-06	-17.7%	3.90E-07	3.28E-07	-15.9%
CARD2	1.25E-06	1.03E-06	-17.9%	3.77E-07	3.20E-07	-15.1%
CARD3	1.24E-06	1.02E-06	-17.7%	3.72E-07	3.17E-07	-14.6%
CARD4	1.35E-06	1.08E-06	-19.7%	3.90E-07	3.28E-07	-15.7%

Table 5.8 shows how the different evaluations of the trapped proton source term obtained from the AP8 and AP9 models change the repartition of the contribution to the overall TID rate of card 4. According to Figure 5.5b, AP8 foresee a more energetic spectrum than AP9 with total flux intensities of the same order of magnitude, resulting in a TID rate that is a factor 24-25 higher than one obtained from AP9. Consequently, the trapped proton delivered the most significant dose fraction when AP8 data were used in the simulation, followed by the SEP protons. Conversely, SEP protons are the dominant source term in the AP9 simulation. Concerning the trapped electron, examining the energetic spectra reported in Figure 5.5a, we found that the AE8 and AE9 differences are less than in the case of the trapped proton. Consequently, the higher TID rate observed with AP9 depends on higher total flux intensity than the spectral changes.

Table 5.8 - Comparison of the contribution to the TID rate in PCB Card 4.

Particle s	AP8/AE8					AP9/AE9				
	NFS configuration		FS configuration		η^*	NFS Configuration		FS configuration		η^*
	TID Rate (Gy/s)	Fraction of the total TID rate	TID Rate (Gy/s)	Fraction of the total TID rate		TID Rate (Gy/s) No shield	Fraction of the total TID rate	TID Rate (Gy/s) Shield	Fraction of the total TID rate	
Trap H	1.02E-06	75.60%	7.98E-07	73.80%	-16.47%	4.07E-08	10.45%	3.32E-08	10.10%	-1.92%
Trap E	3.19E-08	2.37%	1.69E-08	1.60%	-1.11%	5.30E-08	13.60%	2.85E-08	8.70%	-6.28%
GCR H	1.94E-08	1.44%	2.03E-08	1.90%	0.067%	1.94E-08	4.98%	2.03E-08	6.20%	0.23%
GCR He	5.34E-09	0.40%	5.50E-09	0.50%	0.012%	5.34E-09	1.37%	5.50E-09	1.70%	0.04%
CGR Fe	1.75E-09	0.13%	1.73E-09	0.20%	-0.001%	1.75E-09	0.45%	1.73E-09	0.50%	-0.01%
SEP H	2.68E-07	19.95%	2.38E-07	22.03%	-2.226%	2.68E-07	68.79%	2.38E-07	72.50%	-7.69%
SEP He	1.30E-09	0.10%	1.10E-09	0.10%	-0.015%	1.30E-09	0.33%	1.10E-09	0.34%	-0.05%
SEP O	7.54E-11	0.01%	6.25E-11	0.01%	-0.001%	7.54E-11	0.02%	6.25E-11	0.02%	-0.003%
Total	1.35E-06	100%	1.08E-06	100%	-19.75%	3.90E-07	100.00%	3.28E-07	100.00%	-15.69%

η^* is calculated according to Equation 5.2

GCR Hydrogen and Helium are the sole ions in Table 5.8 that cause an increase in their dose rate contributions in the presence of shielding. A possible explanation is the interaction of the high energy tails of the GCR ions with the shielding layers generating less energetic secondary particles having a higher probability of depositing energy into the payload target components. However, their contributions are too little to revert the overall shielding effectiveness in absolute terms.

Conversely, the ^{56}Fe ion contribution to the TID rate decreases when the shielding is present, suggesting that the secondaries born from the interactions with the shielding layers could have an asymmetric kinetic energy distribution: some still have enough energy to pass through the ABCS payload without interacting within its boundary, other exits from the fragmentation reaction with kinetic energy sufficiently lower to stop into the shielding layer. This mechanism will be clarified, addressing further work on simulations with higher statistics and event-by-event analysis.

SEP ions were shielded more efficiently than GCR because of their lower energy distributions. As in the case of GCR ions, SW ions of increasing Z were progressively shielded better: ^{16}O , the SEP heaviest ion considered in the simulation, has the more significant TID rate decrease in Card 4.

The examination of the bi-dimensional mapping of the dose rate spatial distribution obtained, superimposing their meshed responses to an x-y cross-section of the satellite's geometry (see Table 5.3, 2nd row), confirms the dose decreases quantified using the parameter η . Figure 5.10 shows that the dose decreases ($\eta = -19.52\%$) for trapped protons are apparent comparing the reported images.

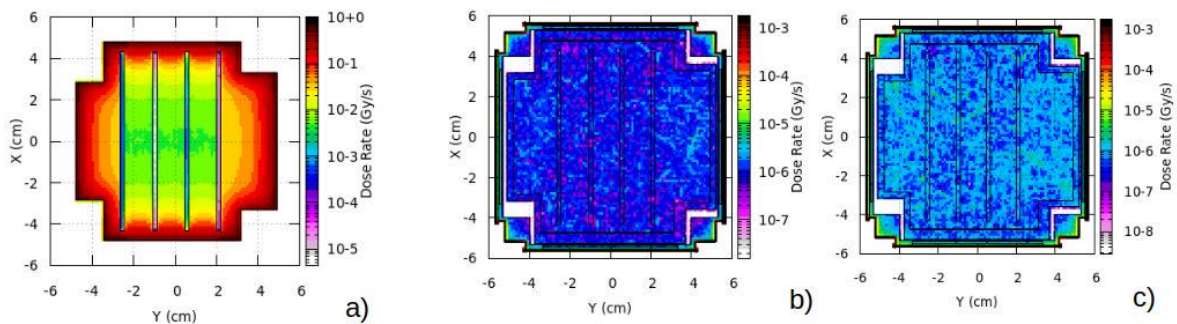


Figure 5.10 - The comparison of the trapped proton dose rate as obtained using AP8 data integrated along the Z-axis of the FLUKA reference system and reported on an X-Y cross-section of the satellite geometry: a) making void all the satellite components except the cards and the air in the payload; b) in the absence of the shielding; c) in the presence of the shielding. In adding the shielding (cases b to c), the TID rate decrease agrees with the target components' shielding effectiveness ($\eta = -19.52\%$).

Figure 5.11 compares the dose rate spatial distribution for the GCR proton ($\eta = +4.88\%$) with and without shielding. The images confirm that the dose increase when the shielding is present.

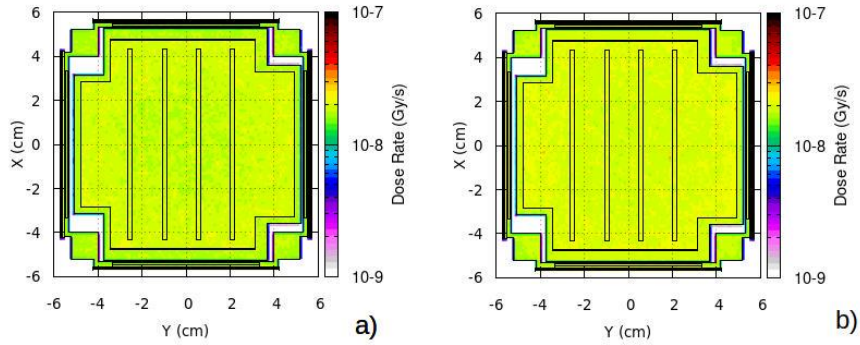


Figure 5.11: The comparison of the GCR proton dose rate integrated along the Z-axis of the FLUKA reference system and reported on an X-Y cross-section of the satellite geometry: a) in the absence of the shielding; b) in the presence of the shielding. The TID rate increase agrees with the target components' shielding effectiveness ($\eta = +4.88\%$).

The dose rate decreases for the ^{56}Fe ions contribution ($\eta = -1.30\%$) is confirmed by the dose rate mapping comparisons reported in Figure 5.12.

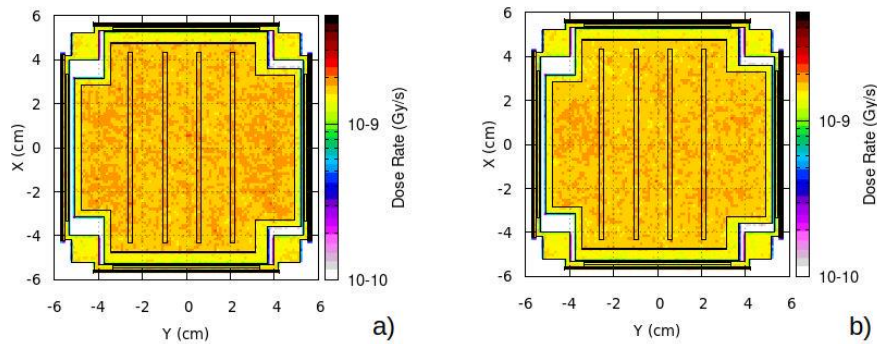


Figure 5.12 - The comparison of the GCR ^{56}Fe dose rate integrated along the Z-axis of the FLUKA reference system and reported on an X-Y cross-section of the satellite geometry: a) in the absence of the shielding; b) in the presence of the shielding. The TID rate decrease agrees with the target components' shielding effectiveness ($\eta = -1.30\%$).

Also, Figure 5.13, which compares the simulated dose rate spatial distributions for SEP protons, agrees with the decrease quantified by $\eta = -11.15\%$. The images also show anisotropies in the dose distribution induced by the four cards whose mutual shielding breaks the irradiation spherical symmetry, causing localized dose increases to each image's "left" and "right" sides.

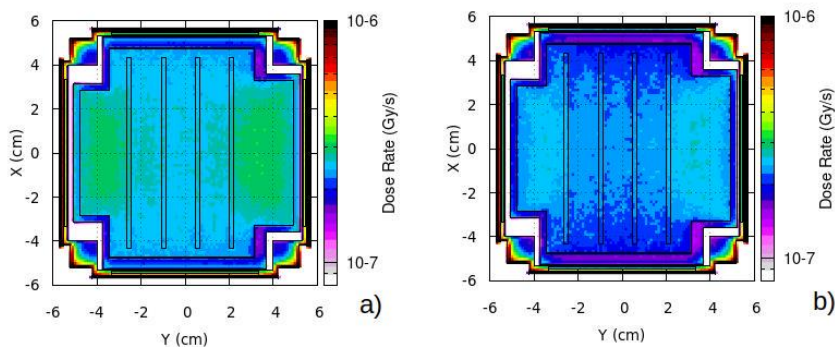


Figure 5.13 - The comparison of the SEP proton dose rate integrated along the Z-axis of the FLUKA reference system and reported on an X-Y cross-section of the satellite geometry: a) in the absence of the shielding; b) in the presence of the shielding. The dose rate decrease agrees with the target components' shielding effectiveness ($\eta = -11.15\%$).

TID rate and shielding effectiveness estimations in the Solar Panels

It is apparent that the SPs are the outermost components of the satellite and have a direct and unshielded exposition to the orbital radiation source. As expected, the data reported in Table 5.9 shows that the FS configuration has no impact on the TID rate on SP components. Due to the progressively increasing shielding offered by the outer layers to the inner ones, a monotonic TID rate decrease is always present in NFS and FS configurations. In agreement with the null values of η reported in Table 5.9, the dose rate distribution in SPs (Figures 5.10 to 5.13) remains unaltered.

Table 5.9 - TID rate deposited into the solar cell components.

Solar Cell component	TID Dose Rate (AP8/AE8)			TID Dose Rate (AP9/AE9)		
	NFS	FS	η	NFS	FS	η
	Gy/s	Gy/s		Gy/s	Gy/s	
Anti-Reflex, SiO ₂	3.79E-01	3.79E-01	0.0%	6.76E-01	6.76E-01	0.0%
Top Cell, In Ga P (N/P)	1.71E-02	1.71E-02	0.0%	1.62E-02	1.62E-02	0.0%
Middle Cell, GaAs(N/P)	4.51E-03	4.51E-03	0.0%	3.42E-03	3.42E-03	0.0%
Bottom Cell, Ge	2.34E-03	2.34E-03	0.0%	1.64E-03	1.64E-03	0.0%
Substrate, Ge(P)	1.09E-03	1.09E-03	0.0%	7.73E-04	7.73E-04	0.0%
Contact Layer, Ag	3.85E-04	3.85E-04	0.0%	3.21E-04	3.21E-04	0.0%

Table 5.10 shows the contribution of each source term to the TID rate in the SP's Middle Cell. The FS solution does not affect the trapped particles ($\eta=0.00\%$) and increases the dose rate from SEP ¹⁶O ($\eta=0.57\%$), GCR He ($\eta=2.80\%$), and GCR H ($\eta=4.88\%$). Also, it causes minor dose rate decreases of the other SEP and GCR ions. Again, those dose rate contributions are negligible compared to one of the trapped particles, leaving the TID rate unaltered. Furthermore, the limited shielding offered from the outermost layers of the SP to the Middle cell does not enhance the spectral differences between the A8 and A9 models for the trapped particles maintaining their contributions to the overall TID rate dominant on the other ions.

Table 5.10 - Comparison of the contribution of each source term to the TID rate in the Middle Cell, GaAs(N/P)

Particles	TID Dose Rate (AP8/AE8)					TID Dose Rate (AP9/AE9)				
	Flux (Gy/s) NFS	Fraction of the total TID rate	Flux (Gy/s) FS	Fraction of the total TID rate	η^*	Flux (Gy/s) NFS	Fraction of the total TID rate	Flux (Gy/s) FS	Fraction of the total TID rate	η^*
Trap H	2.88E-03	63.89%	2.88E-03	63.90%	0.00%	7.78E-04	22.73%	7.78E-04	22.73%	0.00%
Trap E	1.63E-03	36.04%	1.63E-03	36.04%	0.00%	2.64E-03	77.19%	2.64E-03	77.19%	0.00%
GCR H	1.94E-08	0.00%	2.03E-08	0.00%	2E-05%	1.94E-08	0.00%	2.03E-08	0.00%	3E-05%
GCR He	3.67E-09	0.00%	3.78E-09	0.00%	2E-06%	3.67E-09	0.00%	3.78E-09	0.00%	3E-06%
CGR Fe	1.38E-09	0.00%	1.37E-09	0.00%	-2E-07%	1.38E-09	0.00%	1.37E-09	0.00%	-3E-07%
SEP H	2.70E-06	0.06%	2.70E-06	0.06%	0.00%	2.70E-06	0.06%	2.70E-06	0.08%	0.00%
SEP He	1.41E-07	0.00%	1.41E-07	0.00%	0.00%	1.41E-07	0.00%	1.41E-07	0.00%	0.00%
SEP O	1.74E-08	0.00%	1.74E-08	0.00%	0.00%	1.74E-08	0.00%	1.74E-08	0.00%	0.00%
Total	4.51E-03	100%	4.51E-03	100%	0.00%	3.42E-03	100%	3.42E-03	100%	0.00%

η^* is calculated according to Equation 5.2

The Silicon 1 MeV neutron equivalent fluxes in the ABCS target components

The SI1MEVNE flux is a quantity that allows the comparison of the damages induced during irradiation by different kinds of particles. In the present paper, we use this quantity to estimate the damage level in the ABCS target component in the irradiation orbital condition and compare the responses from simulated neutron irradiation of the whole satellite within the TCC of the TAPIRO reactor. In the following discussion, we refer to the simulations carried out with the orbital source as ABCS simulations and name the others as TAPIRO simulations.

Table 5.11 compares the SI1MEVNE fluxes estimations of Card 4 in the ABCS simulation with those obtained in the TAPIRO's simulations. Using the A8 data for trapped particles leads to equivalent flux damage higher of factor 2.8 - 3.1 than the one obtained with A9 with a decrease of the shielding effectiveness -15.66% to -6.86%. This finding is aligned with the already discussed spectral change for the trapped particles introduced by the A8/A9 models.

Because of the poor shielding effectiveness against neutrons ($\eta = -3.36\%$) penetrating more in the shielding designed for the charged particles, the predicted TAPIRO SI1MEVNE flux outperforms the flux of the orbital ABCS simulations. We observe that, according to the AP8/AE8 models, the equivalent fluence received by Card 4 in a two-year exposition to the orbital source is realized in a 47 minutes neutron irradiation in the TCC using a nuclear power of just 50 W (the 1% of the 5kW maximum nuclear power of TAPIRO).

Table 5.11 – Comparison of the SI1MEVNE fluxes in Card 4

TAPIRO Simulation			ABCS Simulation (AP8/AE8)			ABCS Simulation (AP9/AE9)		
NFS (n/cm2/s/kW)	FS (n/cm2/s/Kw)	η	FS (p/cm2/s)	FS (p/cm2/s)	η	NFS (p/cm2/s)	FS (p/cm2/s)	η
4.05E+08	3.89E+08	-3.36%	1.05E+03	9.02E+02	-14.05%	3.09E+02	2.87E+02	-6.85%

Table 5.12 reports the contribution of each orbital source term to the overall SI1MEVNE flux, showing a trend like the one obtained for the TID rate (See Table 5.8). With AP8, the trapped protons are responsible for the more significant fraction of silicon equivalent damages, followed by SEP and GCR proton. The A9 model shows the more significant contribution is from the SEP proton followed by trapped and GCR proton. The shielding effectiveness is higher for trapped particles causing a decrease in their equivalent damages, whereas GCR ions show a positive shielding effect increasing their contribution. The trend is more marked for the A9 data, where the contribution of the trapped proton to the equivalent damage is reduced.

Table 5.12 - Contribution of each source term to SI1MEVNE flux in card 4 of the ABCS payload

Particles	ABCS Simulation (AP8/AE8)					ABCS Simulation (AP9/AE9)				
	Flux (p/cm2/s] NFS	Worth %	Flux (p/cm2/s) FS	Worth %	η^*	Flux (p/cm2/s] FS	Worth %	Flux (p/cm2/s) FS	Worth %	η^*
Trap H	7.77E+02	74.17%	6.44E+02	71.03%	-12.67%	3.50E+01	11.34%	2.83E+01	9.85%	-2.168%
Trap E	2.18E-01	0.02%	7.89E-02	0.01%	-0.01%	3.04E-01	0.10%	1.00E-01	0.03%	-0.066%
GCR H	3.37E+01	3.17%	3.85E+01	4.31%	0.46%	3.36E+01	10.89%	3.85E+01	13.40%	1.586%
GCR He	4.27E+00	0.40%	5.11E+00	0.57%	0.08%	4.27E+00	1.38%	5.11E+00	1.78%	0.272%
CGR Fe	1.08E-01	0.01%	1.29E-01	0.01%	0.002%	1.08E-01	0.04%	1.30E-01	0.05%	0.007%
SEP H	2.35E+02	22.20%	2.15E+02	24.05%	-1.90%	2.35E+02	76.20%	2.15E+02	74.82%	-6.472%
SEP He	2.38E-01	0.02%	2.25E-01	0.03%	-0.00124%	2.40E-01	0.10%	2.26E-01	0.08%	-0.005%
SEP O	3.66E-03	0.00%	3.82E-03	0.00%	0.00002%	3.86E-03	0.00%	3.84E-03	0.00%	-1E-05%
Total	1.05E+03	100%	9.02E+02	100%	-14.05%	3.09E+02	100%	2.87E+02	100%	-6.85%

η^* is calculated according to Equation 5.2

Table 5.13 reports the SI1MEVNE fluxes in SP's regions for both ABCS and TAPIRO simulations. In the orbital irradiation condition, being SPs located in the outermost positions outside the shielding protection, the SI1MEVNE fluxes remain practically unchanged with and without shielding. In addition, we observe a progressive decrease in flux intensity from the outermost to the innermost solar panel regions by three orders of magnitude. Both A8 and A9 data confirm this trend. However, according to their spectral and intensity differences, the starting equivalent flux in the Anti-Reflex layer for the A9 is 1.5 higher than in the A8. Accordingly, the A9 equivalent fluxes in the subsequent layers decrease more rapidly than in the A8 series. Conversely, the SI1MEVNE fluxes estimates for the TAPIRO simulations show an almost constant damage flux that can be ascribed to the different mechanisms of transport and interaction of neutrons in the matter to one of the charged particles.

Table 5.13 – Comparison of the SI1MEVNE fluxes in Solar Panel obtained with the orbital source term and with the neutron spectrum of the TAPIRO's irradiation position RC1 channel and thermal column

Regions	TAPIRO Simulation			ABCS Simulation (AP8/AE8)			ABCS Simulation (AP9/AE9)		
	NFS (n/cm ² /s/kW)	FS (n/cm ² /s/kW)	η	NFS (p/cm ² /s)	FS (p/cm ² /s)	η	NFS (p/cm ² /s)	FS (p/cm ² /s)	η
Anti-Reflex, SiO ₂	5.75E+08	5.73E+08	-0.31%	1.47E+08	1.47E+08	0.0%	2.17E+08	2.17E+08	0.0%
Top Cell, In Ga P (N/P)	5.75E+08	5.74E+08	-0.11%	1.57E+07	1.57E+07	0.0%	9.92E+06	9.92E+06	0.0%
Middle Cell, GaAs(N/P)	5.74E+08	5.76E+08	0.30%	3.65E+06	3.65E+06	0.0%	1.01E+06	1.01E+06	0.0%
Bottom Cell, Ge	5.74E+08	5.73E+08	-0.24%	1.97E+06	1.97E+06	0.0%	4.58E+05	4.59E+05	0.0%
Substrate, Ge(P)	5.75E+08	5.72E+08	-0.48%	9.37E+05	9.37E+05	0.0%	1.91E+05	1.91E+05	0.0%
contact Layer, Ag	5.73E+08	5.71E+08	-0.27%	5.25E+05	5.25E+05	0.0%	9.82E+04	9.83E+04	0.0%

From Table 5.13, a TAPIRO irradiation of 1.5 hours in TCC at the power of 5 kW corresponds to 30 hours of exposure of the anti-reflex layer (the outermost SPs component) to the orbital source. In the same condition, the SP contact layer (the innermost SP component) receives a fluence equivalent to 8429 hours of exposure to the orbital source.

Comparisons of the FLUKA estimates of the dose rate with the ABCS onboard radFET reading

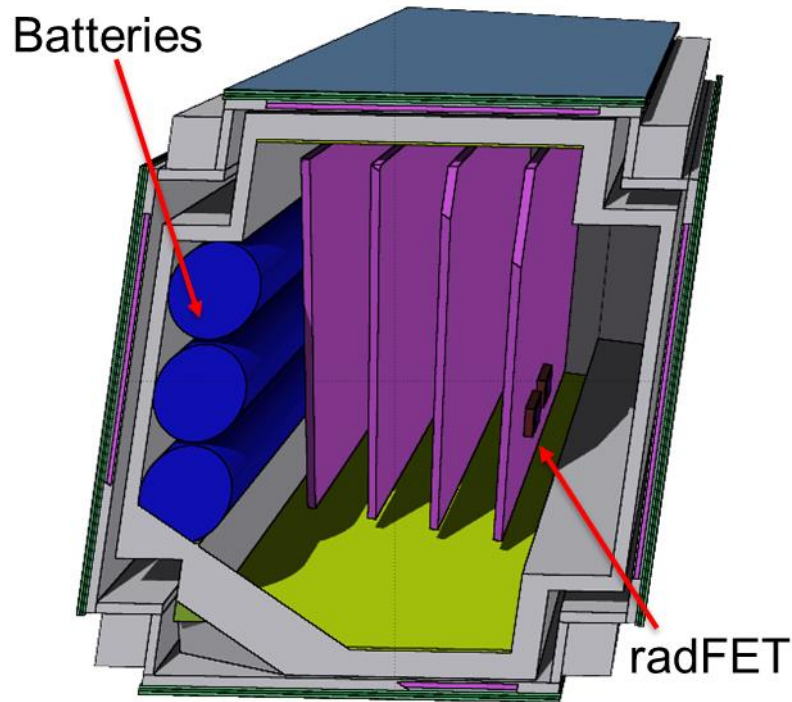


Figure 5.13 – A 3D view of the ABCS payload shows the location of batteries and radFET.

A new set of simulations to estimate the dose-response has been carried out one month before the launch of the satellite in July 2022. As reported in Figure 5.14, the upgraded ABCS geometry in which a six-battery pack and a radFET dose monitor have been added. The motivation for the battery pack implementation is that we are looking for absolute results to compare with experimentally measured quantities in the present simulation set. Whereas in the previous simulations, we estimate the effectiveness of the proposed shielding solution relative to a reference orbital irradiation condition. As shown in Table 5.6, the shielding solution and the then implemented structural materials shield 99.88% of the external radiation, which was quite enough to design a reliable and conservative solution. Furthermore, at the design time, we did not have any specifications about the battery pack composition, so we renounced to implement it.

Table 5.14 – Resume of the simulation present set on radFET dose in the ABCS payload

SOURCE	Tot Core	NPS per core	NPS	calculation time (hours)
Trapped proton	432	5.00E+08	2.16E+11	9.43
Trapped electron	288	7.00E+08	2.02E+11	9.00
GCR H	288	5.00E+07	1.44E+10	12.72
GCR ⁴ He	288	1.50E+07	4.32E+09	11.04
GCR ⁵⁶ Fe	432	1.00E+05	4.32E+07	12.40
SEF-H	288	2.00E+08	5.76E+10	10.65

The simulations have been carried out using the previously employed AE8/AP8-derived source terms to test the radiation shielding effectiveness. The scored quantities are TIDs in the

batteries, Card 4, Si substrate of the radFET from the particle fluxes of primary and secondary particles (Proton, Heavy Ion, Electron, γ photon, Helium-4 (α), neutrons).

As reported in Table 5.14, to achieve a meaningful score, the struggling step size of the charged particles has been reduced to correctly evaluate the energy deposited into the Si substrate of the radFET, and the number of the total sample particles significantly increased, resulting in computing times that range between 9-13 hours.

Examining the TID rate of Table 5.15, we found that card 4 is re-estimated to 4.66 rad/day with a decrease of 48% compared to the previously reported value of 7.02 rad/day (Table 5.7, AP8/AE8, FS configuration). The decrease is due to the additive shielding of the battery pack. The dose rate for one battery is 0.41 rad/day. Finally, the radFET Si substrate's dose rate is 1.59 rad/day without SEP. An eventual SEP emission leads to a dose rate increase between 22% – 32%, depending on the considered region.

Table 5.15 – TID rate obtained in the ABCS payload

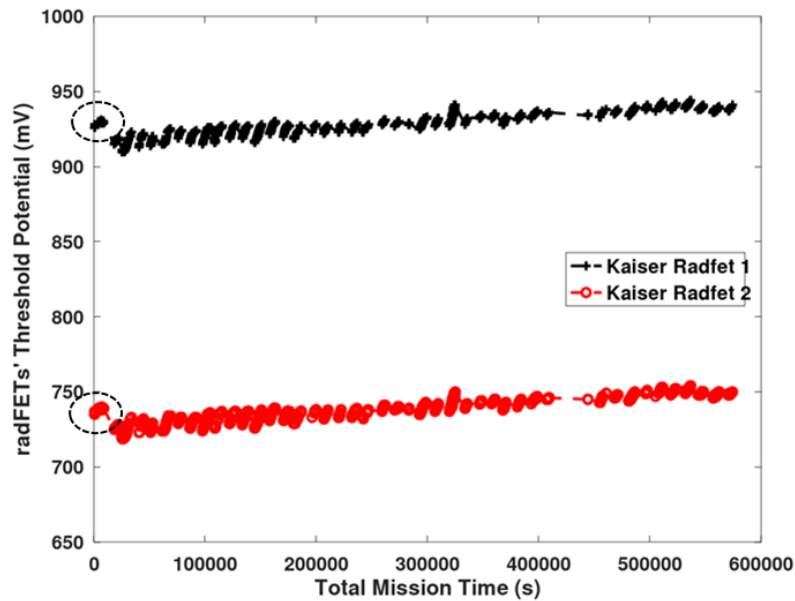
Radiation Source term	TID in Card 4			TID in Battery 1			TID in Si 0		
	(rad/day)	%	% with SEP	(rad/day)	%	% with SEP	(rad/day)	%	% with SEP
Trapped proton	3.44E+00	94.97%	73.80%	3.21E-01	77.68%	56.87%	1.43	90.10%	67.72%
Trapped Electron	7.63E-02	2.11%	1.64%	4.47E-02	10.82%	7.92%	0.06	3.96%	3.90%
GCR-H	9.78E-02	2.70%	2.10%	3.65E-02	8.83%	6.47%	0.07	4.49%	4.43%
GCR-He	2.62E-05	0.0007%	0.0006%	9.02E-03	2.18%	1.60%	0.02	1.15%	1.13%
GCR-Fe	7.88E-03	0.22%	0.17%	1.98E-03	0.48%	0.35%	0.00	0.31%	0.31%
SEP-H	1.04E+00		22.29%	1.51E-01		26.79%	0.53		32.59%
Total	3.62E+00			4.13E-01			1.59		
Total with SEP	4.66E+00			5.64E-01			2.11		

The VT-02 radFET has two active volumes that produce distinct V_{th} readouts. Onboard the satellite, the V_{th} measurements should be performed by supplying a drain current of 20 μ A to the circuit. This drain current value ensured a negligible temperature effect. It guaranteed the stability V_{th} a monotonic increase proportional to the integral dose progressively delivered by the radiation field within the payload.

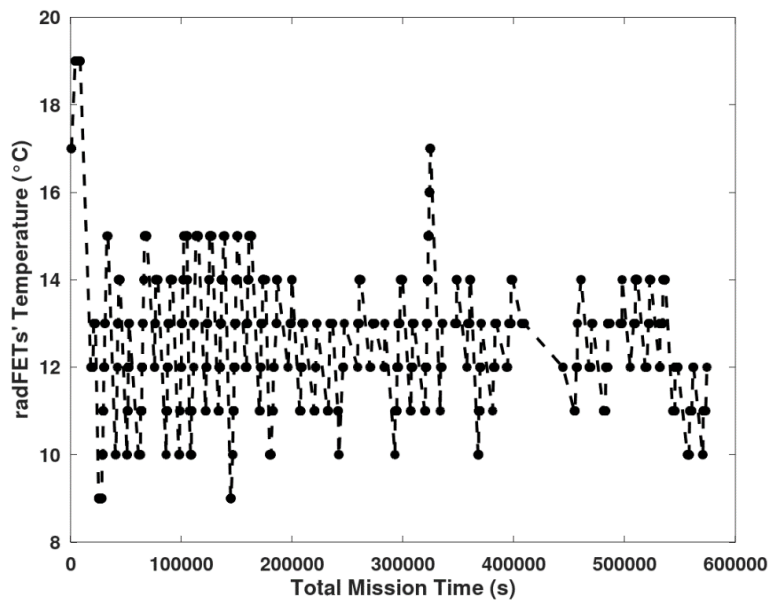
Figure 5.14a reports the measured doses registered in the function of the mission elapsed times. Figure 5.14b reports the same plot for the temperature sensor reading located in the proximity of the radFET. Examining the telemetric data of the first week of the ABCS mission, it is possible to monitor the integrated dose accumulation with time registered by the onboard radFET, and temperatures within the payload were transmitted to ground controls three times a day.

Observing the V_{th} trend in both signals of Figure 5.14a, the expected overall dose increases with time are verified. However, after the first six hours (the data enclosed within circles in Figure 5.14a), we observe a sudden decrease in the V_{th} values of both radFETs. Then there was a reprise of the integrated dose increases for the whole elapsed time, ending in a maximum value higher than the first reading.

Finally, observing Figure 5.14.b, which reports the temperature within the payload in a point close to the radFET, it is apparent that both the first voltage drop at six hours and the subsequent short time scale oscillations seems to be correlated with temperature changes. Such V_{th} time behaviour could indicate a decrease of the drain current from its ideal value of $20 \mu A$, leaving the V_{th} values sensitive to temperature change. Investigations are in progress to ascertain the possible causes of the drain current decrease after the mission's first six hours.



a)



b)

Figure 5.14 – a) Time series of the V_{th} during the first seven days of the mission. The black circles show the V_{th} s decrease after six hours from the mission beginning; b) the temperature time series shows the correlation with the sudden V_{th} decrease at six hours and the subsequent correlation with the V_{th} oscillations in the remaining part of the plot. The possible explanation for the initial drop and subsequent V_{th} oscillations is a drain current decrease that makes the V_{th} readout more sensitive to temperature change (see text).

The dose rate increase derived from the raw data is of 3.20 and 3.06 rad/day, respectively, for radFET1 and radFET2, which are higher than the simulations result (Table 5.15) of 1.59 rad/day and 2.11 rad/day (in the presence of SEP) but not entirely in disagreement.

Being the ABCS launch executed during a year of intense solar activity in which the trapped particles' source intensity substantially deviated from the one inferred by the SPENVIS model, the comparison must be considered preliminary since the post-mission analysis is underway, and a new temperature-corrected dataset will be furnished to allow further comparison and eventually recalibrate the MC simulations.

Conclusion and Future work.

Using the SPENVIS and FLUKA codes is possible to model the satellite's layout and estimate the quantities relevant for the analysis of the radiometric behaviour of the various satellite components with acceptable computational time, encouraging us to develop a modelling methodology that can be included in the concurrent design of future missions.

The separation strategy in different source terms of the Van Allen radiation environment adopted in the present work simplifies the TID and SI1MEVNE estimations. According to the A8 model, the subsequent analysis of each source term shows the trapped particles' prominent role in delivering dose and damages. In contrast, the data from the A9 mitigates the effect of the trapped particles, reducing the overall radiometric impact and increasing the relative role of SEP and GCR.

However, to remain conservative, we decided to adopt the worst scenario furnished by the A8 model for our critical mission review.

Considering the mission's mass budget, a shielding solution of the weight of 300 g constituted by subsequent layers of tungsten, resins, and aluminium located in an area to protect the primary payload (FS configuration) decreases the 20% overall dose rate to the target components in relative to the NFS configuration. Therefore, we renounce the search for a more effective shielding layout because preliminary simulations show us that a decrease of 50%-60% of the dose rate could be attained only by increasing the shield weight to 1 kg, which is entirely unacceptable.

The FS solution is effective for trapped and SEP particles but not for GCR particles whose higher emission energy could still induce Single Event Effects (SEE) to the onboard electronics.

Due to their external position, the SPs are exposed to irradiation without any possibility of the shield receiving an overall dose rate of 2 to 5 orders of magnitude higher than those experimented with within the ABCS payload.

The calculation methodology could be easily extended in the future to other quantities, such as Displacement Per Atoms (DPA), Non-Ionizing Energy Losses (NIEL), and SEE [44], allowing, a more specific implementation of the onboard electronic components, the correlation between irradiation and components availability during missions.

The roadmap to validate the methodology requires a comparison of the simulation outcomes with new experiments carried out at least with protons of relatively high energy (30-70 MeV) and electrons from the accelerator's beams.

The comparisons of the simulation results between the TAPIRO-TCC and orbital irradiations show that TAPIRO outperforms the orbital source in the Silicon 1 MeV equivalent damage flux. This finding is supported by the agreement between the measured neutron energy spectrum in TAPIRO's RC1 and the simulated one.

Obviously, to ascertain the goodness of the simulation results and the facility representativeness limits, careful comparison with the radiometric data obtained during the mission will be mandatory.

The presented results demonstrated how the simulations skills in the radiation transport are central for the aerospace mission design for the near-heart mission, like ABCS, dedicated to exploring zones with relatively high radioactive levels, like the Van Allen Belts.

Future works on the topics will focus on carefully revising the data obtained during the ABCS mission and probably the execution of a new set of simulations with a radiative source close to the orbital condition of the period.

Future work will be addressed in designing an experimental campaign conducted in the TAPIRO's TCC, where it is possible to irradiate CubeSat units while in operation. The first set of parallel irradiation tests to be executed on the TAPIRO reactor and the TOP-INPLART [59] proton accelerator, respectively located in the ENEA research centres of Casaccia and Frascati, are under design. The experiments foresee the irradiation of 1 CubeSat dummy unit with neutrons and protons to verify the damage induced at the same level of Silicon 1 MeV equivalent fluence according to the simulation findings reported in Chapter 5.

Another exciting project could be the launch of a feasibility study to realise a heavy ion accelerator that regionally could integrate the ASIF network for the irradiation test. ENEA and Sapienza University could entirely manage this activity in its initial stage.

The present application has been limited to CubeSat, a small and cheap satellite class used for concept demonstration, personnel training, and scientific application. However, it can be extended to more ambitious scientific or commercial projects integrating several kinds of resources whose discussion is beyond the scope of this thesis.

References

- [1] <https://www.cost.eu/publications/developing-the-scientific-basis-for-monitoring-modelling-and-predicting-space-weather/> visited 06/10/2022.
- [2] <https://timeline.web.cern.ch/victor-hess-discovers-cosmic-rays-0> visited 06/10/2022
- [3] SPENVIS - Space Environment, Effects, and Education System <https://www.spennis.oma.be> visited 06/10/2022
- [4] John E. Beckman, and Terence J. Mahoney, "The Maunder Minimum and Climate Change: Have Historical Records Aided Current Research ?", Library and Information Services in Astronomy III ASP Conference Series, Vol. 153, 1998 U. Grothkopf, H. Andernach, S. Stevens-Rayburn, and M. Gomez (Copyright 1998 Astronomical Society of the Pacific. All rights reserved. ds.)
- [5] The Victoria Advocate -28 dic. 1958
<https://news.google.com/newspapers?id=kCxQAAAAIBAJ&sjid=HVYDAAAAIBAJ&pg=3307%2C5547467> visited 06/10/2022.
- [6] DONALD V. REAMES "The Two Sources of Solar Energetic Particles" ", Space Sci. Rev. 175, 53, 2013.
<https://doi.org/10.1007/s11214-013-9958-9>
- [7] Bird, D. J.; Corbato, S. C.; Dai, H. Y.; Elbert, J. W.; Green, K. D.; Huang, M. A.; Kieda, D. B.; Ko, S.; Larsen, C. G.; Loh, E. C.; Luo, M. Z.; Salamon, M. H.; Smith, J. D.; Sokolsky, P.; Sommers, P.; Tang, J. K. K.; Thomas, S. B. "Detection of a Cosmic Ray with Measured Energy Well beyond the Expected Spectral Cutoff due to Cosmic Microwave Radiation", Astrophysical Journal v.441, p.144.
https://ui.adsabs.harvard.edu/link_gateway/1995ApJ...441..144B/doi:10.1086/175344
- [8] W.R. Binns, M.E. Wiedenbeck, M. Arnould, A.C. Cummings, G.A. de Nolfo, S. Goriely, M.H. Israel, R.A. Leske, R.A. Mewaldt, E.C. Stone, T.T. von Rosenvinge, "The OB association origin of galactic cosmic rays" New Astronomy Reviews 52 (2008) 427–430.
- [9] E. Fermi, "On the Origin of the Cosmic Radiation", Physical Review Vol. 75, N8, APRIL 15, 1949.
- [10] M. Amenomori et al. "Anisotropy and Corotation of Galactic Cosmic Rays", SCIENCE VOL 314 20 OCTOBER 2006, doi:10.1126/science.1131702.
- [11] Masayuki Naito, Nobuyuki Hasebe, Mana Shikishima, Yoshiharu Amano, Junichi Haruyama, Jose A Matias-Lopes, Kyeong Ja Kim and Satoshi Kodaira, "Radiation dose and its protection in the Moon from galactic cosmic rays and solar energetic particles: at the lunar surface and in a lava tube" J. Radiol. Prot. 40 (2020) 947–961 (15pp). <https://doi.org/10.1088/1361-6498/abb120>.
- [12] Daniel Matthia, Thomas Berger, Alankrita I. Mrigakshi, Gunther Reitz, "A ready-to-use galactic cosmic ray model", Advances in Space Research Volume 51, Issue 3, 1 February 2013, Pages 329-338.
- [13] G. D. Badhwar and P. M. O'Neill, "LONG-TERM MODULATION OF GALACTIC COSMIC RADIATION AND ITS MODEL FOR SPACE EXPLORATION", Adv. Space Res. Vol. 14, No. 10, pp. (10)749-(10)757, 1994.
- [14] GNU Octave <https://octave.org/> visited 07/10/2022.
- [15] <https://essr.esa.int/project/iso15390-galactic-cosmic-ray-model-fortran-implementation> visited 06/10/2022.
- [16] <http://www.nasonline.org/member-directory/deceased-members/49583.html> visited 06/10/2022.
- [17] M.S. Gordon, P. Goldhagen, K.P. Rodbell, T.H. Zabel, H.H.K. Tang, J.M. Clem, P. Bailey, "Measurement of the flux and energy spectrum of cosmic-ray induced neutrons on the ground", IEEE Trans. Nucl. Sci. (2004). <https://doi.org/10.1109/TNS.2004.839134>
- [18] "Introduction to the Monte Carlo simulation of radiation transport", Beginner online training, Spring 2020 https://indico.cern.ch/event/1012211/contributions/4247770/attachments/2254500/3825142/02_Introduction_to_Monte_Carlo_2021_online.pdf accessed December 29 2021.
- [19] F. Iannone et al., International Conference on High-Performance Computing & Simulation (HPCS), Dublin, Ireland, 2019, pp. 1051-1052, <https://doi.org/10.1109/HPCS48598.2019.9188135>
- [20] Luo Zheng-Ming and Anders Brahme, " AN OVERVIEW OF THE TRANSPORT THEORY OF CHARGED PARTICLES", Radial. Phys. Chem. Vol. 41, No. 4/5, pp. 673—703, 1993.
- [21] M. Cavinato, E. Fabrici, E. Gadioli 1, E. Gadioli Erba, E. Risi, "Boltzmann master equation theory of angular distributions in heavy-ion reactions", Nuclear Physics A 643 (1998) 15-29.
- [22] <https://fluka.cern> visited 07/10/2022.

- [23] G. Battistoni, T. Boehlen, F. Cerutti, P.W. Chin, L.S. Esposito, A. Fassò, A. Ferrari, A. Lechner, A. Empl, A. Mairani, A. Mereghetti, P. Garcia Ortega, J. Ranft, S. Roesler, P.R. Sala, V. Vlachoudis, G. Smirnov, "Overview of the FLUKA code", *Annals of Nuclear Energy* 82, 10-18 (2015).
- [24] C. Ahdida, D. Bozzato, D. Calzolari, F. Cerutti, N. Charitonidis, A. Cimmino, A. Coronetti, G. L. D'Alessandro, A. Donadon Servalles, L. S. Esposito, R. Froeschl, R. García Alía, A. Gerbershagen, S. Gilardoni, D. Horváth, G. Hugo, A. Infantino, V. Kouskoura, A. Lechner, B. Lefebvre, G. Lerner, M. Magistris, A. Manousos, G. Moryc, F. Ogallar Ruiz, F. Pozzi, D. Prelicpean, S. Roesler, R. Rossi, M. Sabaté Gilarte, F. Salvat Pujol, P. Schoofs, V. Stránský, C. Theis, A. Tsinganis, R. Versaci, V. Vlachoudis, A. Waets, M. Widorski, "*New Capabilities of the FLUKA Multi-Purpose Code*", *Frontiers in Physics* 9, 788253 (2022).
- [25] V. Vlachoudis "FLAIR: A Powerful But User-Friendly Graphical Interface For FLUKA" Proc. Int. Conf. on Mathematics, Computational Methods & Reactor Physics (M&C 2009), Saratoga Springs, New York, 2009
- [26] MCNP version 6.2 (Release Notes) https://mcnp.lanl.gov/pdf_files/la-ur-18-20808.pdf, visited December 29 2021
- [27] Matsumoto, M.; Nishimura, T., "Mersenne twister: a 623-dimensionally equidistributed uniform pseudo-random number generator", *ACM Transactions on Modeling and Computer Simulation*. 8 (1): 3–30. doi:10.1145/272991.272995.
- [28] Knuth, Donald (1997). *Seminumerical Algorithms, The Art of Computer Programming, Vol. 2 (3rd ed.)*, Reading, MA: Addison-Wesley Professional. pp. 10–26.
- [29] https://www.enea.it/it/Ricerca_sviluppo/documenti/nucleare/TRIGA.pdf visited 07/10/2022.
- [30] G.S. Was, "Fundamentals of radiation material science", pp 4-12 Springer ISBN 978-1-4939-3436-2.
- [31] D. Vrajitoru "Parallel and Distributed Programming"
https://www.cs.iusb.edu/~danav/teach/b424/b424_23_embpar.html accessed December 29 2021
- [32] N.Burgio, L.Cretara, M.Frullini, A.Gandini, V.Peluso, A.Santagata, Nuclear Engineering and Design, (2014) <http://dx.doi.org/10.1016/j.nucengdes.2014.03.040>
- [33] M. Ciotti, "Utilizzo del reattore TAPIRO a supporto dello sviluppo dei sistemi LFR"
www.enea.it/it/Ricerca_sviluppo/energia/ricerca-di-sistema-elettrico/accordo-di-programma-mise-enea-2012-2014/produzione-di-energia-elettrica-e-protezione-dellambiente/documenti/ricerca-di-sistema-elettrico/nucleare-iv-gen/2012/rds-2013-016.pdf, pag 9. accessed 29 December 2021
- [34] "Development of a target system for the production of beta-emitting radioisotopes with small size cyclotrons", S. Buono, N. Burgio, L. Maciocco, R. Rocca, 11th Workshop on Targetry and Target Chemistry, Robinson College, University of Cambridge, 28th to 31st August 2006.
- [35] "DESIGN AND TEST OF AN ACCELERATOR DRIVEN NEUTRON ACTIVATOR AT THE JRC CYCLOTRON OF THE EUROPEAN COMMISSION" N. Burgio et al., *Cyclotrons and Their Applications 2007*, Eighteenth International Conference.
- [36] "Development of an accelerator-driven neutron activator for medical radioisotope production", N. Burgio et al. *Nuclear Instruments and Methods in Physics Research Section A Accelerators Spectrometers Detectors and Associated Equipment* 601(3):223-228 April 2009.
- [37] N. Burgio, L. Cretara, M. Corcione, M. Frullini, L. Iannascoli, A. Nascetti, A. Santagata, G. Palmerini, A. Quintino, J. R. Brucato, A. Meneghin, D. Paglialunga, "Modelling the interaction of the Astro Bio Cube Sat with the Van Allen's Belt radiative field using Monte Carlo transport codes", *Radiation Detection Technology and Methods*, <https://doi.org/10.1007/s41605-022-00321-9>.
- [38] M.S. Gordon ; P. Goldhagen ; K.P. Rodbell ; T.H. Zabel ; H.H.K. Tang ; J.M. Clem ; P. Bailey "Measurement of the flux and energy spectrum of cosmic-ray induced neutrons on the ground" *IEEE Transactions on Nuclear Science* (Volume: 51, Issue: 6, Dec. 2004).
- [39] Claudio Cipriani " A PROCEDURE TO ESTIMATE EARTH ATMOSPHERIC NEUTRON FLUXES USING FLUKA CODE", Master Thesis - Facoltà di Ingegneria Civile e Industriale (Tecnologie Nucleari). Tutors Prof. Massimo Frullini, Dr N. Burgio, Dr Luca Cretara AA 2019/2020.
- [40] <https://www.geomagsphere.org/index.php/vertical-rigidity-cutoff> visited 07/10/2022

- [41] Roesler S., Engel R., Ranft J. (2001) The Monte Carlo Event Generator DPMJET-III. In: Kling A., Barão F.J.C., Nakagawa M., Távora L., Vaz P. (eds) *Advanced Monte Carlo for Radiation Physics, Particle Transport Simulation and Applications*. Springer, Berlin, Heidelberg. https://doi.org/10.1007/978-3-642-18211-2_166
- [42] C. M. Hung and E. Shuryak, "Equation of state, radial flow, and freeze-out in high energy heavy ion collisions", *Phys. Rev. C* **57**, 1891.
- [43] Scoring and Biasing | The official CERN FLUKA website visited on 07/10/2022.
- [44] Kenneth A. LaBel, Michele M. Gates, Janet L. Barth, "Single Event Effect Criticality Analysis", Sponsored by NASA Headquarters/ Code QW February 15, 1996, <https://radhome.gsfc.nasa.gov/radhome/papers/seecai.htm> accessed December 29 2021
- [45] [20090007715.pdf \(nasa.gov\)](#) accessed 07/10/2022.
- [46] : Simonsen LC, Slaba TC, Guida P, Rusek A (2020) "NASA's first ground-based Galactic Cosmic Ray Simulator: Enabling a new era in space radiobiology research.", *PLoS Biol* 18(5): e3000669. <https://doi.org/10.1371/journal.pbio.3000669> Academic Editor: Tom Misteli, National Cancer
- [47] Gerald Soelkner, "Ensuring the reliability of power electronic devices with regard to terrestrial cosmic radiation", *Microelectronics Reliability* 58 (2016) 39–50.
- [48] C.M. Buttar, "GaAs detectors - A review", *Nuclear Instruments and Method B*, Volume 395, Issue 1, 1 August 1997, Pages 1-8.
- [49] Holmes-Siedle, A. *Nucl. Instrum. Methods Phys. Res. B*. 1974, 121, 69–179.
- [50] Matteo Marzo, Stefano Bonaldo, Markus Brugger, Salvatore Danzeca, Ruben Garcia Alia, Angelo Infantino, and Adam Thornton, "RadFET dose response in the CHARM mixed-field: FLUKA MC simulations", DOI: 10.1051/epjn/2017016
- [51] A. Kahraman, E. Yilmaz, S. Kaya & A. Aktag (2015), "Effects of packing materials on the sensitivity of RadFET with HfO₂ gate dielectric for electron and photon sources", *Radiation Effects and Defects in Solids*, 170:10, 832-844, DOI: 10.1080/10420150.2015.1118689
- [52] G.S. Was, "Fundamentals of radiation material science", pp 77-129 Springer ISBN 978-1-4939-3436-2.
- [53] "Standard Practice for Ensuring Test Consistency in Neutron-Induced Displacement Damage of Electronic Parts" ASTM E 1854 – 96.
- [54] "Commercial documentation on the calibration procedure of some radFET Varadis VT02" – private communications.
- [55] https://www.nasa.gov/mission_pages/cubesats/index.html, accessed December 29 2021
- [56] Agenzia Spaziale Italiana (ASI), www.asi.it, accessed December 29 2021
- [57] <https://www.rsc.org/journals-books-databases/about-journals/lab-on-a-chip/>, accessed December 29 2021
- [58] https://www.nasa.gov/sites/default/files/atoms/files/biosentinel_fact_sheet-16apr2019_508.pdf, accessed December 29 2021.
- [59] TOP-IMPLART <https://salute.sostenibilita.enea.it/projects/top-implart>
- [60] [HZETRN2020\(LAR-19979-1\) | NASA Software Catalog](#)